

Aspects of femtosecond pulse shape transfer via difference frequency mixing

by

Gerda Nicolene Botha

*Dissertation presented for the degree of Doctorate
of Science in the Faculty of Science at Stellenbosch University*



Supervisor: Dr. Hermann Uys

Co-supervisor: Prof. Heinrich Schwoerer

December 2015

Declaration

By submitting this thesis/dissertation electronically, I declare that the entirety of the work contained therein is my own, original work, that I am the sole author thereof (save to the extent explicitly otherwise stated), that reproduction and publication thereof by Stellenbosch University will not infringe any third party rights and that I have not previously in its entirety or in part submitted it for obtaining any qualification.

Date: December 2015

Abstract

We investigate the generation of shaped femtosecond pulses in the infrared spectral regime via a nonlinear process called difference frequency mixing. First we develop a detailed model of the process, incorporating pulse propagation during difference frequency mixing, in the slowly varying envelope approximation. Difference frequency mixing (DFM) is numerically simulated for several wavelengths, nonlinear crystals and Type I and Type II frequency mixing. The different factors influencing the shape transfer efficiency of a shaped pulse to a different wavelength regime, as well as the conversion efficiency, is identified and investigated thoroughly by doing a parametric study. The numerical modeling demonstrates that the efficiency, with which a shaped pulse in the near-infrared is transferred to another wavelength regime, depends strongly on the refractive index of the nonlinear medium for the interacting pulses and is optimal when the velocity of the generated pulse equals that of the shaped input pulse. We show that it is possible to control the temporal pulse duration of the generated pulse by using specific input angles and so manipulating the effective refractive index of the nonlinear material for the input and generated pulses. It was found that it is possible to temporally broaden or narrow the generated pulse relative to the input pulses. We compare the developed numerical model to experimental measurements. A liquid crystal spatial light modulator (SLM), inserted in a 4f setup, is used to generate the shaped pulses. Experimentally we demonstrate high-fidelity shape transfer by mixing 795 nm and 398 nm femtosecond pulses in a BBO crystal. The temporal broadening and narrowing of the generated pulse is also shown and compared to the numerical simulations showing excellent agreement with measured results.

Opsomming

Ons ondersoek die generasie van gevormde femtosekonde pulse in die infrarooi spektrale regime via 'n nie-liniêre proses genaamd verskil frekwensie vermenging. Ons ontwikkel eerste a gedetaleerde model van die proses wat the pulse se beweging gedurende verskil frekwensie vermenging in die stadige wisselende *envelope* benadering insluit. Verskil frekwensie vermenging is numeries gesimuleer vir 'n paar golflengtes, nie-liniêre kristalle en Tipe I en Tipe II frekwensie vermenging. Die verskillende faktore wat die vorm oordrag effektiwiteit van 'n gevormde puls van een golflengte na 'n ander golflengte beïnvloed; sowel as die doeltreffendheid; is geïdentifiseer en deeglik ondersoek deur 'n parametries studie te doen. Die numeriese model toon dat die oordragseffektiwiteit waarmee die gevormde puls in die naby-infrarooi na 'n ander golflengte oorgedra word, afhanklik is op die brekingsindekse van die nie-liniêre medium vir die interaktiewe pulse en is optimaal wanneer die snelheid van die gegenereerde puls gelyk is aan die snelheid van die gevormde inkomende puls. Ons wys dat dit moontlik is om die pulsduur van die gegenereerde puls te beheer deur spesifieke invalshoeke te gebruik en so die effektiewe brekingsindeks van die nie-liniêre materiaal vir die inkomende en gegenereerde pulse te manipuleer. Daar is gevind dat dit moontlik is om die gegenereerde pulse langer of korter to maak relatief tot die inkomende pulse. 'n Vloeibare kristal ruimtelike lig moduleerder (SLM), geplaas in 'n 4f opstel, word gebruik om die vorm van die pulse te genereer. Eksperimenteel demonstreer ons hoë-trou vorm oordrag deur 795 nm en 398 nm femtosekonde pulse in 'n BBO kristal te meng. Die rek en krimp van die duur van die gegenereerde pulse word ook gewys en vergelyk met die numeriese simulaties wat uitstekend vergelyk met die gemete resultate.

Acknowledgments

I would like to express appreciation and thanks to my advisor Dr. Lourens Botha, who have been a tremendous mentor for me. I would like to thank him for encouraging my research and for allowing me to grow as a research scientist. Thank you to Dr. Hermann Uys for all the his patience, motivation, enthusiasm, and immense knowledge. He's guidance, advice and support have been priceless. I would like to express my gratitude to Prof. Heinrich Schwoerer for all the helpful experimental advice; insightful, constructive comments and suggestions. Special thanks to Dr. Anton du Plessis for initial experimental guidance; to Hendrik Kloppers and Johan Steyn for all the technical assistance and guidance in the lab and Christine Ruperti who was always ready to help with any and all administrative problems. Thank you to Attie Hendriks, who I shared a lab and equipment with, for the stimulating discussions and Gert Wessels for letting me use his computers for simulations. I would like to express gratitude to the CSIR, National Laser Center for employing me for the duration of my studies and the University of Stellenbosch, Laser Research Institute, where I am registered. And finally, special thanks to my family and friends. Words cannot express how grateful I am for all of the sacrifices that you have made on my behalf. Your prayer for me was what sustained me so far.

Contents

| | | |
|----------|---|-----------|
| 1 | Introduction | 1 |
| 2 | Technical Overview | 6 |
| 2.1 | Laser Specifications | 6 |
| 2.2 | Theory of Pulse Shaping | 9 |
| 2.3 | Pulse Shaping Experimental Setup | 12 |
| 2.4 | Femtosecond Temporal Pulse Measurement | 13 |
| 2.4.1 | Intensity Autocorrelation | 14 |
| 2.4.2 | Intensity Cross-Correlation | 18 |
| 2.4.3 | Frequency-Resolved Optical Gating (FROG) | 19 |
| 2.5 | Difference Frequency Generation Experimental Setup | 21 |
| 3 | Pulse Shaping Using a Spatial Light Modulator | 23 |
| 3.1 | SLM Liquid Crystal Display | 23 |
| 3.2 | Control of Phase and Amplitude | 27 |
| 3.3 | Measurement of the Voltage Dependence | 30 |
| 3.4 | Calculating the Phase Calibration Curve | 33 |
| 3.4.1 | Creating a Double Pulse | 35 |
| 3.5 | Simulating the SLM | 37 |
| 3.5.1 | Damage Threshold of SLM | 40 |
| 4 | Difference Frequency Mixing | 42 |
| 4.1 | Theory | 43 |
| 4.2 | Conservation of Energy During Difference Frequency Mixing | 49 |

| | |
|--|------------|
| <i>CONTENTS</i> | vi |
| 4.2.1 Weak Coupling Limit | 52 |
| 4.3 Numerical Modeling | 55 |
| 4.4 Parametric Study | 59 |
| 4.4.1 Influence of Nonlinear Coupling Strengths | 60 |
| 4.4.2 Influence of Relative Velocities on Shape Transfer | 63 |
| 4.4.3 Influence of Relative Velocities on a Pulse FWHM | 66 |
| 4.5 Phase Matching | 69 |
| 4.6 Physical Examples | 71 |
| 4.6.1 Type II Difference Frequency Mixing for Generating Mid-IR Pulses | 71 |
| 4.6.2 Type I Frequency Mixing for Generating Near-IR | 77 |
| 4.7 Phase Transfer | 83 |
| 5 Experimental Equipment | 84 |
| 5.1 Laser Stability | 84 |
| 5.2 SLM Assisted Autocorrelation | 87 |
| 5.3 SLM | 88 |
| 5.3.1 Calibration of the Pixels and Spectrum | 88 |
| 5.3.2 Measuring the Pulse After the 4f Setup | 89 |
| 5.3.3 SLM stability | 90 |
| 5.4 TOPAS | 93 |
| 5.4.1 Setup | 93 |
| 5.4.2 Characterisation of the TOPAS Output | 94 |
| 6 Difference Frequency Generation of Shaped Pulses | 96 |
| 6.1 Experimental Setup | 97 |
| 6.2 Experimental Results | 98 |
| 7 Summary | 103 |
| Bibliography | 104 |

List of Figures

| | | |
|------|--|----|
| 2.1 | (a) Real part of the electric field of a femtosecond pulse and (b) the corresponding intensity. | 8 |
| 2.2 | Typical 4f pulse shaping setup. | 10 |
| 2.3 | Folded experimental setup. | 13 |
| 2.4 | Autocorrelation setup. | 15 |
| 2.5 | Simulation of (a) an 123 fs Gaussian pulse and (b) the 174 fs autocorrelation signal for figure (a). | 16 |
| 2.6 | Measured autocorrelation trace of the amplifier pulse. | 16 |
| 2.7 | (a) Movement of pulses input during autocorrelation. (b) Corresponding autocorrelation peaks. | 17 |
| 2.8 | (a) Simulated 300 fs double pulse and (b) autocorrelation trace of the double pulse. | 17 |
| 2.9 | Cross-correlation trace of a double pulse with a single pulse of which the FWHM is (a) 1% of the input double pulse FWHM and (b) 150% the input double pulse FWHM. | 19 |
| 2.10 | FROG measurement of a (a) single pulse and (b) chirped pulse. | 20 |
| 2.11 | Extracted phase of the chirped pulse in figure 2.10(b). | 21 |
| 2.12 | Difference frequency generation experimental setup. | 22 |
| 3.1 | A liquid crystal display front view and a single pixel side view .[1] | 24 |
| 3.2 | Cross section of a single liquid crystal cell with (a) $V = 0$ and (b) $V \neq 0$. [1] | 25 |
| 3.3 | (a) Top: Experimental setup of a folded SLM configuration and (b) Bottom: schematic drawing showing the optical axis orientation for the folded SLM setup in (a). | 28 |
| 3.4 | Calibration setup. | 31 |
| 3.5 | Measured Transmission-Voltage Graph for display B. | 32 |

| | | |
|------|--|----|
| 3.6 | Standardisation of transmission values. | 34 |
| 3.7 | Calculated ϕ dependence. | 35 |
| 3.8 | a) Amplitude and Phase modulation and b) corresponding voltage counts for a 150 fs double pulse. | 37 |
| 3.9 | Simulating an ideal shaper with (a) a continuous response function ($H(\omega)$) for a 250 fs double pulse and (b) generated 250 fs double pulse. | 38 |
| 3.10 | Simulating a discrete shaper with (a) pixelated response function for a 250 fs double pulse between selected frequencies, (b) half an oscillation of response function, (c) the generated 250 fs double pulse zoomed in on the x-axis to show the replicas, (d) the double pulse and the (e) corresponding spectrum of the shaped pulse. | 39 |
| 4.1 | Visualisation of the Lax-Friedrichs method. | 56 |
| 4.2 | Relative movement of the pulses using the Lax-Friedrichs method. | 57 |
| 4.3 | Difference frequency generation simulated using the Euler method. | 58 |
| 4.4 | Difference frequency generation simulated using the combined Lax-Friedrichs and the Euler method in a single pulse. | 59 |
| 4.5 | Shape transfer to the idler with (a) $\gamma_s \approx \gamma_p \approx \gamma_i \approx 0.1$ and (b) $\gamma_s \approx \gamma_p \approx \gamma_i \approx 1$ | 60 |
| 4.6 | Shape and amplitude transfer to the idler with (a) $\gamma_p \gg \gamma_s = \gamma_i$ and (b) $\gamma_s \gg \gamma_p = \gamma_i$ | 62 |
| 4.7 | Shape and amplitude transfer to the idler with (a) $\gamma_s \ll \gamma_p = \gamma_i$ and (b) $\gamma_i \ll \gamma_s = \gamma_p$ | 62 |
| 4.8 | Transfer of the pump pulse shape to the idler pulse for (a) $r_v = 2.5$, (b) $r_v = 1.18$, (c) $r_v = 0.8$ and (d) $r_v = 0.56$ | 64 |
| 4.9 | Transfer of the pump pulse shape to the idler pulse for (a) $r_v = 1$ and (b) $r_v = -1$ | 65 |
| 4.10 | Generated single idler pulse for $r_v = 10$, (a) 3d view and (b) comparison between pump and idler pulse. | 66 |
| 4.11 | Generated single idler pulse for (a) $r_v = -0.67$, (b) $r_v = 3.33$, (c) $r_v = 0.91$ and (d) $r_v = 0.50$ | 67 |
| 4.12 | Idler FWHM for different velocity ratios (r_v). | 68 |
| 4.13 | Phase matching diagram. | 70 |
| 4.14 | Input signal and pump angle vs (a) idler wavelength and (b) effective idler refractive index for generating $1.6\mu\text{m}$ in GaSe. | 72 |
| 4.15 | Input pump angle vs (a) relative velocities and (b) relative velocity ratio for generating $1.6\mu\text{m}$ in GaSe. | 72 |

| | |
|---|----|
| 4.16 (a) Generated wavelengths for a collinear pump and signal configuration with changing pump angle θ_p . (b) Relative velocity ratio (r_v) with respect to changing θ_p and (c) zoomed in graph of 4.16(b) for constant $\phi_{ps} = 0.001^\circ$ | 74 |
| 4.17 Varying pump and signal input angles vs (a) wavelength and (b) the relative velocity ratios (r_v) for generating $10\mu\text{m}$ in GaSe. | 75 |
| 4.18 Simulating the generation of a $10\mu\text{m}$ double pulse in GaSe. | 76 |
| 4.19 Relative velocities versus input angle for a BBO crystal. | 77 |
| 4.20 (a) Idler wavelength versus angle between signal and pump (ϕ_{ps}) and input angle of pump (θ_p), (b) relative velocities vs incident pump angle (θ_p), (c) relative velocity ratio r_v vs incident pump angle (θ_p) and (d) zoomed r_v vs θ_p for BBO. | 78 |
| 4.21 Generation of shaped idler for $\theta_p = 29.2^\circ$ and (a) $\phi_{ps} = 0.01^\circ$, and (b) $\phi_{ps} = 2.5^\circ$ | 79 |
| 4.22 Generation of single idler pulse for (a) $\phi_{ps} = 3.4^\circ$, $r_v = 0.5042$ and (b) $\phi_{ps} = 2.4^\circ$, $r_v = 0.2663$ | 80 |
| 4.23 Generation of a single idler pulse for (a) $\phi_{ps} = 7^\circ$, $r_v = 2.019$ and (b) $\phi_{ps} = 5.9^\circ$, $r_v = 1.449$ | 81 |
| 4.24 Blue curve: Angle between the pump and optical axis (θ_p) with constant $\phi_{ps} = 3.4^\circ$. Red curve: Angle between the pump and signal (ϕ_{ps}) with constant $\theta_p = 29.2^\circ$ versus relative velocity ratio (r_v). | 82 |
| 4.25 Phase of input pulse and generated Idler pulse. | 83 |
| 5.1 Average of the amplifier autocorrelation trace with error bars. | 85 |
| 5.2 Deconvolution of autocorrelation trace. | 86 |
| 5.3 (a) Gaussian fit of experimental trace in figure 5.1 and (b) deconvolution of the Gaussian fit in figure 5.3(a). | 86 |
| 5.4 SLM assisted (a) autocorrelation and (b) FROG trace. | 87 |
| 5.5 (a) The spectra after the 4f setup and (b) the same spectra with blocked pixels. | 88 |
| 5.6 Spectrum calibrated for corresponding SLM pixels. | 89 |
| 5.7 Trace of pulse after the 4f setup. | 90 |
| 5.8 Average of the measured pulses. | 91 |
| 5.9 Simulation of (a) the mask, $H(\omega)$, with an offset added, (b) the resulting shaped pulse and (c) the autocorrelation trace for the pulse in figure (b). | 92 |
| 5.10 TOPAS configuration.[2] | 94 |

| | |
|--|-----|
| 5.11 Spatial profile of 863.66 nm generated pulse from the TOPAS (a) camera image, (b) sum of the x profile and (c) y profile with a Gaussian fit. | 94 |
| 5.12 TOPAS output power vs wavelength. | 95 |
| 6.1 Phase matching scheme for Type I frequency mixing. | 97 |
| 6.2 Difference frequency generation experimental setup. | 97 |
| 6.3 Comparison between the averaged pulses and amplifier input. | 99 |
| 6.4 Averaged spectrum indicating the (a) input signal pulse and (b) generated idler pulse for a temporally narrowed idler pulse. | 100 |
| 6.5 Comparison between the average pulses and amplifier input. | 100 |
| 6.6 Comparison between the average pulses and SLM input. | 101 |

List of Tables

| | | |
|-----|--|----|
| 4.1 | Parameters for coupling strength study. | 61 |
| 4.2 | Shape transfer to idler. | 65 |
| 4.3 | (a) Error and peak separation ratio for a simulated double pulses at different ϕ_{ps} and (b) FWHM for simulated single pulses at different ϕ_{ps} for constant $\theta_p = 29.2^\circ$ | 81 |
| 4.4 | Pump angle with the crystal optical axis (θ_p) and corresponding velocity ratio (r_v) for constant $\phi_{ps} = 3.4^\circ$ | 82 |

List of Abbreviations

| | |
|------------------|--|
| LC-SLM | Liquid Crystal Spatial light modulator |
| SLM | Spatial light modulator |
| UV | Ultra violet |
| MIR | Mid Infrared |
| IR | Infrared |
| AOM | Acousto optic modulator |
| FROG | Frequency resolved optical gating |
| DFM | Difference frequency mixing |
| FWHM | Full width half maximum |
| OPA | Optical parametric amplifier |

Chapter 1

Introduction

Many molecular dynamical processes take place on the *ultrafast* timescale which is on the order of 10^{-12} seconds. This time scale is significantly faster than what can be observed or captured by conventional electronics. It is important to be able to measure these dynamics in order to manipulate interactions, for instance steering a chemical reaction down a specific reaction channel or identifying mechanisms in a biological process. Ultrafast, specifically femtosecond, laser pulses have a duration similar, or faster, to these dynamics and can be used as a viable tool for measuring and/or manipulating chemical reactions and molecular dynamics. Possible application areas where this can be beneficial include ionization, isomerization, vibration and rotational dynamics, charge-transfer, fragmentation, chemical reactions and biological processes. We are interested in vibrational dynamics since selective vibrational excitation can steer a chemical reaction down a specific reaction channel [3]. This requires us to be able to manipulate the electronic ground state of the vibrational or rovibrational molecular dynamics, which takes place in the mid- to far infrared wavelength regime (MIR and FIR respectively).

Temporally shaped femtosecond laser pulses have emerged as a versatile tool for controlling and probing molecular processes. Experimental demonstrations to date include selective ionization [4], control of dissociation branching ratios [5], optimization of fluorescence signals [6], wave packet manipulation [7] and the observation of ground state dynamics through four-wave mixing [8]. Very often, control of these processes are coherent, since pulse durations on the femtosecond timescale are typically faster than the relevant decoherence processes influencing the dynamics.

Tannor and Rice [9] introduced the pump-dump scheme that can be used for selective bond excitation,

where a localised wave packet is formed by a short femtosecond pulse, exciting the reactant. After a predetermined short time period a second femtosecond pulse is used to de-excite the wave packet, “dumping” it to a lower excited level or different region in the potential of the ground state.

The vibrational wave packet motion in the electronic ground state of potassium (K_2) was investigated using a pump-dump scheme by Schwoerer et al. [10] where the wave packet is prepared by stimulated Raman scattering (pump-dump) with the wave packet consisting out of several coherent excited vibrational states, due to the femtosecond pulse broad bandwidth. After the wave packet evolves for some time, it is probed by a third pulse and a time-of-flight mass spectrometer is used to detect the K_2 ion fragments.

An area of interest that is less well studied using shaped pulses, is the direct manipulation of electronic ground state vibrational or rovibrational molecular dynamics [11]. While examples abound exist of indirect control via Raman transitions [12, 13] and generation of vibrational wave packets in excited electronic states [14], limitations on commercially available programmable pulse shapers generally preclude generation of shaped pulses in the infrared (IR) regime which is required for direct addressing of vibrational excitations.

To perform direct manipulation of the electronic ground state vibrational or ro-vibrational molecular dynamics, it is critical to accurately shape temporal femtosecond pulses in the far infrared wavelength regime. Temporal pulse shaping can be done using various types of pulse shapers, such as fixed spatial masks, programmable spatial light modulators (SLM), acousto-optic modulators (AOM) or even deformable mirrors. The programmability of SLM and AOM are advantageous for the implementation of adaptive techniques such as open and closed loop control, which makes it unnecessary to have complete knowledge about the chemical reaction dynamics or solve the Hamiltonian of the relevant molecules to select the optimal temporal pulse shape. One example is using closed loop control to optimise the output of a specific product in a chemical reaction by changing the pulse shape. Temporal pulse shaping has been used in many applications and is therefore a well established technique. One of the earliest femtosecond pulse shaping experiments was demonstrated by Weiner et al. [15] using spatially patterned amplitude and phase masks. Meshulach et al. [16] employed a SLM in a self-learning pulse-shaping system for shaping uncharacterised pulses into the wanted waveforms. The most important feature of a SLM is the active display, which consist out of pixels containing liquid crystals. Brixner et al. [17] used an SLM with 128 independent pixels, together with different characterisation methods and appropriate optimisation algorithms, for optimised frequency-domain femtosecond laser

pulse shaping. Strobrawa et al. [18] investigated pulse shaping with a 640 pixel SLM where the larger active area made it possible for high-power as well as high-resolution pulse shaping, so that more accurate pulse shaping can be done due to less discretisation caused by the increased number of pixels. The pulse shaper, with a resolution of 0.15 nm/pixel, has been improved on through the years with Delagnes et al. [19] achieving a resolution of approximately 0.06 nm/pixel. Monmayrant et al. [20] employed two 640 pixel liquid crystal devices in order to do high resolution and power pulse shaping. Their device provided a wide enough shaping window to be useful in some coherent control experiments. Instead of using nematic liquid crystals, ferroelectric liquid crystals can also be used. Ferroelectric liquid crystals offer approximately two orders of magnitude faster response time, but are limited to binary phase modulation and in general induce significant loss [21]. Pulse shaping can also be done by shaping only the phase or the amplitude envelope of a pulse. Zou et al. [22] as well as Hacker [23] utilised phase-only pulse shaping.

Amplitude and phase shaping of mid- to far-infrared and ultra violet (UV) regime are not as straightforward as in the visible and near infrared regime, due to the limitations on the wavelength shaping range of most programmable pulse shapers. Liquid crystals absorb radiation in the MIR and UV range, making shaping in these regimes more complicated. In recent years germanium acousto optic modulators (Ge AOM), pulse shapers that can operate in the FIR regime, have become commercially available but is expensive and therefore not always available in laboratories. Shim et al. [24, 25] shaped a series of pulses directly in the MIR using a Ge AOM that worked successfully in the IR to far-IR regime.

An alternative method to direct pulse shaping, when shaping pulses in these inaccessible wavelength regimes and shapers restricted to the visible spectrum, is to do indirect shaping. Indirect pulse shaping is accomplished by shaping the pulse in the visible or near-IR regime and then transferring the shape to the desired wavelength via a nonlinear interaction. Various nonlinear interaction schemes can be used, from second harmonic generation (SHG) to sum frequency generation (SFG) and difference frequency generation (DFG). Apart from generating shaped pulses in the MIR and FIR wavelength regimes it is also possible to use indirect pulse shaping to generate shaped pulses in the UV wavelength regime [26].

The transfer of a pulse shape from one wavelength regime to another desired regime has been investigated through numerical modeling by several groups. Bakker et al. [27] presented a model to accurately simulate difference frequency mixing for picosecond pulses using various crystals and crystal lengths.

They found that by using their model the effect of phase mismatch, group velocity differences and depletion of the pulses in the medium can be quantified for a collinear configuration. Numerical simulations of the nonlinear interaction between single pulses have been performed in the past by Cavallari et al. [28] who investigate the feasibility of using difference frequency mixing to generate sub-100 fs pulses in the 3 to 5 μm range. They used type II frequency mixing in a potassium titanyl phosphate (KTP) nonlinear crystal, where a pump wave (ω_p , ordinary polarisation) is mixed with a signal wave (ω_s , extraordinary polarisation) to produce an idler wave ($\omega_i = \omega_p - \omega_s$, with polarisation o) and found that the simulation corresponds well to their experimental measurements. Prawiharjo et al. [29] did a theoretical and numerical examination of indirect pulse shaping through DFG, assuming the undepleted pump and unamplified signal approximation, which is valid for a non-dispersive nonlinear medium i.e. a short crystal length and low intensities. Calculations were done to investigate the effect of dispersion in the material as well as the temporal walk-off in order to achieve good fidelity parametric transfer in a dispersive material. The nonlinearity in the interaction and group velocity dispersion were investigated through numerical analysis with the nonlinear process and shape transfer investigated for periodically-poled lithium niobate.

The experimental generation of wavelengths in the MIR to FIR regime have been successfully accomplished by various groups. Tsubouchi et al. [30] simulated, experimentally generated and compared difference frequency mixed MIR phase- and amplitude shaped pulses. They found that the temporal pulse features transferred mostly to the generated pulse but that there was large changes in the spectral features. Hacker et al. [23] investigated the generation of shaped ultra short pulses at 400 nm by using frequency doubling, through numerical simulation and experimental measurements, showing complete transfer of a phase modulation to the temporal and corresponding spectral domain. Indirect shaped pulses has been implemented widely for various purposes. Tan et al. [31], using an AOM, as well as Witte et al. [32], using an SLM, shaped pulses in the near infrared regime and transferred the shape to the MIR 3 – 10 μm regime. Tan et al. used phase locked MIR pulses to obtain the complex valued optical free induction decay of a C-H vibrational mode of chloroform, while Witte successfully implemented the nonlinear process in a electronic feedback loop which can be used in various applications.

For direct manipulation of the electronic ground state vibrational molecular dynamics, the finer features in the pulse shape profile are vital, making it necessary to know how accurate the pulse shape transfer is to the MIR to FIR wavelength regimes. In this thesis we build on the work of the above au-

thors by further studying femtosecond pulse shape transfer via difference frequency generation (DFG). Though previous authors investigated indirect pulse shaping it is still not clear which experimental configurations would give the best shape transfer and conversion efficiency as well as which crystals would be optimal for the process. We model the interaction numerically to identify critical factors influencing the efficiency of the pulse shape transfer to the desired wavelength. Using the numerical model we can identify the optimal experimental configuration and wavelengths for excellent shape transfer to the required wavelength regime, as well as experimental configurations to temporally compress or stretch the pulse. Finally, we successfully demonstrate the pulse transfer process experimentally and do auto-correlation characterisation of the transfer fidelity. The numerical simulation and experimental results are compared for three cases; where the DFG pulse is narrower compared to the input single pulses, the DFG pulse is stretched and the case where the shape of one shaped input pulse is transferred to the DFG pulse. The main outcome of this thesis is to provide a recipe for achieving high fidelity pulse shape transfer through difference frequency generation.

The rest of this thesis consist of 6 parts. We start by characterising femtosecond pulses, looking at the method for pulse shaping and propose an experimental setup. We continue with an in depth look at the components of the pulse shaper (SLM), namely the liquid crystal display and how it's is employed in pulse shaping. In chapter 4 we look at the DFG of a shaped pulse and do a numerical study of the interaction for different nonlinear crystals and wavelength regimes exploring the critical parameters in the interaction. Next we get an overview of the experimental equipment and laser light that will be used in our final experiment. In the second to last chapter we revisit the experimental setup for the DFG and experimentally look at the three interaction cases we simulated in chapter 4. We conclude with a discussion of the results generated throughout the thesis and propose a way forward.

Chapter 2

Technical Overview

2.1 Laser Specifications

In the following chapters we discuss the use of femtosecond laser pulses in theoretical as well as experimental work. In our experimental setup pulses are created by a pulsed femtosecond Coherent Mira oscillator with a repetition rate of 86 MHz, and are subsequently amplified using a regenerative Coherent Legend ultrafast amplifier to produce laser pulses with a repetition rate of 1 kHz, an average power of 1 W (1 mJ per pulse energy) and center wavelength (λ_c) of 795 nm. A regenerative amplifier allows multiple passes, by means of retro reflection, through a pumped gain medium. The pulses is coupled out of the cavity by a Pockel cell combined with a quarter-wave plate, that acts as an optical switch, to exit through a polariser. Ideally these laser pulses consists out of an oscillating electric field with a Gaussian envelope, which can mathematically be described as

$$E(t) = E_0 e^{[-\alpha t^2 - i\omega_c t]}, \quad (2.1)$$

with E_0 the amplitude, t the time, $\omega_c = 2\pi\nu_c$ the center frequency of the pulse and α is related to the inverse of the temporal duration (Δt) squared, of the Gaussian pulse, with the derivation to follow in equation 2.3. The wavelength of the radiation is related to the radiation frequency through $\lambda = \frac{c}{\nu} = \frac{2\pi c}{\omega}$. The intensity is related to the electric field via $I(t) = \frac{c\epsilon_0 n}{2} |E(t)|^2$ with c the speed of light, ϵ_0 the vacuum permittivity and n the refractive index. All units of measurement in this body of work are in SI units.

The temporal duration of a pulse is characterised by the full width half maximum (FWHM). This

FWHM (Δt) is defined, for a Gaussian pulse, as twice the time it takes for the pulse amplitude to fall from maximum pulse intensity ($I(0)$) to half of the maximum intensity. To calculate the FWHM we solve equation 2.1 at half of the maximum intensity, $\frac{I(0)}{2}$, of the pulse

$$\begin{aligned}
 I(t) &= \frac{c\epsilon_0 n}{2} |E(t)|^2 = \frac{c\epsilon_0 n}{2} \left(|E_0| e^{-\alpha t^2} \right)^2, \\
 I(t) &= I(0) e^{-2\alpha t^2}, \\
 \frac{I(0)}{2} &= I(0) e^{-2\alpha (\Delta t/2)^2}, \\
 \alpha &= \frac{2 \ln(2)}{(\Delta t)^2}.
 \end{aligned} \tag{2.2}$$

with $\Delta t = t_2 - t_1$ where t_1 and t_2 are the times where the pulse is at half of the maximum intensity. Equation 2.1 can now be written in terms of the temporal FWHM

$$E(t) = E_0 e^{\left[-\frac{2 \ln(2)}{(\Delta t)^2} t^2 - i\omega_c t \right]}. \tag{2.4}$$

By doing a Fourier transform of equation 2.1, we have the mathematical description of the pulse in the frequency domain

$$\begin{aligned}
 E(\omega) &= \int_{-\infty}^{\infty} E(t) e^{i\omega t} dt, \\
 &= E_0 \sqrt{\pi/\alpha} e^{-(\omega - \omega_c)^2 / 4\alpha},
 \end{aligned} \tag{2.5}$$

with ω the frequencies in the pulse. Similar to equation 2.2 we calculate α for the spectral FWHM of equation 2.5 and find

$$\alpha = \frac{(\Delta \omega)^2}{8 \ln(2)}, \tag{2.6}$$

with $\Delta \omega$ the spectral FWHM of the laser, known as the bandwidth. Equation 2.5 can now be written as

$$E(\omega) = \frac{E_0 \sqrt{8\pi \ln(2)}}{\Delta\omega} e^{-(\omega - \omega_c)^2 2\ln(2)/(\Delta\omega)^2}. \quad (2.7)$$

By setting equation 2.3 and 2.6 equal to each other we find $\Delta t \times \Delta\nu = 0.44$ for a Gaussian pulse, this value differs for different pulse shapes. This relation is known as the time-bandwidth product and from this it is clear that the wider the frequency bandwidth, the shorter the pulse duration will be. In our system the wavelength bandwidth FWHM of the pulses used in our experiments vary between 10 nm and 15 nm, depending on the laser alignment. From the time-bandwidth product we can calculate, for example, that the minimal possible pulse duration for a pulse with a 10 nm bandwidth, from our experimental setup would be 93 fs. We use the term minimal since the pulse duration can be longer than expected from the time-bandwidth product due to higher order effects in the pulse, so that the product can be written as $\Delta t \times \Delta\nu > 0.44$.

Figure 2.1(a) shows a simulation (using equation 2.4) of the real part of a typical pulse used in our experimental setup (where $\Delta t = 100$ fs and $\lambda_c = 795$ nm), with the blue line representing the oscillating carrier electric field strength and the red line indicating the envelope of the pulse. The intensity corresponding to the electric field in figure 2.1(a), with a temporal FWHM of 100 fs, is shown in figure 2.1(b).

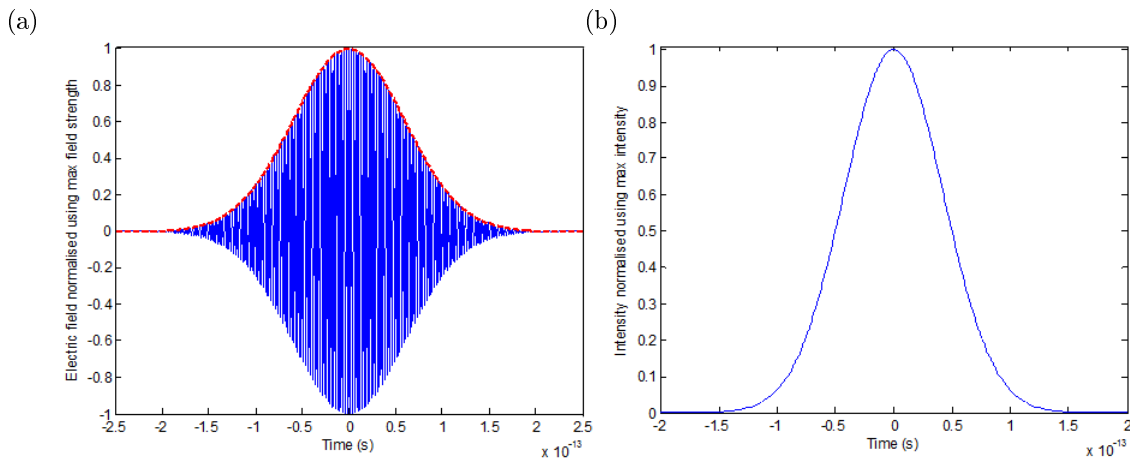


Figure 2.1: (a) Real part of the electric field of a femtosecond pulse and (b) the corresponding intensity.

In the case where the shape of the pulse envelope is changed so that the pulse is no longer Gaussian, or the wavelength components are out of phase with each other, the pulse would be described as a shaped pulse. Two kinds of shaped pulses will frequently be discussed in this thesis, namely chirped

pulses and double pulses. Chirped pulses are a good example of phase shaping while a double pulse is a good example of a pulse with a shaped envelope.

When the relative phases of the different wavelength components of a pulse are increasing or decreasing quadratically with increasing wavelength, the pulse is linearly chirped. Such a linearly chirped pulse is described mathematically as

$$E(t) = E_0 e^{[-\alpha t^2 - i\omega_c t + i\phi(t)]},$$

with $\phi(t) = \beta t^2$ the phase of the pulse and β determining the degree of phase variation in the pulse. Chirp can occur when the laser pulse moves through a dispersive medium and the different wavelength components go out of phase, delaying some of the wavelengths more than others, which stretches the pulse in time.

The second pulse shape that will be investigated is a double pulse. We describe a double pulse as two identical Gaussian pulses separated by a short time duration (τ), and it can be created by various methods. The double pulse can be expressed in the temporal domain as

$$E(t) = E_0 \left(e^{-\alpha t^2} + e^{-\alpha(t+\tau)^2} \right) e^{-i\omega_c t},$$

with $\alpha = \frac{2\ln(2)}{(\Delta t)^2}$ and in the spectral domain as

$$E(\omega) = E_0 \sqrt{\frac{\pi}{\alpha}} e^{-(\omega-\omega_c)^2/4\alpha} \left[1 + e^{-i(\omega-\omega_c)\tau} \right],$$

with $\alpha = \frac{(\Delta\omega)^2}{8\ln(2)}$ and τ the temporal separation between the two pulses.

2.2 Theory of Pulse Shaping

Gaussian pulses are not always the optimal pulse shape for use in experiments, for example in coherent control experiments. The Gaussian pulse shape can be changed to the desired pulse shape by shaping the temporal amplitude envelope and/or phase. Unfortunately it is not possible to shape the pulses directly in the time domain, since femtosecond pulses are so short that current electronics are not fast enough. Fortunately we have established that the temporal and spectral domain of a pulse

are coupled and we can move from one domain to the other by doing a Fourier transform. To work around shaping in the temporal domain, the pulse can be shaped in the frequency (spectral) domain by changing the amplitude and/or phase of the different frequencies in the pulse bandwidth. There are several pulse shaping devices available, such as fixed spatial masks, programmable liquid crystal spatial light modulator (LC SLM), acousto-optic modulators (AOM) or even movable or deformable mirrors. We will be focusing on programmable liquid crystal spatial light modulators (SLM) since this is what we use in our experiments.

Experimentally pulse shaping is done in the frequency domain, the wavelength components of the temporal pulses have to be spatially separated. The phase and/or amplitude mask ($H(\omega)$) is applied to the wavelengths of the spectrally dispersed pulse, using an SLM active display. A dispersive optic, for instance a grating, is used that spatially separates the grating's first order beam, into its frequency components, see figure 2.2. The dispersed wavelength components are collimated with a lens with focal length f placed one focal length (f) before the SLM. Now each wavelength component is focused and falls on the SLM active display, which consists out of liquid crystals inside pixels which are separated by gaps. The influence of the pixels and gaps on the shaped pulse will be described in the next chapter, section 3.5. After the light is transmitted by the shaper, the beam follows an identical path to that of before falling on the SLM, focused by a second identical lens and falling on a second identical grating. The second grating collimates the beam and compresses all the wavelength components so that there are no spatial dispersion of the wavelengths in the femtosecond pulse, similar to the input pulse.

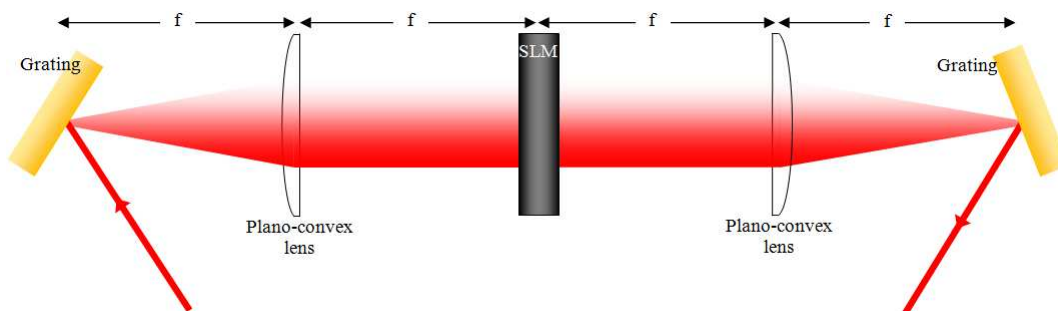


Figure 2.2: Typical 4f pulse shaping setup.

This setup, where the distance between each element is the focal length of the lens, is known as a 4f setup, see figure 2.2. The focal length of the lenses are chosen by considering the grating groove density, the spectral spread of the laser light and the wanted illuminated area on the pulse shaper pixel

display. By using the grating equation the spatial spread of the wavelegnths can be calculated

$$d(\sin\theta_i + \sin\theta_m) = m\lambda$$

with d the inverse groove density, θ_i the input angle with respect to the grating normal and θ_m the output/diffracted angle with respect to the grating normal for wavelength λ . The focal length influences the resolution of the SLM (wavelength per pixel), since the resolution is dependent on the amount of SLM pixels illuminated by the dispersed beam as well as the bandwidth of the laser.

From figure 2.2, pulse shaping is done by changing the spectral components of the pulse using a SLM, which functions as a programmable filter or mask, with $H(\omega)$ known as the transfer function of the filter [21]. This is described mathematically as

$$E_{\text{out}}(\omega) = E_{\text{in}}(\omega)H(\omega), \quad (2.8)$$

$$\text{so that } H(\omega) = \frac{E_{\text{out}}(\omega)}{E_{\text{in}}(\omega)}. \quad (2.9)$$

$E_{\text{in}}(\omega)$ is the input electric field in the frequency domain, $H(\omega)$ the frequency mask and $E_{\text{out}}(\omega)$ the shaped electric field in the frequency domain after the filter. Equation 2.8 can be expressed in the temporal domain as linear filtering. The Fourier transform of equation 2.9, using the convolution theorem, expresses shaping of a temporal pulse as

$$e_{\text{out}}(t) = e_{\text{in}}(t) * h(t) = \int dt' e_{\text{in}}(t')h(t - t'), \quad (2.10)$$

with $*$ the convolution. $e_{\text{out}}(t)$ is the output temporal pulse after the shaping and $e_{\text{in}}(t)$ is the input pulse in the time domain. $e_{\text{in}}(t)$, $E_{\text{in}}(\omega)$ and $e_{\text{out}}(t)$, $E_{\text{out}}(\omega)$, are Fourier transform pairs respectively [21]. $h(t)$ is the impulse response of the filter, which is the Fourier transform of the frequency mask (transfer function) $H(\omega)$, which is implemented by the pulse shaper with

$$H(\omega) = \int dt h(t) e^{-i\omega t},$$

$$h(t) = \frac{1}{2\pi} \int d\omega H(\omega) e^{i\omega t}.$$

In summary, to do temporal pulse shaping the input pulse $e_{\text{in}}(t)$ has to be Fourier transferred to the spectral domain $E_{\text{in}}(\omega)$ where the frequency mask $H(\omega)$ is applied to create $E_{\text{out}}(\omega)$. The pulse is then transformed back to the temporal domain and we have a temporally shaped pulse, $e_{\text{out}}(t)$.

It has been previously mentioned that pulse shaping can be done by shaping the amplitude and/or phase of each wavelength component. Phase-only shaping has the advantage of conserving the energy of the pulse compared to amplitude shaping, where the wavelength components intensities are modulated [23, 22]. For several pulse shapes, such as pulse trains with different envelopes, phase-only shaping can be sufficient for the generation of the wanted shaped pulse with the advantage of no losses due to amplitude modulation [21]. The restricting factors that should be kept in mind when shaping with an SLM, is the number of pixels illuminated; the gap to pixel ratio (called the form factor); maximum phase shift; the maximum amplitude modulation contrast and the actual width of the pixels [23]. The number of pixels illuminated and the pixel width plays a large part in the shaping resolution, which determines the level of detail that can be used in the amplitude and phase patterns, while the gap to pixel ratio indicates the amount of unshaped light and wavelengths that will pass through the shaper.

2.3 Pulse Shaping Experimental Setup

We discussed the general 4f setup for pulse shaping in section 2.2 with the experimental setup shown in figure 2.2. The 4f setup can be made more compact by replacing the lenses with the appropriate plano-concave mirrors, as shown by Stobrawa [18] and Präkelt [33], or folding the setup by placing a mirror at the appropriate position. We employ the folded 4f configuration in our experimental setup by placing a flat mirror after the transmissive SLM displays, see figure 2.3. The reflected beam in figure 2.3 travels back on the same path as the input beam, creating a configuration where the radiation passed through the SLM active display and a 300 mm focal length lens twice and reflected by the grating, with a groove density of 1800 grooves/mm, twice. A polariser is placed in the output beam which is spatially separated from the input beam after the 4f setup. This folded configuration significantly reduces the size of the experimental setup.

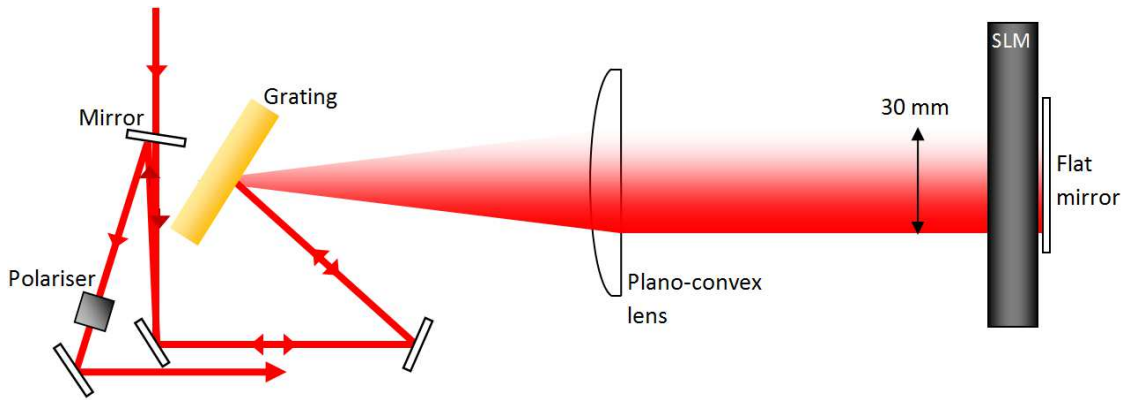


Figure 2.3: Folded experimental setup.

The folded configuration is easier to align due to fewer optics in the setup and the light following the same path back to the grating, making the flat mirror the only optic necessary to align the beam after the SLM. In order to characterise the folded setup we calculate the losses that the setup induces in the total power. There is a loss in power at the grating due to the diffraction of the beam in different spatial modes with only the first mode used in the setup. We find an 8.8% loss in power due to the grating by measuring the input power before (125 mW) and the first order after the grating (114 mW). After the 4f setup and polariser, with both displays of the SLM set for maximum transmission, the power is measured as 45 mW. By using the calculated loss due to the grating and the measured power after the first reflection from the grating and after the 4f setup, the loss induced by the SLM display when the light pass through it twice can be calculated. The power before the light hits the grating the second time is calculated as 49.3 mW using the now known loss percentage of the grating and the output power. The loss in power due to the beam passing through the SLM display twice can now be calculated at 56.7%, using the measured power before and calculated power after the SLM. When repeating the calculation for a single pass 4f setup using the input power and calculated loss percentages for the grating and SLM (divided by 2 for a single pass), we have an output of 74.5 mW. From this we calculate that in a double pass setup there is 40% more loss in power than a single pass configuration.

2.4 Femtosecond Temporal Pulse Measurement

In our experimental work it is very important to have accurate knowledge of the femtosecond pulses that are used and generated in the experiment. In order to characterise the pulses several parameters

have to be measured, namely the temporal envelope, time duration and spectrum of the pulse; while the phase information is necessary when working with pulses with a shaped phase, such as chirped pulses. Due to the ultrafast nature of femtosecond pulses it is not possible to measure the temporal amplitude and phase information or the pulse duration with available conventional electronics. On the other hand, measuring the wavelength spectrum of pulses are straightforward and is done using a spectrometer (Ocean Optics). Different tactics can be employed to measure the temporal information or pulse duration. Some of these techniques are intensity autocorrelation, intensity cross-correlation and frequency resolved optical gating (FROG).

2.4.1 Intensity Autocorrelation

Intensity autocorrelation is a method where the pulse is used to measure itself and works on the principle of nonlinear optics. A nonlinear interaction occurs when one or more laser pulse interact ($\omega_1 \pm \omega_2$) in a nonlinear medium to generate a new pulse (ω_3). The principle of autocorrelation works by measuring the sum frequency signal ($\omega_1 + \omega_2 = \omega_3$) generated when two pulses, I_1 and I_2 , interact in a nonlinear crystal while changing the timing between the two pulses. The signal (ω_3) is measured as a function of the relative time delay (τ) between the two pulses [21]

$$S(\tau) \sim \int dt I_1(t - \tau) I_2(t). \quad (2.11)$$

Experimentally the incoming pulse is split into two replicas by a beam splitter, so that $I_1 = I_2$. One pulse is reflected by the beam splitter to fall on a set of mirrors and is reflected to a lens, see figure 2.4. The identical pulse transmitted by the beam splitter falls on a mirror positioned on a translation stage. The translation stage is used to adjust the difference in path length between the two pulses, effectively adjusting the timing between the pulses. The mirror reflects the beam back on the traveled path and is reflected by the beam splitter to the lens. The setup is aligned so that the path lengths of the two pulses are identical at the predetermined “zero position” of the translation stage. The two beams are focused by the lens into a nonlinear beta barium borate (BBO) crystal with sum frequency mixing taking place in the crystal when the pulses overlap spatially and temporally. The signal $S(\tau)$ is measured by a photo diode placed in the beam path of the generated signal after the BBO crystal. The temporal overlap between the pulses is adjusted by moving the translation stage away from the “zero position”.

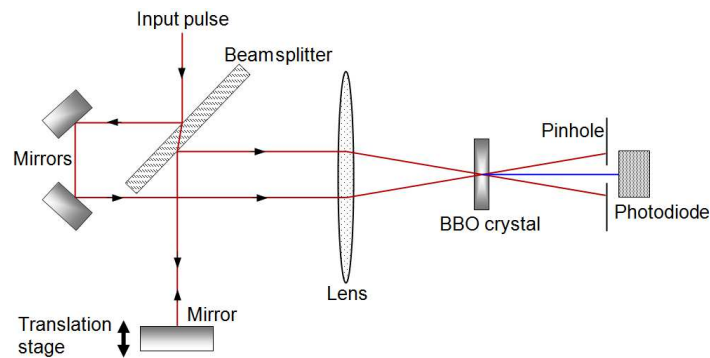


Figure 2.4: Autocorrelation setup.

Maximum sum frequency mixing will occur when there is perfect temporal overlap between the two pulses (identical path lengths). The signal intensity will decrease as the temporal overlap between the 2 pulses decrease until there is no signal, which corresponds to no overlap of the pulses. The exact pulse shape cannot be determined by looking at the autocorrelation trace due to the measured signal being a convolution of the two pulses, see equation 2.11; due to this we use autocorrelation to only determine the time duration for single pulses and the envelope of uncomplicated shaped pulses [21] such as single Gaussian pulses and double pulses. For more complicated shapes (such as a chirped pulse which has phase modulation) this method is not useful, since any phase information is lost in the measurement process.

We simulate a single Gaussian pulse in order to investigate how the ideal autocorrelation signal would look. In figure 2.5(a) the intensity of the simulated input pulse is shown with a 123 fs FWHM. The autocorrelation signal of the pulse in figure 2.5(a) is simulated and shown in figure 2.5(b) with a FWHM of 174 fs.

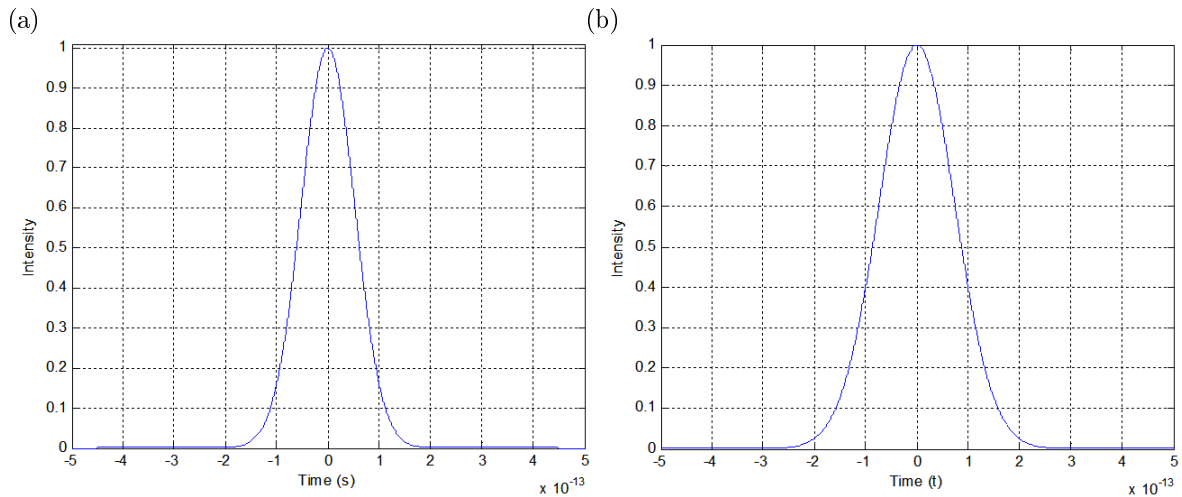


Figure 2.5: Simulation of (a) an 123 fs Gaussian pulse and (b) the 174 fs autocorrelation signal for figure (a).

By multiplying the 174 fs autocorrelation trace in figure 2.5(b) with the factor 0.707 the autocorrelation will have the same FWHM as the input pulse. This 0.707 factor is known as the deconvolution factor and is unique for Gaussian pulses.

A measured experimental autocorrelation trace for a Gaussian pulse with a 123 fs FWHM is shown in figure 2.6, where the pulse duration is calculated by using the FWHM of the autocorrelation signal and taking into account the deconvolution factor for a Gaussian pulse.

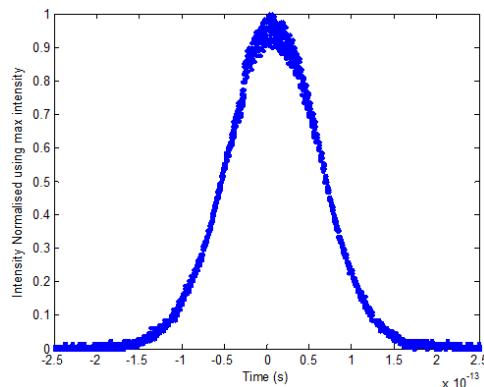


Figure 2.6: Measured autocorrelation trace of the amplifier pulse.

Next we investigate the autocorrelation trace of a double pulse. When measuring a pulse with a more complex shape than a single Gaussian pulse, the trace is not as straight forward. With one double pulse stationary and the other moving temporally over the first, the first peak of the autocorrelation trace will be half the intensity than that of the main peak, and is generated when two peaks overlap. This is

due to less sum frequency generation (SFG) because of only partial temporal overlap, see the second set of double pulses of in figure 2.7. When the two pulses overlap completely (four peaks overlapping, figure 2.7, set 3) the main peak is generated, with maximum temporal overlap giving maximum SFG. Finally when the last two peaks overlap the final autocorrelation peak will be generated with half the intensity of the main peak, see the fourth set of pulses in figure 2.7.

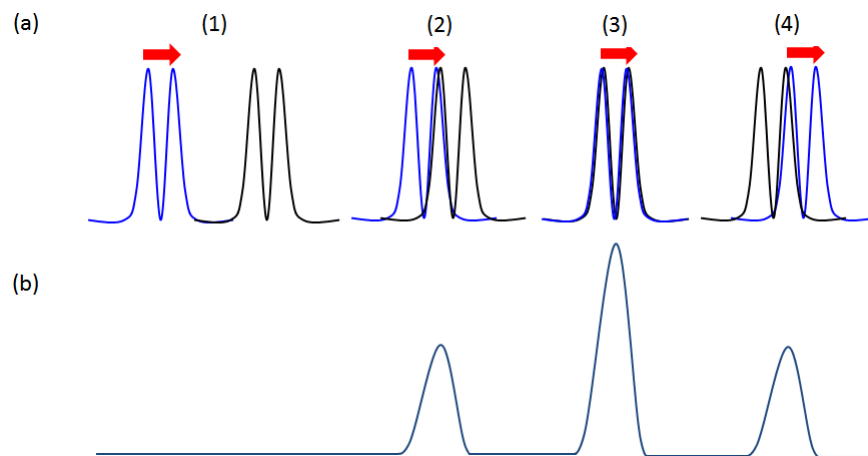


Figure 2.7: (a) Movement of pulses input during autocorrelation. (b) Corresponding autocorrelation peaks.

We simulate a double pulse with a 300 fs peak separation and 123 fs FWHM, as well as the corresponding autocorrelation trace, see figure 2.8(a) and (b) respectively.

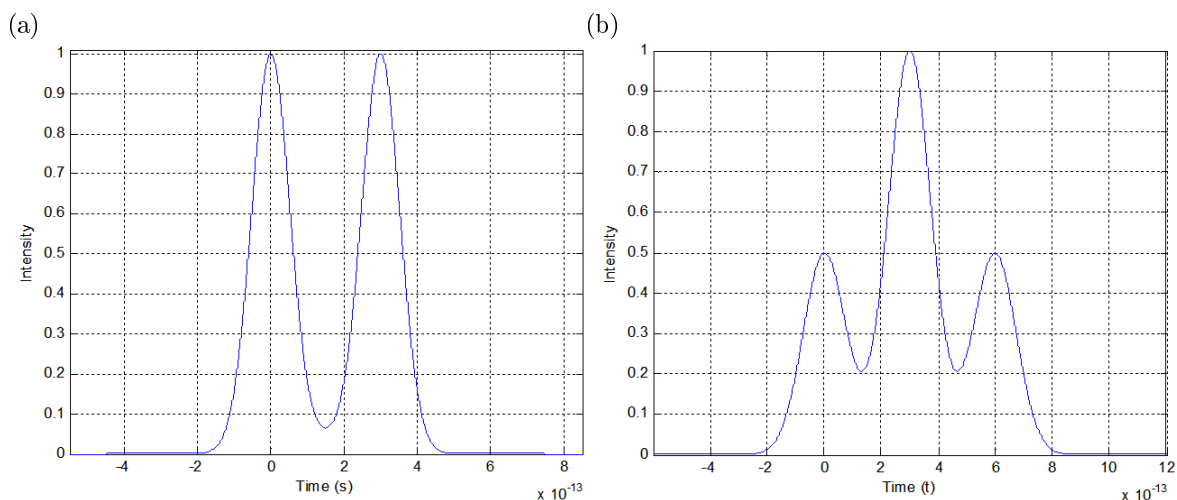


Figure 2.8: (a) Simulated 300 fs double pulse and (b) autocorrelation trace of the double pulse.

In figure 2.8(b) the 300 fs distance between the main and side peaks in the autocorrelation trace

corresponds to the distance between the two peaks of the input pulse in figure 2.8(a). We conclude that we are able to accurately deduce the separation between the peaks of a double pulse from an autocorrelation trace. The FWHM of the main peak (181 fs) is longer than the input pulses FWHM. This is due to the overlap of the side peaks and the main peak in the autocorrelation trace, which occurs when the separation of the input pulses is less than three times the pulses FWHM.

2.4.2 Intensity Cross-Correlation

Intensity cross correlation works similar to intensity autocorrelation, with the first pulse (I_1 in equation 2.11) a short Gaussian pulse and the second pulse (I_2) a shaped pulse (e.g. double pulse) that is significantly longer in time than the single pulse. In the case where the shaped pulse is a double pulse, the cross-correlation trace reflects the double pulse shape and not the autocorrelation trace in figure 2.8(b). This is due to the shaped pulse interacting with the short Gaussian pulse and not a replica of itself, as in autocorrelation. Figure 2.9 shows the cross-correlation traces of the double pulse simulated in figure 2.8(a), which has a 300 fs peak separation and 123 fs FWHM. We compare the two examples of cross-correlation. In each case the short single pulse (I_1) used to measure the double pulse (I_2) (shown in figure 2.8(a)) has a different FWHM. In figure 2.9(a) the FWHM of the short pulse is 0.01 times shorter than the double pulse FWHM. The resulting cross-correlation trace has a FWHM of 123.7 fs and pulse separation of 300 fs. The FWHM of I_1 in figure 2.9(b) is 1.5 times longer than that of the input double pulse, with the cross-correlation trace FWHM 185.7 fs and pulse separation 300 fs. Comparing the two cases in figure 2.9, we can conclude that it is crucial to use a significantly shorter single pulse (I_1) in comparison to the shortest temporal feature of the shaped pulse (I_2) in order to have an accurate cross-correlation trace.

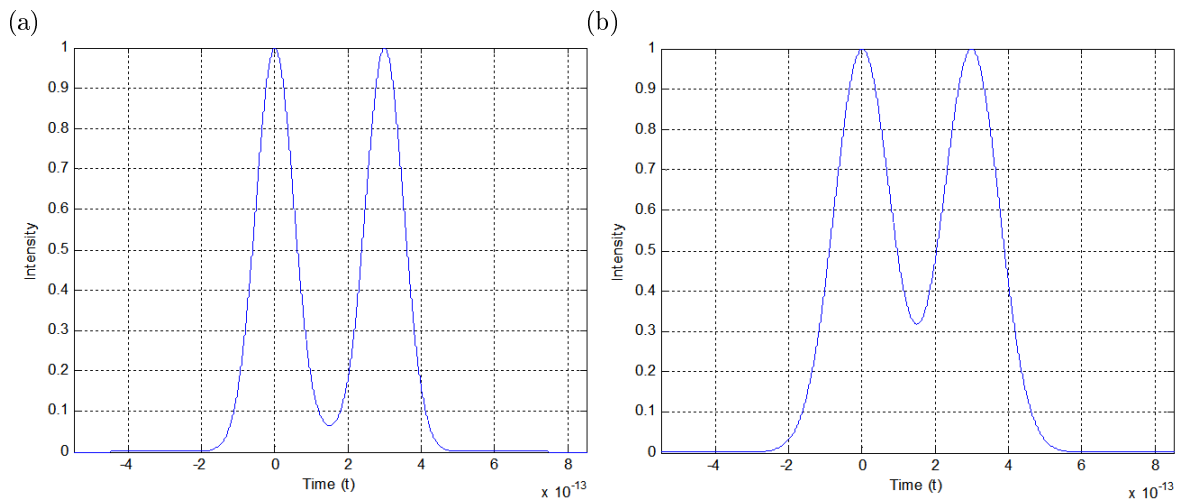


Figure 2.9: Cross-correlation trace of a double pulse with a single pulse of which the FWHM is (a) 1% of the input double pulse FWHM and (b) 150% the input double pulse FWHM.

This confirms that if any of the temporal features of the shaped pulse (I_2) are on the same time scale as the short pulse (I_1), those features will be broadened with respect to the unshaped pulse [21], as shown in figure 2.9(b), with the pulse separation remaining the same. When using this method there is no pulse phase information gathered.

2.4.3 Frequency-Resolved Optical Gating (FROG)

During FROG a laser pulse is measured by splitting the input pulse into two pulses and gating the one pulse with the second identical time-delayed pulse. The gating can be done by various methods of which one is sum frequency generation [21], similar to autocorrelation. The spectrum of the SFG is measured as a function of the delay time (τ) between the two pulses, using a spectrometer. FROG is used to measure the time and spectral information of the frequency time resolved signal from which one can extrapolate the phase information of the shaped pulse, for example a chirped pulse. The FROG experimental setup is identical to the intensity autocorrelation setup in figure 2.4, but with the photo diode, which measures the SFG, replaced by a spectrometer. We measure an experimental single Gaussian pulse and chirped pulse for comparison, see figure 2.10.

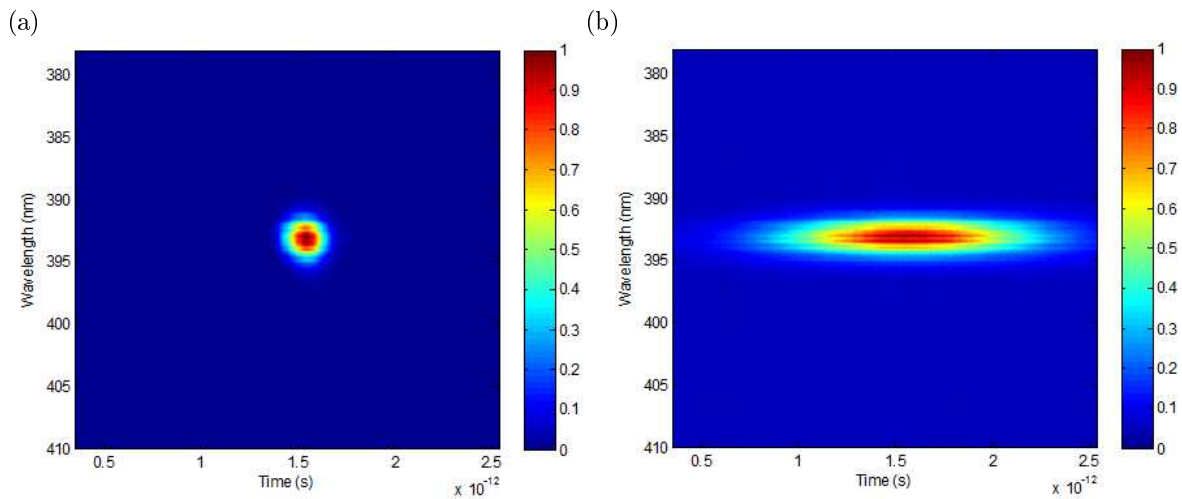


Figure 2.10: FROG measurement of a (a) single pulse and (b) chirped pulse.

In figure 2.10(a) the FROG trace of a single Gaussian pulse with a FWHM of 160 fs is shown with the wavelength range indicated on the y-axis, the time duration on the x-axis and the pulse intensity indicated by the colour bar. The pulse shows no change in the spectral components with time except for the expected Gaussian intensity envelope. In figure 2.10(b) a chirped pulse is shown with a longer pulse duration at 1 ps, due to the -45000 fs^2 quadratic chirp. In the case of SH FROG the pulse interacts with an identical replica of itself, including the phase information, in the nonlinear crystal. When these two replicas interact, as the one pulse moves over the second (due to the change in delay between the two pulses), the different wavelengths of the chirped pulses will interact to create new wavelengths. This interaction is symmetrical over the zero delay, which corresponds to the maximum overlap between the two pulses. Due to the identical nature of the pulses this produces a symmetrical FROG trace. The phase information can be extracted from the FROG traces by using a FROG iterative algorithm (Femtisoft Technologies, Frog3), with the phase information for the chirped pulse in figure 2.10(b) show in figure 2.11.

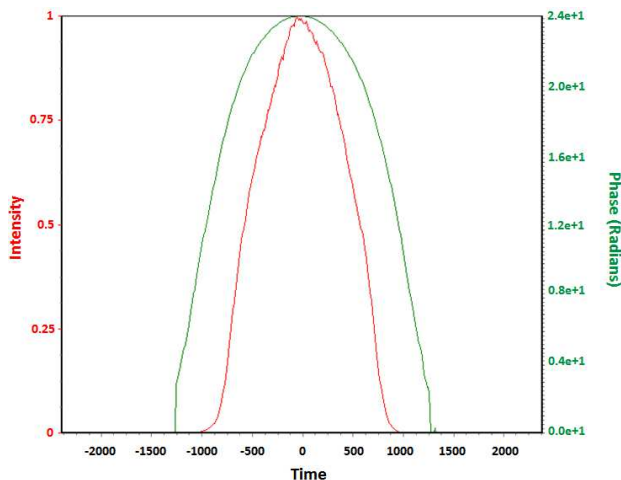


Figure 2.11: Extracted phase of the chirped pulse in figure 2.10(b).

From the extracted data in figure 2.11 the chirped pulse has a quadratic phase with a negative slope, as expected.

2.5 Difference Frequency Generation Experimental Setup

The main goal of this thesis is to investigate the generation of shaped pulses at wavelengths not accessible to the pulse shaper, such as the far infrared. To achieve this, we shape a single Gaussian pulse to have the desired shape at an accessible wavelength and convert the wavelength of a second single Gaussian pulse to the needed wavelength. The two pulses are used in a nonlinear process (difference frequency generation (DFG) with $\omega_1 - \omega_3 = \omega_2$ for our experimental setup) to generate a shaped pulse at the predetermined (inaccessible to our pulse shaper) wavelength.

Experimentally it is necessary to shape a pulse at the laser fundamental wavelength, 795 nm, and convert a second pulse to the needed wavelength. The experimental setup we use is shown in figure 2.12 consists out of three parts: pulse shaping, frequency conversion and the nonlinear mixing of the pulses.

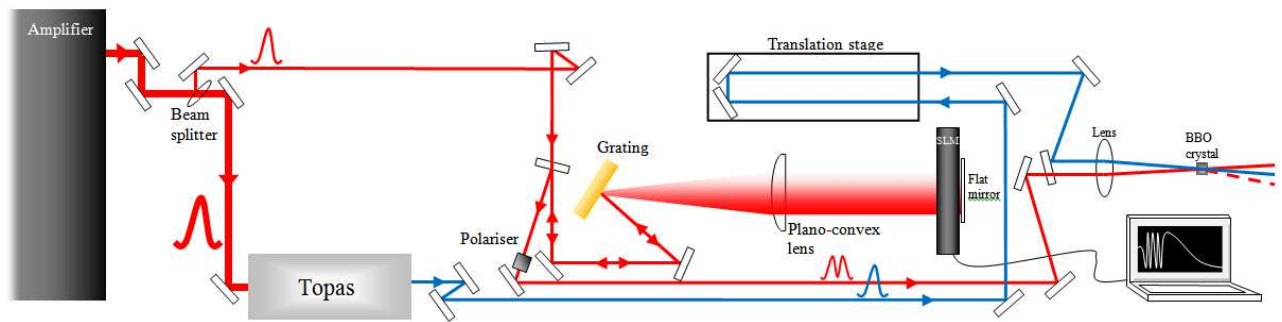


Figure 2.12: Difference frequency generation experimental setup.

In figure 2.12 the pulse at the fundamental wavelength is split into two parts with a 80/20 beam splitter. The 20% reflected light is shaped by a SLM in the folded 4f setup and the 80% transmitted light is frequency converted using an optical parametric amplifier (TOPAS) or a nonlinear crystal. Finally the two pulses are combined in a BBO crystal to generate the shaped pulse via DFG at the predetermined wavelength out of the SLM shaping range. In the following chapters we will discuss pulse shaping with the SLM to generate the shaped pulse, look briefly at frequency conversion using the TOPAS and simulate the DFG of shaped pulses inside nonlinear crystals while investigating the factors influencing the shape transfer. The simulations are compared to the experimental results which were generated using the setup in figure 2.12.

Chapter 3

Pulse Shaping Using a Spatial Light Modulator

Temporal femtosecond pulse shaping has been discussed in the previous chapter, looking at the experimental 4f setup for the SLM and two examples of shaped pulses: double pulses and linearly chirped pulses. In this chapter we investigate the spatial light modulator (SLM) and how temporal pulse shaping is done using the SLM, theoretically and experimentally.

3.1 SLM Liquid Crystal Display

The SLM contains two liquid crystal displays, which are controlled separately. Each display consists out of 640 individually controlled pixels with a small gap between each pixel, see figure 3.1 [1]. Each pixels contains a thin layer of nematic (aligned parallel but not in a rigid structure) liquid crystals, sandwiched between two parallel pieces of glass. The nematic nature ensures that the molecules have a defined orientation based on a magnetic field or alignment layer. The liquid crystals can be described as long, thin, rod-like molecules. The inside of the glass plates are coated with transparent electrically conductive Indium Tin Oxide with an alignment layer for geometric orientation of the liquid crystal molecules next to it.

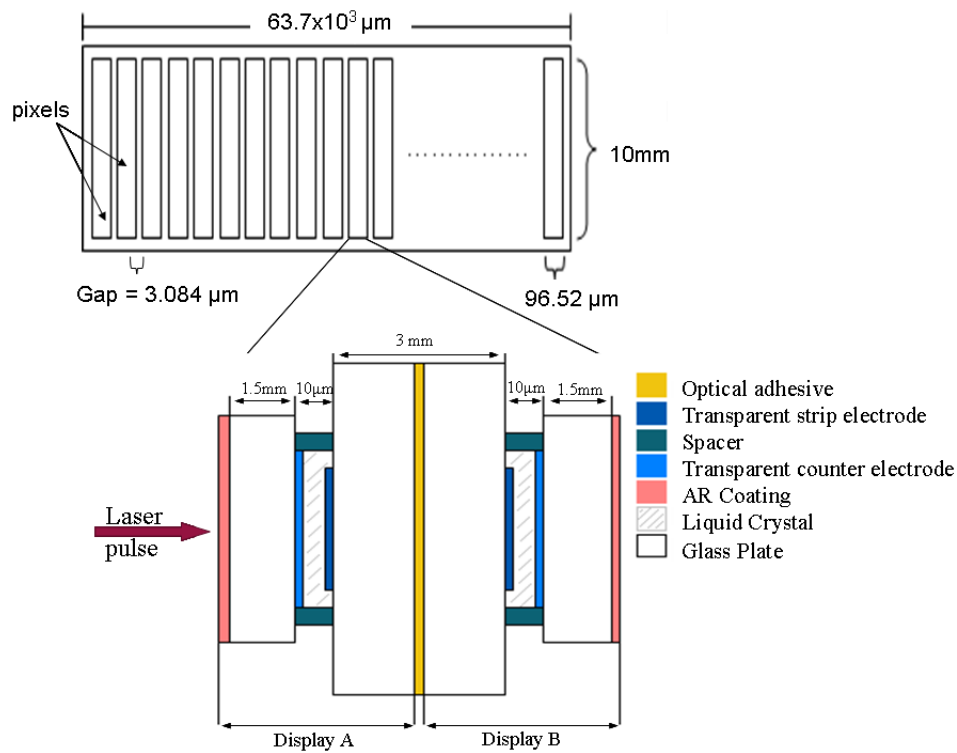


Figure 3.1: A liquid crystal display front view and a single pixel side view .[1]

The alignment layer, which has a series of parallel microscopic grooves, causes the liquid crystal molecules to orientate homogeneously in the direction defined by the grooves. Due to the directional dependence of the liquid crystal's physical properties, such as the crystal refractive index (meaning that the refractive index for the incoming radiation is dependent on the orientation of the liquid crystals), the liquid crystals can be described as an optical anisotropic material [1].

In the absence of an electric field the molecules are aligned with their long axis along the alignment layer, (see figure 3.2(a)). When an electric field is applied, the liquid crystal molecules tilt along the axis of the electric field, causing a change in the refractive index for the polarised light. The stronger the electric field, the more the liquid crystals will tilt in the direction of the applied field, see figure 3.2(b). This way it is possible to control the degree of molecular rotation which in turn determines the optical effect that the liquid crystals have on polarised light [1].

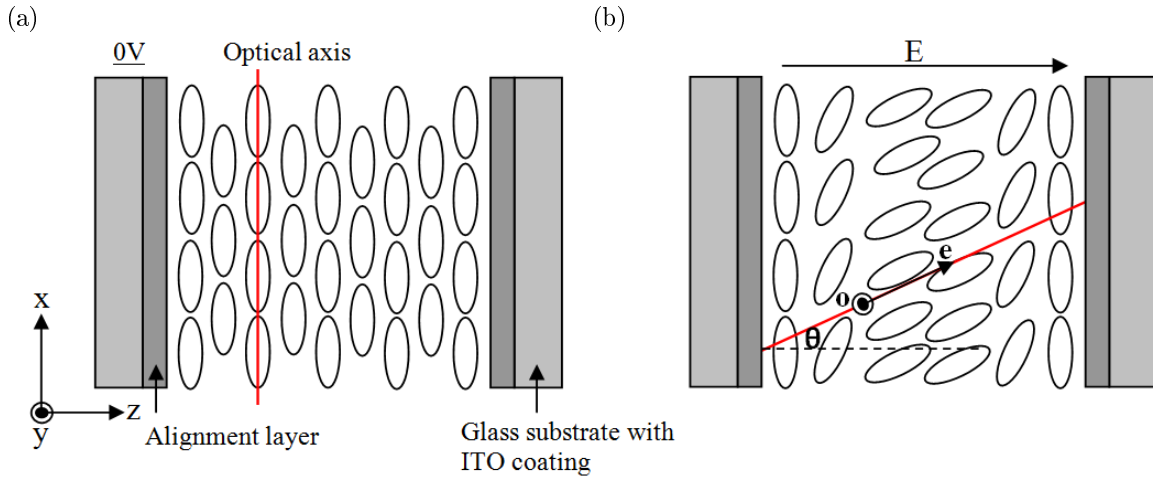


Figure 3.2: Cross section of a single liquid crystal cell with (a) $V = 0$ and (b) $V \neq 0$. [1]

The optical behavior of the liquid crystals can be compared to that of uni-axial birefringent crystals. In general a material is birefringent when the beam traveling along the z -axis is decomposed into an ordinary and extraordinary ray. The ordinary ray polarisation is perpendicular to the optical axis of the material, while the extraordinary ray is polarised along the material optical axis. Due to these different polarisations the ordinary and extraordinary rays see different refractive indices. The ordinary polarised ray's refractive index (n_o) is independent of the angle of the incoming ray with the optical axis while the extraordinary ray's refractive index (n_e) is dependent on the angle of the ray with the optical axis. The difference in refractive index is then $\Delta n = n_e - n_o$.

In figure 3.2 the x -axis is defined as the optical axis of the liquid crystals at 0 voltage. For birefringence to occur in the liquid crystals, the incoming light propagation must be in the z direction, perpendicular to the optical axis. When a voltage is applied and the liquid crystals rotate, the optical axis will rotate in the x - z plane with the crystals. The beam falling on the crystals is decomposed into the ordinary and extra-ordinary rays. The ordinary ray with the polarisation perpendicular to the optical axis (meaning polarisation in the y -direction in figure 3.2a), sees a constant refractive index (n_o) while the extraordinary ray, with polarisation along the optical axis (see figure 3.2b), refractive index is dependent on the orientation of the liquid crystals optical axis, $n_e(\phi)$. When a voltage is applied and the LC rotate, $n_e(\phi)$ will change while n_o will stay the same. This will cause a change in Δn with $\Delta n = n_e(\phi) - n_o$.

This effect of electrically controlled birefringence is used by the SLM for phase and amplitude modulation. In the absence of an electric field where $V = 0$, the maximum phase difference ($\Delta\phi_{\max}$) between

the ordinary and extraordinary beam will occur and can be expressed mathematically as

$$\Delta\phi_{\max} = 2\pi(n_e - n_o) \frac{d_{\text{LC}}}{\lambda_0}, \quad (3.1)$$

with the input wavelength λ_0 and d_{LC} the liquid crystal cell thickness [1]. When an electric field is applied in the z direction, the angle $\theta(V)$ between the direction of the incident wave and optical axis decreases continuously with increasing voltage, due to the rotation of the liquid crystals molecules. Due to the angle (and so also voltage) dependence of the extraordinary refractive index (n_e) the effective extraordinary refractive index will become $n_\theta(V)$ taking into account the polarisation angle with the liquid crystals optical axis; while n_o remains constant. From equation 3.1 the phase change at voltage can now be expressed as

$$\Delta\phi(V) = \frac{2\pi d}{\lambda} (n_\theta(V) - n_o) \quad \text{with} \quad n_\theta(\omega, V) = \frac{1}{\sqrt{\frac{\cos^2 \theta(V)}{n_o^2(\omega)} + \frac{\sin^2 \theta(V)}{n_e^2(\omega)}}}. \quad (3.2)$$

The dependence of the extraordinary refractive index on the voltage ($n_\theta(V)$) is non-trivial and therefore needs to be measured in order to calibrate the SLM. This will be done later in this chapter when measuring the voltage dependence of the transmission from the SLM. The phase retardation for the extraordinary polarised beam, which is voltage dependent, consists of the phase retardation induced by the liquid crystals (ϕ_{LC}) and the retardation due to the glass substrate the liquid crystal display is sandwiched between (ϕ_{glass})

$$\begin{aligned} \phi_e &= \phi_{\text{LC}} + 2\phi_{\text{glass}}, \\ &= \frac{\omega}{c} [n_{\text{LC}}(\omega, V) \cdot d_{\text{LC}} + 2n_{\text{glass}}(\omega) \cdot d_{\text{glass}}], \end{aligned}$$

with $\Delta n(\omega, V) = n_{\text{LC}}(\omega, V) - n_{o;\text{LC}}(\omega)$. Now we can write

$$\begin{aligned} \phi_e &= \frac{\omega}{c} [(n_{\text{LC}}(\omega, V) - n_{o;\text{LC}}(\omega) + n_{o;\text{LC}}(\omega)) \cdot d_{\text{LC}} + 2n_{\text{glass}}(\omega) \cdot d_{\text{glass}}], \\ &= \frac{\omega}{c} (\Delta n(\omega, V) \cdot d_{\text{LC}}) + \frac{\omega}{c} (n_{o;\text{LC}}(\omega) \cdot d_{\text{LC}} + 2n_{\text{glass}}(\omega) \cdot d_{\text{glass}}), \\ &= \Delta\phi(\omega, V) + \phi_{\text{fixed}}(\omega). \end{aligned}$$

The phase retardation can be divided into a constant part $\phi_{\text{fixed}}(\omega)$, due to the ordinary polarised wave's constant refractive index; and a voltage dependent part $\Delta\phi(\omega, V)$. The voltage dependent part is largest for zero voltage and disappears for high driving voltages [1]. The refractive index of the ordinary polarised wave is always $n_{\text{o;LC}}$ so that the retardation of that is always $\phi_{\text{fixed}}(\omega)$. This means that the phase retardation $\Delta\phi$ between the ordinary and extraordinary polarised wave can be expressed as

$$\Delta\phi = \phi_e - \phi_o = \Delta\phi(\omega, V) = \frac{\omega}{c} \Delta n(\omega, V) \cdot d_{\text{LC}}. \quad (3.3)$$

where ϕ_e and ϕ_o are the ordinary and extraordinary phase retardation of the light when applying voltage V .

3.2 Control of Phase and Amplitude

When the polarisation direction of the incident light is 45° with regard to the optical axis of the liquid crystals, the light wave will be decomposed into a component in the ordinary and extraordinary polarisation direction, as discussed in the previous section. These two components can be phase shifted with respect to each other by changing the optical axis of the liquid crystals through rotation, by applying a voltage on the displays [1]. Amplitude modulation is done by changing the polarisation using a liquid crystal display in conjunction with a polariser, that for instance, only lets light through polarised in the x-direction. In practice, amplitude modulation is done by applying a specific voltage on selected liquid crystal pixels, changing the phase difference between the ordinary and extraordinary beam. This rotates the polarisation of the light. When combining this with the polariser placed after the SLM only light polarised in the x direction will be transmitted, blocking all other polarisations. The transmitted light has not only an amplitude modulation but also a phase change, which is coupled to the amount of amplitude modulation. This means that an additional liquid crystal display is necessary in order to do either pure phase or pure amplitude modulation, or a combination of both.

The SLM utilises two liquid crystal displays (display A and display B) back-to-back (for simultaneous but independent phase and amplitude modulation) in such a manner that the direction of orientation of the alignment layers are perpendicular to each other, see figure 3.3(b). In each case the polarisation direction of the incident wave is at a 45° angle with regard to both alignment directions. Our experimental setup is folded as shown in figure 3.3(a) with figure 3.3(b) indicating the corresponding schematic setup.

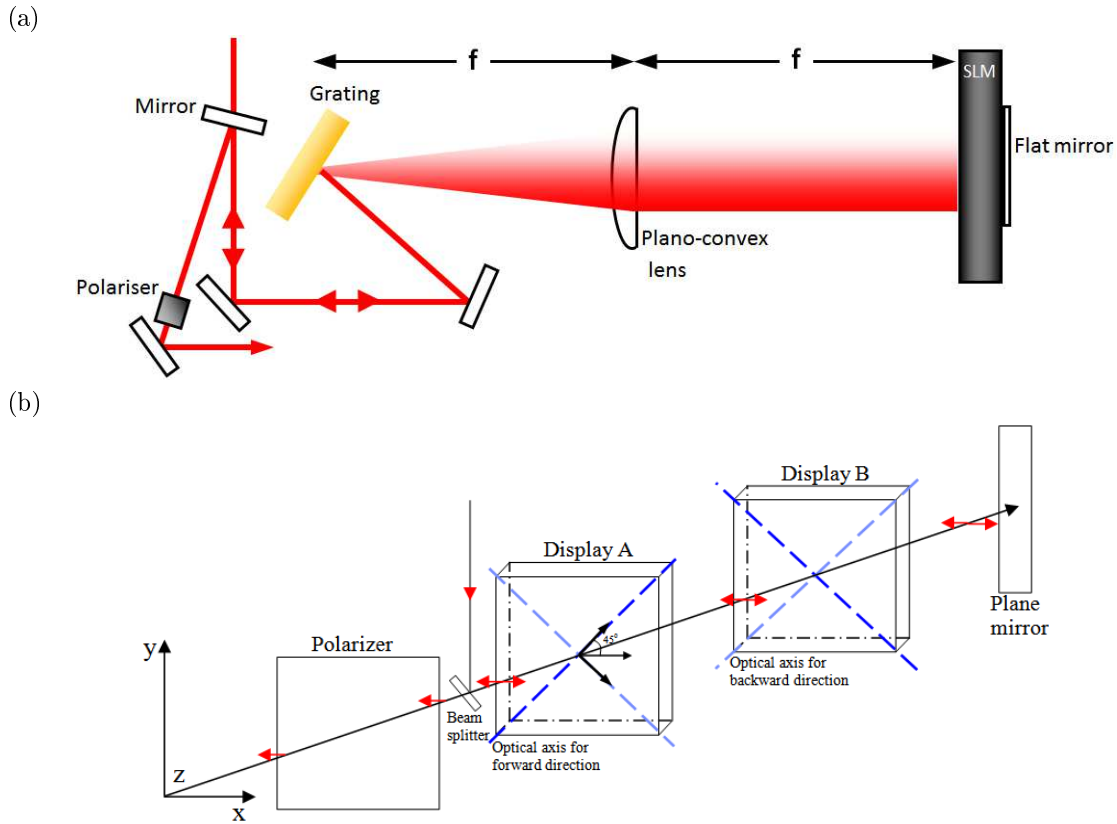


Figure 3.3: (a) Top: Experimental setup of a folded SLM configuration and (b) Bottom: schematic drawing showing the optical axis orientation for the folded SLM setup in (a).

The configuration in figure 3.3(b) can be described mathematically using Jones matrices. The red arrows indicate the path that the pulse travels, with respect to the optics mathematically described by the Jones matrices. We describe a liquid crystal cell in terms of Jones matrices as

$$\begin{bmatrix} \cos(\theta) & \sin(\theta) \\ -\sin(\theta) & \cos(\theta) \end{bmatrix} \begin{bmatrix} 1 & 0 \\ 0 & e^{i\Delta\phi} \end{bmatrix} \begin{bmatrix} \cos(-\theta) & \sin(-\theta) \\ -\sin(-\theta) & \cos(-\theta) \end{bmatrix},$$

where θ is the degree of liquid crystal rotation with respect to the optical axis, due to an applied voltage and $\Delta\phi$ the relative change in phase between the ordinary and extraordinary components of the wave due to the birefringence of the LC. The Jones matrix $\begin{bmatrix} \cos(\theta) & \sin(\theta) \\ -\sin(\theta) & \cos(\theta) \end{bmatrix}$ represents the rotation of the polarisation of the incoming light into the basis of the optical axis and $\begin{bmatrix} 1 & 0 \\ 0 & e^{i\Delta\phi} \end{bmatrix}$

represents the relative change in the phase between the ordinary and extraordinary polarised wave due to the rotation (θ) of the liquid crystals. After the phase retardation is added to the wave, the light polarisation is rotated back to the frame of the laboratory, $\begin{bmatrix} \cos(-\theta) & \sin(-\theta) \\ -\sin(-\theta) & \cos(-\theta) \end{bmatrix}$. The Jones matrices representing the horizontal polariser placed after the setup is

$$\begin{bmatrix} 1 & 0 \\ 0 & 0 \end{bmatrix}.$$

In the case of the second liquid crystal display the optical axis is rotated by an additional 90° , so that the angle θ will change signs. The exiting field after the horizontal polariser can thus be described by

$$\begin{aligned} \epsilon_{\text{out}} &= \begin{bmatrix} \frac{1}{2}e^{2i\Delta\phi_1} + \frac{1}{2}e^{2i\Delta\phi_2} \\ 0 \end{bmatrix} E_0 e^{i(\omega t - kz)}, \\ \epsilon_{\text{out}} &= \begin{bmatrix} 1 \\ 0 \end{bmatrix} \left(\frac{e^{(i\Delta\phi_1 - i\Delta\phi_2)} + e^{(i\Delta\phi_2 - i\Delta\phi_1)}}{2} \right) e^{i(\Delta\phi_1 + \Delta\phi_2)} E_0 e^{i(\omega t - kz)}, \\ &= \begin{bmatrix} 1 \\ 0 \end{bmatrix} \cos(\Delta\phi_1 - \Delta\phi_2) e^{i(\Delta\phi_1 + \Delta\phi_2)} E_0 e^{i(\omega t - kz)}, \end{aligned} \quad (3.4)$$

with $\epsilon_{\text{in}} = \begin{bmatrix} 1 \\ 0 \end{bmatrix} E_0 e^{i(\omega t - kz)}$ the input radiation and $\begin{bmatrix} 1 \\ 0 \end{bmatrix}$ representing light linearly (horizontally) polarised in the x-direction. $\Delta\phi_1$ and $\Delta\phi_2$ are the change in phase of the light due to rotation of the liquid crystal in display A and display B, respectively. The phase retardation of the liquid crystal displays act on the amplitude modulation (A) as well as the phase ϕ modulation, as stated previously. This dependence of the amplitude and phase on phase modulation can now be calculated from equation 3.4 as

$$A = \cos(\Delta\phi_1 - \Delta\phi_2) \quad (3.5)$$

$$\phi = \Delta\phi_1 + \Delta\phi_2, \quad (3.6)$$

with $\Delta\phi_1 = \frac{1}{2}(\phi + \arccos(A))$ and $\Delta\phi_2 = \frac{1}{2}(\phi - \arccos(A))$. This states that the amplitude modulation is determined by the difference in the phase change from the two displays and the resulting

phase modulation corresponds to the sum in phase change from the two displays. Pure amplitude modulation occurs when $\Delta\phi_1 = -\Delta\phi_2$ and pure phase modulation will occur when $\Delta\phi_1 = \Delta\phi_2$.

In order to generate a specific phase and/or amplitude modulation, it is necessary to know what the dependencies of the refractive indices are on the input light wavelength and SLM driving voltage [1]. These dependencies will be investigated in the next section. Liquid crystal modulators are configured for either phase-only or phase-and-amplitude pulse shaping and a maximum phase change of 2π is required for complete phase control [21].

Two dual liquid crystal SLMs (4 liquid crystal displays) can also be used for controlling the time-dependent polarisation profile of ultra short pulses. One limitation of using a liquid crystal SLM is the limited resolution of the displays [21] due to the pixels. Because the shaping is done in the spectral domain the spectrum of the pulse must be adequately sampled with the fixed pixels, which means that the spectrum must vary sufficiently slow so not to lose any sharp spectral features. This will be investigated more closely when simulating the SLM in section 3.5 later in this chapter.

3.3 Measurement of the Voltage Dependence

In order to shape light predictably using an SLM, it is necessary to relate the phase shift imposed on the light to the voltage applied on the liquid crystal displays [1]. By measuring the transmission T as a function of the driving voltage, using the setup shown in figure 3.4, the individual phase retardation of each liquid crystal pixel can be determined. From equation 3.5 we deduce that the transmission of the SLM can be related to the amplitude (equation 3.5) so that

$$\begin{aligned} T(V_1, V_2) &= \cos^2(\Delta\phi_1(V_1) - \Delta\phi_2(V_2)), \\ &= \frac{1}{2} \{1 + \cos(2\Delta\phi_1(V_1) - 2\Delta\phi_2(V_2))\}, \end{aligned} \quad (3.7)$$

where we now explicitly indicate the voltage dependencies of the phase shifts, $\Delta\phi(V)$.

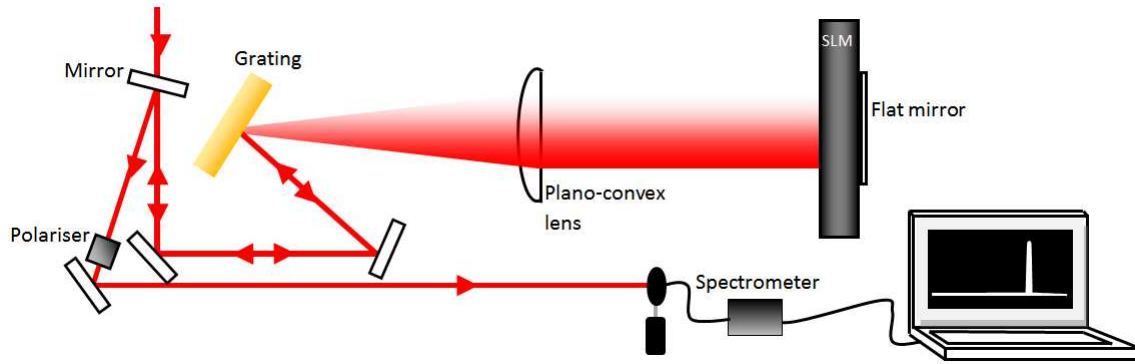


Figure 3.4: Calibration setup.

By setting the drive voltage of one of the liquid crystal cells to its maximum value, making it inactive and totally transmissive, the phase calibration can be done for the individual displays. The phase retardation of the liquid crystal cell that the maximum voltage was applied to becomes very small and can be approximated to zero. From the transmission T , the retardation $\Delta\phi$ of the second LC cell can be calculated

$$\begin{aligned}\Delta\phi_1(V_1) &= \Delta\phi_2(V_2^{\max}) \pm \frac{1}{2} \arccos \{2T(V_1, V_2^{\max}) - 1\}, \\ \Delta\phi_2(V_2) &= \Delta\phi_1(V_1^{\max}) \pm \frac{1}{2} \arccos \{2T(V_1^{\max}, V_2) - 1\}.\end{aligned}\quad (3.8)$$

The unknown constant terms in the above equations, $\Delta\phi_2(V_2^{\max})$ and $\Delta\phi_1(V_1^{\max})$, act as fixed offsets since the amplitude and phase is only dependent on a change in the phases, see equation 3.5 and 3.6 respectively. The same constant phase shift applied at all frequencies has no effect on the light wave, meaning that the equations can be simplified by assuming $\Delta\phi_2(V_2^{\max}) = 0$ and $\Delta\phi_1(V_1^{\max}) = 0$ [1]. To experimentally determine the transmission-voltage-graph of the separate liquid crystal display (e.g. B), the other display (e.g. A) has to be made inactive by applying the maximum voltage, see figure 3.5. The y-axis is the transmission of the light through the SLM display normalised using the maximum transmission value. The calibration curve (figure 3.5) was measured for the center wavelength (795 nm) using the femtosecond laser and a spectrometer, see figure 3.4. This setup makes it possible to measure the transmission curve for each wavelength of the pulse bandwidth. The transmission curve must be measured for both display A and display B.

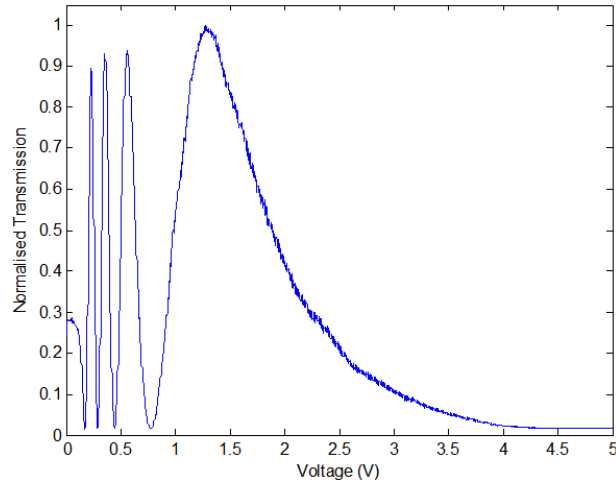


Figure 3.5: Measured Transmission-Voltage Graph for display B.

Figure 3.5 shows more oscillations in the transmission curve than in the literature [1]. This is due to the light passing through the liquid crystal displays twice, in our folded 4f setup, having twice the effect on the phase.

The phase retardation ($\Delta\phi$) is not just dependent on the voltage (V) but on the wavelength of the light wave as well. This dependence is due to the wavelength dependence of the ordinary and extraordinary polarised light refractive indices, ($\Delta n(\omega, V)$), see equation 3.3. This means that in order to generate an accurate phase modulation it is necessary to have knowledge of the liquid crystal refractive indices dependence on the light frequency as well as the driving voltage applied on the liquid crystal displays, $\Delta n(\omega, V)$. The frequency dependent difference between the ordinary and extraordinary refractive index follows directly from the frequency dependence of the maximum phase shift, if the liquid crystal cell thickness d_{LC} is known.

Since we know from equation 3.2 that

$$\begin{aligned} \Delta\phi(V) &= \frac{2\pi d}{\lambda} (n_{\theta}(V) - n_o) \text{ with} \\ \frac{1}{n_{\theta}^2(\omega, V)} &= \frac{\cos^2 \theta(V)}{n_o^2(\omega)} + \frac{\sin^2 \theta(V)}{n_e^2(\omega)}, \end{aligned}$$

it follows that

$$\begin{aligned} \Delta n(\omega, V) &= n_{\theta}(V) - n_o, \\ &= \sqrt{\frac{n_o^2(\omega) n_e^2(\omega)}{n_e^2(\omega) \cos^2 \theta(V) + n_o^2(\omega) \sin^2 \theta(V)}} - n_o(\omega), \end{aligned}$$

$$\begin{aligned}
&= \frac{n_o(\omega) n_e(\omega)}{\sqrt{n_o(\omega) + [n_e^2(\omega) - n_o^2(\omega)] \cos^2 \theta(V)}} - n_o(\omega), \\
\Delta n(\omega, V) &= n_o(\omega) \left(\frac{\frac{n_e(\omega)}{n_o(\omega)}}{\sqrt{1 + \left[\left(\frac{n_e(\omega)}{n_o(\omega)} \right)^2 - 1\right] \cos^2 \theta(V)}} - 1 \right), \\
\Delta n(\omega, V) &= n_o(\omega) f(\omega, V) \text{ with } f(\omega, V) = \frac{\frac{n_e(\omega)}{n_o(\omega)}}{\sqrt{1 + \left[\left(\frac{n_e(\omega)}{n_o(\omega)} \right)^2 - 1\right] \cos^2 \theta(V)}} - 1.
\end{aligned}$$

The frequency dependence of the function in the brackets, $f(\omega, V)$, can be neglected due to the refractive index ratio $\frac{n_e(\omega)}{n_o(\omega)}$ of the liquid crystals being near constant for each wavelength in our bandwidth [1]. Consequently

$$\Delta n(\omega, V) = n_o(\omega) \cdot f(V), \quad (3.9)$$

with $f(V)$ describing the voltage dependency and $n_o(\omega)$ the frequency dependent maximum difference in refractive indices; indicating that the frequency and voltage dependency of the optical anisotropy can be treated separately. The function $f(V)$ is standardised to have a maximum of 1 and represents the change in phase due to the changing voltage.

In our experiment the bandwidth of our beam is sufficiently narrow (10 - 15 nm), so that the change in the refractive indices due to the different wavelengths is very small (with the difference in the refractive index between 790 nm and 800 nm equal to 3.650×10^{-4}) giving negligible wavelength dependence. Due to the very small change in wavelength dependence in our setup, the calibration can be done for a single wavelength. In the case for larger bandwidths (shorter pulses) with the wavelength dependence much larger, using a spectrometer in the calibration process makes it possible to calibrate for each wavelength, effectively measuring a transmission curve for each wavelength in the laser bandwidth.

3.4 Calculating the Phase Calibration Curve

The typical voltage dependency $f(V)$ of the amplitude has been measured and is indicated in figure 3.5. From the measured curve we now calculate the change in phase ($\Delta\phi$) due to the voltage. In the experimental calibration setup the orthogonal polarisation (to the polarisation used for shaping) is used, so that the amplitude is written as $A = \sin(\Delta\phi(V))$ instead of equation 3.5 [1]. The ideal voltage

dependent transmission function can now be written as

$$T(V) = \sin^2(\Delta\phi(V)).$$

$\sin^2(x)$ has a period π so that the phase retardation $\Delta\phi(V)$ can then be written as

$$\Delta\phi(V) = k\pi \pm \arcsin \sqrt{\frac{T(V)}{T_0}}. \quad (3.10)$$

In the ideal case the transmission graph will reach “0” at the minimum and a consistent value T at the maximum voltage. When taking the experimental measurement, the transmission values T have to be standardised before equation 3.10 can be used to determine $\Delta\phi(V) = f(T)$. The background of the transmission is subtracted and normalised to the contrast

$$\frac{T}{T_0} = \frac{T_i - T_{\min}}{T_{\max} - T_{\min}},$$

where T_{\max} and T_{\min} are the extreme values adjacent to T_i , which is the transmission measurement at each voltage count i , see figure 3.6.

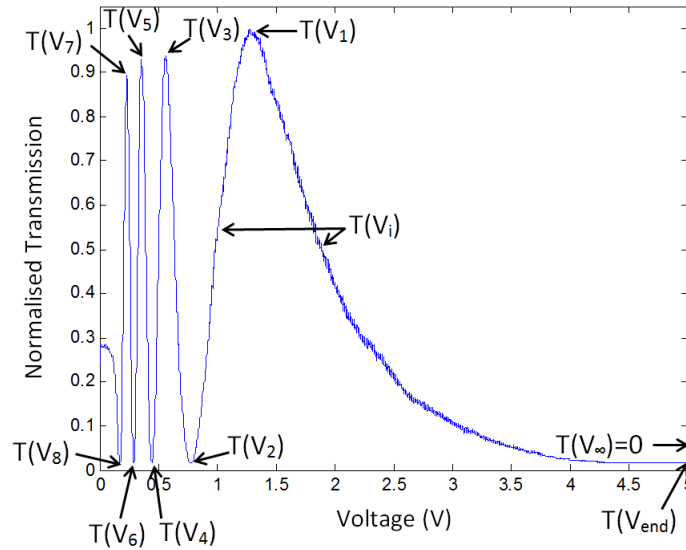


Figure 3.6: Standardisation of transmission values.

Each T value indicated on the y axis of figure 3.6 corresponds to a specific voltage (V). The ϕ dependence on voltage is calculated from equation 3.10 for different regions [1].

$$\Delta\phi(V) = 0 + \arcsin \sqrt{\frac{T(V) - T(V_{\text{end}})}{T(V_1) - T(V_{\text{end}})}}, \text{ for region } V_{\text{inf}} \text{ to } V_1$$

$$\Delta\phi(V) = \pi - \arcsin \sqrt{\frac{T(V) - T(V_2)}{T(V_1) - T(V_2)}}, \text{ for region } V_1 \text{ to } V_2.$$

In general, for region V_{2k} to V_{2k-1} (positive slope), $\Delta\phi(V) = k\pi - \arcsin \sqrt{\frac{T(V) - T(V_{2k})}{T(V_{2k-1}) - T(V_{2k})}}$ and for region V_{2k} to V_0 (negative slope), $\Delta\phi(V) = k\pi + \arcsin \sqrt{\frac{T(V) - T(V_{2k})}{T(V_{2k-1}) - T(V_{2k})}}$. The calculated $\Delta\phi$ is then plot against the corresponding count as shown is figure 3.7. A similar calculation is done for the second display using the measured transmission-voltage graph of the second display.

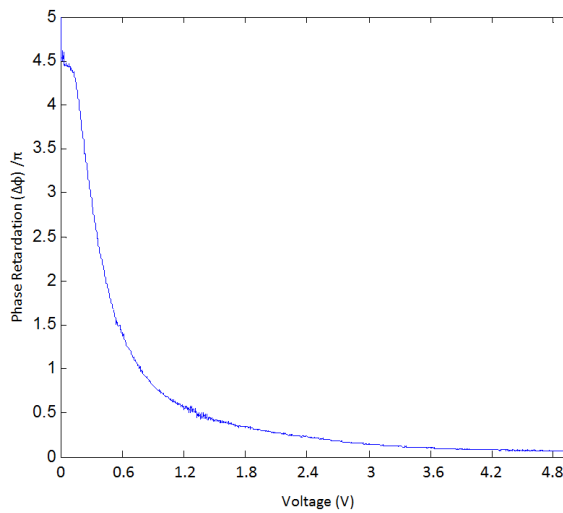


Figure 3.7: Calculated ϕ dependence.

After the calibration is done, $\Delta\phi_A$ and $\Delta\phi_B$ can be easily calculated for known amplitudes and phases and the corresponding count extracted from figure 3.7.

3.4.1 Creating a Double Pulse

As an example for creating a specific pulse shape, consider a double pulse where the electric field is described in the frequency domain.

$$E(\omega) = E_0 \sqrt{\frac{\pi}{\alpha}} e^{-(\omega - (1-\gamma)\omega_c)^2 / 4\alpha} \left[1 + e^{-i(\omega - (1-\gamma)\omega_c)\tau} \right], \quad (3.11)$$

with ω_c the carrier frequency, τ the delay between the two pulses and γ the parameter that allows tuning of the carrier phase in relation to the electric field envelope, so that the carrier phase is unchanged

when $\gamma = 0$ and the oscillation frequency matches the carrier frequency when $\gamma = 1$ [34]. We know from equation 2.9 that the transfer function, $H(\omega)$, can be calculated by dividing the Fourier transform of the wanted pulse shape (equation 3.11) by the Fourier transform of the input Gaussian pulse (equation 2.5) as follows

$$\begin{aligned} H(\omega) &= \frac{1}{2} \left[1 + e^{-i[\omega - (1-\gamma)\omega_c]\tau} \right] \\ &= \frac{1}{2} \left[1 + \cos([\omega - (1-\gamma)\omega_c]\tau) - i \sin([\omega - (1-\gamma)\omega_c]\tau) \right]. \end{aligned} \quad (3.12)$$

The real and imaginary parts of $H(\omega)$ are respectively:

$$\begin{aligned} \text{RE} &= \frac{1}{2} + \frac{1}{2} \cos([\omega - (1-\gamma)\omega_c]\tau) \text{ and} \\ \text{IM} &= \frac{1}{2} \sin([\omega - (1-\gamma)\omega_c]\tau). \end{aligned}$$

We can now determine the amplitude and phase modulations that will create the wanted double pulse in terms of the real and imaginary parts of the transfer function ($H(\omega)$)

$$\begin{aligned} \text{Amplitude} &= \sqrt{\text{RE}^2 + \text{IM}^2} \\ &= \sqrt{\left(\frac{1}{2} + \frac{1}{2} \cos([\omega - (1-\gamma)\omega_c]\tau) \right)^2 + \left(\frac{1}{2} \sin([\omega - (1-\gamma)\omega_c]\tau) \right)^2}, \end{aligned} \quad (3.13)$$

$$\text{Phase} = \arctan\left(\frac{\text{IM}}{\text{RE}}\right) = \arctan\left(\frac{\sin([\omega - (1-\gamma)\omega_c]\tau)}{1 + \cos([\omega - (1-\gamma)\omega_c]\tau)}\right). \quad (3.14)$$

Due to the gaps between the pixels of the SLM displays, 3% unshaped light will pass through and appear at $\tau = 0$ as back ground radiation. The modulation from equation 3.13 and 3.14 is used as the amplitude and phase respectively, see figure 3.8(a).

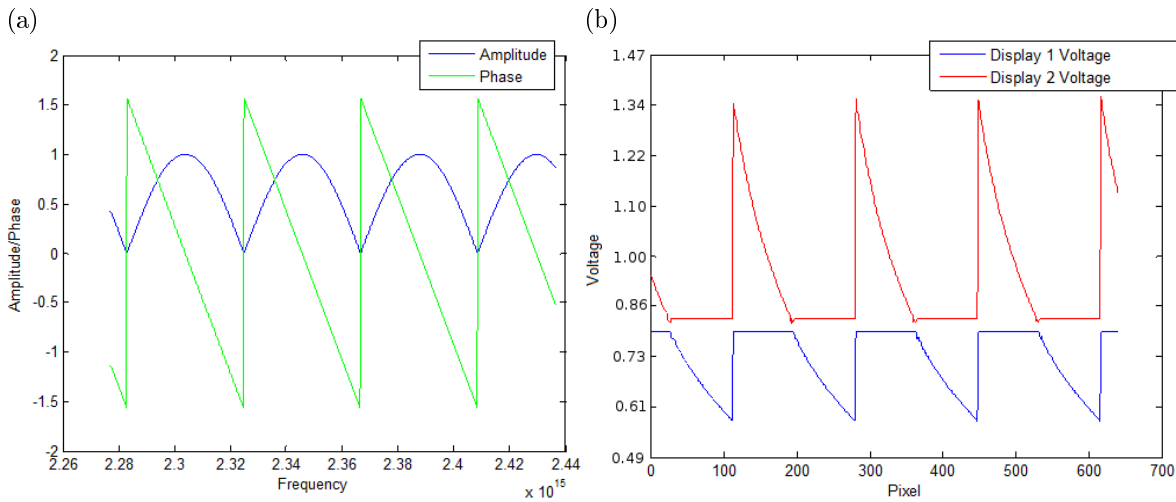


Figure 3.8: a) Amplitude and Phase modulation and b) corresponding voltage counts for a 150 fs double pulse.

The voltage patterns corresponding to the amplitude and phase in figure 3.8(a) can now be calculated using equations 3.5 and 3.6. The necessary voltages to create the phase changes, $\Delta\phi_1$ and $\Delta\phi_2$, are extrapolated from the calculated phase dependence curve in figure 3.7. This yields the voltage patterns shown in figure 3.8(b) which are programmed onto the SLM to create the double pulse.

3.5 Simulating the SLM

When shaping with a SLM it is important to remember that the shaper displays consist out of liquid crystal pixels, so that the transfer function applied to the pulse is not continuous, but pixelated. This means that the calculated or simulated shape produced by the shaper will not be identical to the experimentally shaped pulse if the shaper is assumed to be ideal, due to the discrete nature of the real SLM display. In this section we investigate the influence of a pixelated shaper on the generated pulse shape by shaping a double pulse and comparing the results from a ideal shaper and discrete (pixelated) shaper, for instance an SLM. The same response function, tailored to create a double pulse with a 250 fs separation and 100 fs FWHM, are used for both cases. The response function is continuous for the ideal shaper and made discrete to correspond to the SLM pixelated display for the case of a discrete shaper. The ideal continuous response function in figure 3.9(a) is generated using equation 3.12, with $\tau = 250$ fs and $\gamma = 0$.

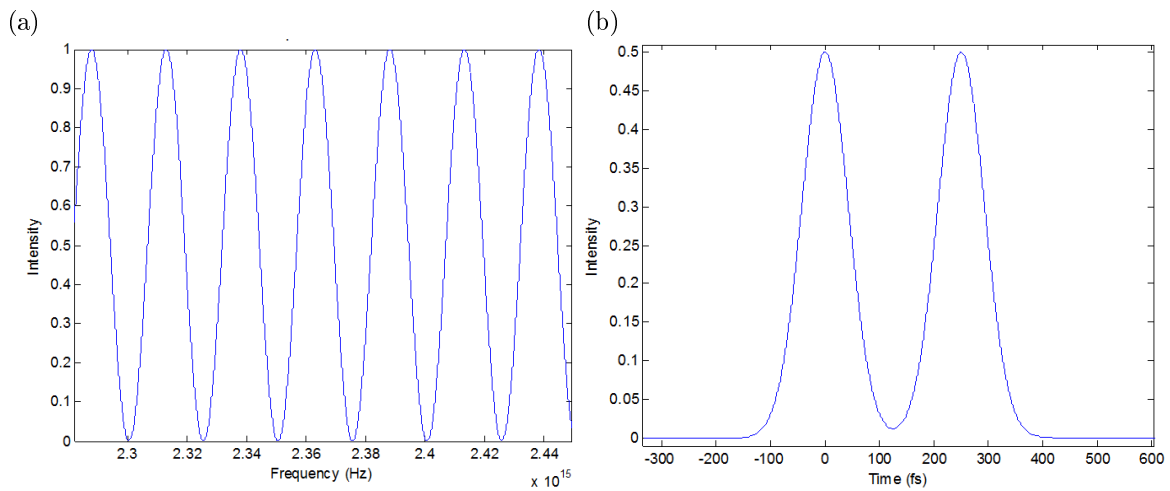


Figure 3.9: Simulating an ideal shaper with (a) a continuous response function ($H(\omega)$) for a 250 fs double pulse and (b) generated 250 fs double pulse.

By multiplying the response function in figure 3.9(a) with the Fourier transform of the input 100 fs Gaussian pulse (see equation 2.9), an ideal double pulse is created with a pulse separation of 250 fs and with each peak having a FWHM of 100 fs, see figure 3.9(b).

Next we investigate the effect of the pixelated shaper (SLM) used in our experiment, by simulating the transfer function used in the continuous case as discretised, see figure 3.10(a) and a zoomed half oscillation in figure 3.10(b). The factors determining the amount of discretisation are the pulse bandwidth, the amount of illuminated pixels and the size of the pixels. These factors have been discussed previously in sections 2.1, 2.3 and 3.1 respectively. The gaps between the pixels are not taken into account in this simulation, only the discreet nature of the SLM display is investigated.

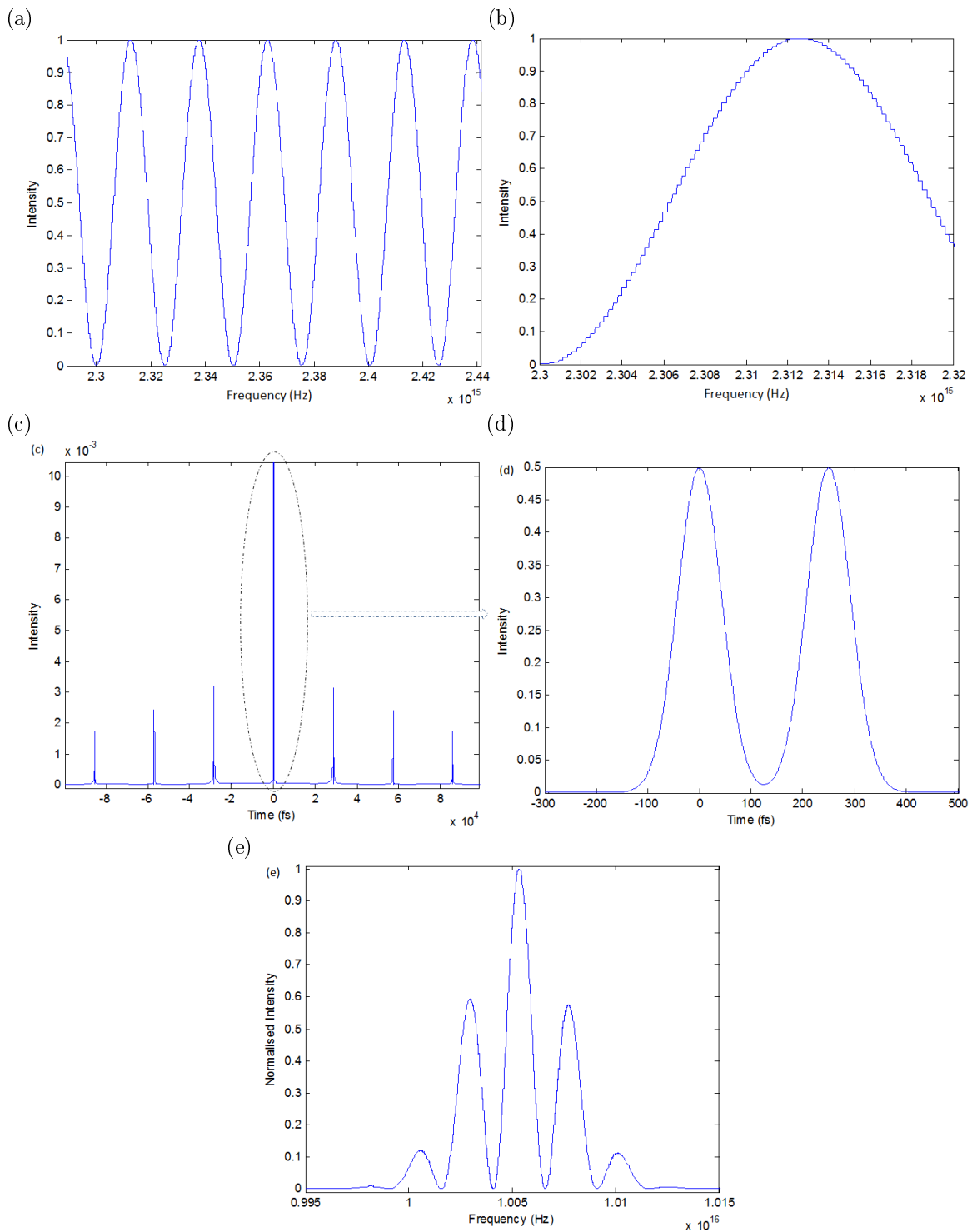


Figure 3.10: Simulating a discrete shaper with (a) pixelated response function for a 250 fs double pulse between selected frequencies, (b) half an oscillation of response function, (c) the generated 250 fs double pulse zoomed in on the x-axis to show the replicas, (d) the double pulse and the (e) corresponding spectrum of the shaped pulse.

With the pixelated response function, see figure 3.10(a) and (b), the generated double pulse, has replicas at constant intervals of 28.6 ps, see figure 3.10(c) zoomed in on the x-axis. The replicas are four orders of magnitude smaller than the main peak and can be considered negligible. The pre-pulses in figure 3.10(c) appear earlier than $t = 0$ due to the Fourier transform integrating over negative frequencies, with the frequency range from $-\infty$ to ∞ . When looking closer at the double pulse figure 3.10(d) the separation between the peaks are 250 fs with each peak having a 100 fs FWHM, identical to the shaped pulse generated by the ideal continuous response function. The larger the separation between the two pulses, the more pixelated the response function becomes and the larger the replicas. This is due to the response function for a double pulses with larger temporal pulse separation having more oscillations than pulses with smaller separations. More detail in the response function will fall away due to pixelation, creating larger replicas.

The size of the pixels determines the discrete nature of the response function, with the relation: replica spacing $\sim 1/\text{pixel width}$; the larger pixels will have more frequencies corresponding to one pixel and the steps in the response function will become larger, causing the distance between the replicas to be smaller. This means that there is a temporal shaping window, due to the size of the pixels, that has to be considered when doing experiments, fortunately the replicas in our experiments are spaced sufficiently far enough apart (28.6 ps) to not significantly influence our experiment. The corresponding shaped spectrum of the double pulse, $E_{\text{out}}(\omega)$, is indicated in figure 3.10(e) and corresponds to a Gaussian pulse, $E_{\text{in}}(\omega)$, multiplied by the response function.

3.5.1 Damage Threshold of SLM

It is important to know what laser intensity is safe to use with the SLM so as not to damage the liquid crystal displays. The liquid crystal pixels damage threshold can be calculated using the provided data from the manufacturer [1]. The peak intensity damage threshold of the SLM is given in the SLM manual [1] as $1100 \frac{\mu\text{J}}{\text{cm}^2}$ for a 250 fs pulses at 790 nm with a 1.85 kHz repetition rate, so that the damage threshold for the peak intensity can be calculated as

$$\begin{aligned} \text{Peak intensity} &= \frac{\text{Energy}}{\text{Pulses duration} \times \text{Area}} \\ &= \frac{1100}{(250 \times 10^{-15}) \text{ s.cm}^2} \frac{\mu\text{J}}{\text{cm}^2} = 4.4 \frac{\text{GW}}{\text{cm}^2}. \end{aligned}$$

Next we calculate the peak intensity of the amplifier output used in our setup, which produces 1W at

a 1 kHz repetition rate. We assume that our average pulse duration is 100 fs, and that the SLM is operated in a 4f setup where the spot size, illuminating the active area of the SLM display, is significantly larger than the spot size of the amplifier beam due to the grating and collimating lens. The laser beam area is calculated as $(l \times h)$, with the length and height of the laser beam spot $3 \times 1 \text{ cm}^2$. The energy of one pulse is then calculated as

$$\text{Energy} = \frac{\text{Average power}}{\text{Rep rate}} = \frac{1}{1 \times 10^3} \frac{\text{W}}{\text{pulses/sec}} = 1000 \mu\text{J},$$

with the repetition rate from our amplifier $1 \text{ kHz} = 1000 \text{ pulses/sec}$. The peak intensity of one pulse can now be calculated to be

$$\frac{1000}{100 \times 10^{-15} \times (3 \times 1)} \frac{\mu\text{J}}{\text{s.cm}^2} = 3.33 \frac{\text{GW}}{\text{cm}^2}.$$

This peak intensity of our pulse is lower than the peak intensity damage threshold of the SLM and we conclude that the amplified beam is safe to use on the SLM in our 4f setup.

Chapter 4

Difference Frequency Mixing

Second order nonlinear processes are used to generate new frequencies by implementing second harmonic generation, sum-frequency generation, difference frequency generation (DFG) or more [27]. In these nonlinear processes, energy is converted from the input electromagnetic fields interacting in a nonlinear medium to generate a new field under the condition $\omega_p - \omega_s = \omega_i$, where $\omega_j = \frac{2\pi c}{\lambda_j}$ is the angular frequency of the femtosecond pulse, with $j = p, s$ or i representing the pump pulse (p), signal pulse (s) and idler pulse (i) respectively. The amount of light generated through a nonlinear process as well as the direction of the generated field's polarisation is dependent on the second order susceptibility $\chi^{(2)}$. $\chi^{(2)}$ is the third order tensor characteristic to the nonlinear medium where the non linear process takes place. The frequency conversion is most efficient when there is phase matching, i.e when the condition $\tilde{k}_p - \tilde{k}_s = \tilde{k}_i$ is met, with $k_j = \frac{2\pi n_j}{\lambda_j}$ the wave number and n the refractive index.

In this chapter we develop a model to investigate the generation of a shaped femtosecond pulse at a wavelength inaccessible to the pulse shaper, by using DFG, building on the work of previous authors mentioned in chapter 1. The two input pulses, with frequency ω_s (signal) and ω_p (pump), interact in a nonlinear medium, such as a GaSe or BBO crystal, to generate an idler frequency ω_i where $\omega_i = \omega_p - \omega_s$. GaSe and BBO crystals are uni-axial, which means that they have one optical axis. There are several polarisation phase matching schemes in uni-axial crystals, depending on the orientation of the crystal. One example is type II phase matching, which occurs when the signal and idler pulses have perpendicular polarisations, $\omega_i(e) = \omega_p(e) - \omega_s(o)$ and this scheme is considered for the nonlinear process. We use the model to identify, investigate and finally predict the parameters for optimal transfer of a temporally shaped pulse to the near IR and Far IR wavelength regimes as well as the

transfer efficiency.

4.1 Theory

As background material we explicitly derive the wave equation for light traveling through a nonlinear medium, following broadly the methods in Meystre [35] and Boyd [36]. We start with Maxwell's equations

$$\nabla \cdot \tilde{\mathbf{D}} = \tilde{\rho}, \quad (4.1)$$

$$\nabla \cdot \tilde{\mathbf{B}} = 0, \quad (4.2)$$

$$\nabla \times \tilde{\mathbf{E}} = -\frac{\partial \tilde{\mathbf{B}}}{\partial t}, \quad (4.3)$$

$$\nabla \times \tilde{\mathbf{H}} = \frac{\partial \tilde{\mathbf{D}}}{\partial t} + \tilde{\mathbf{J}}, \quad (4.4)$$

where $\tilde{\mathbf{D}}$ represents the electric displacement field, $\tilde{\mathbf{B}}$ is the magnetic field, $\tilde{\mathbf{E}}$ the electric field, $\tilde{\mathbf{H}}$ the magnetic field strength, $\tilde{\mathbf{J}}$ the current density and $\tilde{\rho}$ the charge density [36]. The tilde ($\tilde{}$) is used to indicate rapid temporal variation of the field. We assume that the medium contains no free charges or currents, so that $\tilde{\rho} = 0$, $\tilde{\mathbf{J}} = 0$ and that the medium is not magnetic $\tilde{\mathbf{B}} = \mu_0 \tilde{\mathbf{H}}$, with μ_0 the permeability. We write the electric displacement ($\tilde{\mathbf{D}}$) in terms of the electric field ($\tilde{\mathbf{E}}$) and polarisation ($\tilde{\mathbf{P}}$) so that $\tilde{\mathbf{D}} = \epsilon_0 \tilde{\mathbf{E}} + \tilde{\mathbf{P}}$, with ϵ_0 the permittivity of free space. Because we are working in a nonlinear medium (nonlinear crystal) the polarisation vector ($\tilde{\mathbf{P}}$) depends nonlinearly on the local value of the electric field strength ($\tilde{\mathbf{E}}$) [36]. If we take the curl of the electric field, equation 4.3, we have

$$\begin{aligned} \nabla \times \nabla \times \tilde{\mathbf{E}} &= \nabla \times \left(-\frac{\partial \tilde{\mathbf{B}}}{\partial t} \right), \\ \nabla \times \nabla \times \tilde{\mathbf{E}} &= \nabla \times \left(-\mu_0 \frac{\partial \tilde{\mathbf{H}}}{\partial t} \right), \\ \nabla \times \nabla \times \tilde{\mathbf{E}} &= -\mu_0 \left(\nabla \times \frac{\partial \tilde{\mathbf{H}}}{\partial t} \right), \end{aligned}$$

From equation 4.4 we can write $\nabla \times \tilde{\mathbf{H}} = \frac{\partial \tilde{\mathbf{D}}}{\partial t}$ since $\tilde{\mathbf{J}} = 0$, so that we have

$$\nabla \times \nabla \times \tilde{\mathbf{E}} + \mu_0 \left(\frac{\partial^2 \tilde{\mathbf{D}}}{\partial t^2} \right) = 0,$$

$$\begin{aligned}\nabla \times \nabla \times \tilde{\mathbf{E}} + \mu_0 \epsilon_0 \frac{\partial^2 \tilde{\mathbf{E}}}{\partial t^2} &= -\mu_0 \frac{\partial^2 \tilde{\mathbf{P}}}{\partial t^2}, \\ \nabla \times \nabla \times \tilde{\mathbf{E}} + \frac{1}{c^2} \frac{\partial^2 \tilde{\mathbf{E}}}{\partial t^2} &= -\frac{1}{\epsilon_0 c^2} \frac{\partial^2 \tilde{\mathbf{P}}}{\partial t^2},\end{aligned}$$

where $\mu_0 \epsilon_0 = \frac{1}{c^2}$. Using the identity $\nabla \times \nabla \times \tilde{\mathbf{E}} = \nabla (\nabla \cdot \tilde{\mathbf{E}}) - \nabla^2 \tilde{\mathbf{E}}$ with $\nabla (\nabla \cdot \tilde{\mathbf{E}}) = 0$, since there are no free charges, we can write

$$\begin{aligned}-\nabla^2 \tilde{\mathbf{E}} + \frac{1}{c^2} \frac{\partial^2 \tilde{\mathbf{E}}}{\partial t^2} &= -\frac{1}{\epsilon_0 c^2} \frac{\partial^2 \tilde{\mathbf{P}}}{\partial t^2}, \\ \nabla^2 \tilde{\mathbf{E}} - \frac{1}{\epsilon_0 c^2} \frac{\partial^2 \tilde{\mathbf{D}}}{\partial t^2} &= 0.\end{aligned}$$

$\tilde{\mathbf{P}}$ can be separated into its linear and nonlinear part $\tilde{\mathbf{P}} = \tilde{\mathbf{P}}^{(L)} + \tilde{\mathbf{P}}^{(NL)}$, with $\tilde{\mathbf{P}}^{(L)}$ linearly dependent on the electric field strength $\tilde{\mathbf{E}}$. Similarly $\tilde{\mathbf{D}}$ can be written as $\tilde{\mathbf{D}} = \tilde{\mathbf{D}}^{(L)} + \tilde{\mathbf{P}}^{(NL)}$, so that

$$\nabla^2 \tilde{\mathbf{E}} - \frac{1}{c^2 \epsilon_0} \frac{\partial^2 \tilde{\mathbf{D}}^{(L)}}{\partial t^2} = \frac{1}{\epsilon_0 c^2} \frac{\partial^2 \tilde{\mathbf{P}}^{(NL)}}{\partial t^2}. \quad (4.5)$$

In a dispersive medium each frequency component of the field must be considered separately so that we represent the electric field as the sum of the various frequency components so that $\tilde{\mathbf{E}}(\mathbf{r}, t) = \sum_{\mathbf{n}} \tilde{\mathbf{E}}_{\mathbf{n}}(\mathbf{r}, t)$, with \mathbf{n} representing each frequency component and \mathbf{r} the position in the medium, similar for $\tilde{\mathbf{D}}^{(L)}(\mathbf{r}, t)$ and $\tilde{\mathbf{P}}^{(NL)}(\mathbf{r}, t)$. Neglecting dissipation in the field, the relationship between the electric displacement and electric field can be written as $\tilde{\mathbf{D}}_{\mathbf{n}}^{(L)}(\mathbf{r}, t) = \epsilon_0 \epsilon^{(L)}(\omega_{\mathbf{n}}) \cdot \tilde{\mathbf{E}}_{\mathbf{n}}(\mathbf{r}, t)$ with $\epsilon^{(L)}$ the frequency-dependent dielectric tensor.

We are simulating type II frequency generation in two uni-axial nonlinear crystals, GaSe and BBO, with the pump wave (ω_p , polarisation e) and the signal wave (ω_s , polarisation o) functioning as the input and producing an idler wave (ω_i , polarisation e), obeying the frequency relation $\omega_i = \omega_p - \omega_s$. The type of frequency generation determines which polarisations of the beams (o or e) will interact, which in turn determines the relevant refractive indices, $n_e(\omega_j)$ or $n_o(\omega_j)$.

Consider 4.5 in the vicinity of some frequency ω_j

$$\nabla^2 \tilde{\mathbf{E}}_j - \frac{\epsilon^{(L)}(\omega_j)}{c^2} \frac{\partial^2 \tilde{\mathbf{E}}_j}{\partial t^2} = \frac{1}{\epsilon_0 c^2} \frac{\partial^2 \tilde{\mathbf{P}}_j^{(NL)}}{\partial t^2} \quad (4.6)$$

with ω_j the center frequency of the pulse and $j = p, s$ or i . The electric field and polarisation are expressed in t and Z , for movement in 1 dimension, to approximate collinear movement of the

pulses so that the electric field of the pump pulse can be described as $\tilde{\mathbf{E}}_p = E_p(Z, t)e^{i(k_p Z - \omega_p t)}$ [35], with $E_p(Z, t)$ the amplitude envelope of the electric field and $e^{i(k_p Z - \omega_p t)}$ the oscillating electric field, which varies with the carrier frequency so that the envelope varies on the scale of $1/k_p$, which is much slower than the oscillating field. The polarisation of the pump pulse can be described as $\tilde{\mathbf{P}}_p = 4\epsilon_0 d_{\text{eff}} E_s(Z, t)e^{i(k_s Z - \omega_p t)} E_i(Z, t)e^{i(k_i Z - \omega_p t)}$ [35]. Inserting the electric field and polarisation into equation 4.6, with Z representing the spatial position of the pulse in the crystal [36], the interaction of the pulses can be expressed as

$$\begin{aligned} \frac{\partial^2 \tilde{\mathbf{E}}_p}{\partial Z^2} - \frac{\epsilon^{(L)}(\omega_p)}{c^2} \frac{\partial^2 \tilde{\mathbf{E}}_p}{\partial t^2} &= \frac{1}{\epsilon_0 c^2} \frac{\partial^2 \tilde{\mathbf{P}}_p}{\partial t^2}, \\ \frac{\partial^2 (E_p(Z, t)e^{i(k_p Z - \omega_p t)})}{\partial Z^2} - \frac{\epsilon^{(L)}(\omega_p)}{c^2} \frac{\partial^2 (E_p(Z, t)e^{i(k_p Z - \omega_p t)})}{\partial t^2} &= \\ \frac{1}{\epsilon_0 c^2} \frac{\partial^2 (4\epsilon_0 d_{\text{eff}} E_s(Z, t)e^{i(k_s Z - \omega_p t)} E_i(Z, t)e^{i(k_i Z - \omega_p t)})}{\partial t^2}, & \\ \left(\frac{\partial^2 E_p(Z, t)}{\partial Z^2} + 2ik_p \frac{\partial E_p(Z, t)}{\partial Z} - k_p^2 E_p(Z, t) \right) e^{i(k_p Z - \omega_p t)} - & \\ \frac{\epsilon^{(L)}(\omega_p)}{c^2} \left(\frac{\partial^2 E_p(Z, t)}{\partial t^2} - 2i\omega_p \frac{\partial E_p(Z, t)}{\partial t} - \omega_p^2 E_p(Z, t) \right) e^{i(k_p Z - \omega_p t)} &= \\ -\frac{1}{\epsilon_0 c^2} 8i\epsilon_0 d_{\text{eff}} \omega_p \left(\frac{\partial E_s(Z, t)}{\partial t} E_i(Z, t) + E_s(Z, t) \frac{\partial E_i(Z, t)}{\partial t} + \frac{\omega_p}{2i} E_s(Z, t) E_i(Z, t) \right) e^{i[(k_s + k_i)Z - \omega_p t]}. & \end{aligned}$$

We assume the slowly varying envelope approximation, where the oscillating electric field varies on a much more rapid time scale than the envelope so that the fast oscillating parts can be neglected and the following applies, i.e. $\left| \frac{\partial^2 E_p}{\partial Z^2} \right| \ll \left| k_p \frac{\partial E_p}{\partial Z} \right|$, $\left| \frac{\partial^2 E_p}{\partial t^2} \right| \ll \left| \omega_p \frac{\partial E_p}{\partial t} \right|$ and $\left| \frac{\partial E_p}{\partial t} \right| \ll |\omega_p E_p|$ [36]. The wave equation becomes

$$\frac{\partial E_p(Z, t)}{\partial Z} + \frac{1}{v_p} \frac{\partial E_p(Z, t)}{\partial t} = \frac{i\omega_p \chi_{\text{eff}}^{(2)}}{n_p c} E_s(Z, t) E_i(Z, t) e^{i(k_s + k_i - k_p)Z},$$

with $v_p = \frac{c}{n_p}$ the phase velocity of the pump pulse in the birefringent medium, $n(\omega_p)^2 = \epsilon^{(L)}(\omega_p)$ the refractive index, $k_p = \frac{n_p \omega_p}{c}$ the wave number and $d_{\text{eff}} = \frac{1}{2} \chi_{\text{eff}}^{(2)}$ representing the nonlinear susceptibility. E_p is the amplitude of the wave at a specific point in time and space and ω_p the center frequency of the pulse. The frequency bandwidth of the pulses are sufficiently narrow so that the dispersion in the medium can be approximated as linear and so the relationship between the frequency (ω) and

wavenumber (k) can be approximated as linear as well, the group velocity of the pulses are then $\frac{\partial\omega}{\partial k} = \text{constant}$ and equal to the phase velocity $v_p = \frac{c}{n_p}$.

$$\frac{\partial E_p(Z, t)}{\partial Z} v_p + \frac{\partial E_p(Z, t)}{\partial t} = \frac{i\omega_p \chi_{\text{eff}}^{(2)}}{n_p c} v_p E_s(Z, t) E_i(Z, t) e^{i(k_i + k_s)Z - ik_p Z}. \quad (4.7)$$

Equation 4.7 can now be applied to each electric field participating in the nonlinear interaction in order to yield the coupled partial differential equation for the pump, signal and idler pulse with the refractive index dependent on the wavelength $n(\lambda)$. Hence forth we write $E_j(Z, t)$ as E_j with the time and spatial dependence implied and with $E_j^*(\omega) = E_j(-\omega)$. The coupled partial equation for E_s and E_i are then

$$\begin{aligned} \frac{\partial E_s}{\partial Z} v_s + \frac{\partial E_s}{\partial t} &= \frac{i\omega_s \chi_{\text{eff}}^{(2)}}{n_s c} v_s E_p E_i^* e^{i(k_p - k_i)Z - ik_s Z}, \\ \frac{\partial E_i}{\partial Z} v_i + \frac{\partial E_i}{\partial t} &= \frac{i\omega_i \chi_{\text{eff}}^{(2)}}{n_i c} v_i E_p E_s^* e^{i(k_p - k_s)Z - ik_i Z}. \end{aligned}$$

By defining $k_p - k_s - k_i$ as Δk , we have

$$\begin{aligned} \frac{\partial E_s}{\partial Z} v_s + \frac{\partial E_s}{\partial t} &= \frac{i\omega_s \chi_{\text{eff}}^{(2)}}{n_s c} v_s E_p E_i^* e^{i\Delta k Z}, \\ \frac{\partial E_p}{\partial Z} v_p + \frac{\partial E_p}{\partial t} &= \frac{i\omega_p \chi_{\text{eff}}^{(2)}}{n_p c} v_p E_s E_i e^{-i\Delta k Z}, \\ \frac{\partial E_i}{\partial Z} v_i e^{-i\Delta k Z} + \frac{\partial E_i}{\partial t} e^{-i\Delta k Z} &= \frac{i\omega_i \chi_{\text{eff}}^{(2)}}{n_i c} v_i E_p E_s^*. \end{aligned}$$

We set $E_i e^{-i\Delta k Z} = \hat{E}_i$ with $E_i^* e^{i\Delta k Z} = \hat{E}_i^*$ in order to isolate the phase mismatch in one equation

$$\frac{\partial E_s}{\partial Z} v_s + \frac{\partial E_s}{\partial t} = \frac{i\omega_s \chi_{\text{eff}}^{(2)}}{n_s c} v_s E_p \hat{E}_i^*, \quad (4.8)$$

$$\frac{\partial E_p}{\partial Z} v_p + \frac{\partial E_p}{\partial t} = \frac{i\omega_p \chi_{\text{eff}}^{(2)}}{n_p c} v_p E_s \hat{E}_i, \quad (4.9)$$

$$\frac{\partial (\hat{E}_i e^{i\Delta k Z})}{\partial Z} v_i e^{-i\Delta k Z} + \frac{\partial (\hat{E}_i e^{i\Delta k Z})}{\partial t} e^{-i\Delta k Z} = \frac{i\omega_i \chi_{\text{eff}}^{(2)}}{n_i c} v_i E_p E_s^*.$$

Solving the partial differential equation for \hat{E}_i gives

$$\left[\frac{\partial \hat{E}_i}{\partial Z} e^{i\Delta k Z} + i\Delta k \hat{E}_i e^{i\Delta k Z} \right] v_i e^{-i\Delta k Z} + \frac{\partial \left(\hat{E}_i e^{i\Delta k Z} \right)}{\partial t} e^{-i\Delta k Z} = \frac{i\omega_i \chi_{\text{eff}}^{(2)}}{n_i c} v_i E_p E_s^*,$$

$$\begin{aligned} \frac{\partial \hat{E}_i}{\partial Z} v_i + i\Delta k \hat{E}_i + \frac{\partial \hat{E}_i}{\partial t} &= \frac{i\omega_i \chi_{\text{eff}}^{(2)}}{n_i c} v_i E_p E_s^*, \\ \frac{\partial \hat{E}_i}{\partial Z} v_i + \frac{\partial \hat{E}_i}{\partial t} &= \frac{i\omega_i \chi_{\text{eff}}^{(2)}}{n_i c} v_i E_p E_s^* - i\Delta k v_i \hat{E}_i. \end{aligned} \quad (4.10)$$

The $i\Delta k v_i \hat{E}_i$ term represents the phase matching of the nonlinear interaction. Doing a transformation to a frame moving with the velocity of the signal wave (E_s) in the crystal, using $z = Z - v_s t$ and $\tau = t$, the signal wave equations becomes

$$\begin{aligned} \frac{\partial E_s}{\partial Z} v_s + \frac{\partial E_s}{\partial t} &= \frac{i\omega_s \chi_{\text{eff}}^{(2)}}{n_s c} v_s E_p \hat{E}_i^*, \\ v_s \left[\frac{\partial E_s}{\partial \tau} \frac{\partial \tau}{\partial z} + \frac{\partial E_s}{\partial z} \frac{\partial z}{\partial Z} \right] + \left[\frac{\partial E_s}{\partial \tau} \frac{\partial \tau}{\partial t} + \frac{\partial E_s}{\partial Z} \frac{\partial Z}{\partial t} \right] &= \frac{i\omega_s \chi_{\text{eff}}^{(2)}}{n_s c} v_s E_p \hat{E}_i^*, \\ v_s \left[\frac{\partial E_s}{\partial \tau} (0) + \frac{\partial E_s}{\partial z} (1) \right] + \left[\frac{\partial E_s}{\partial \tau} (1) + \frac{\partial E_s}{\partial z} (-v_s) \right] &= \frac{i\omega_s \chi_{\text{eff}}^{(2)}}{n_s c} v_s E_p \hat{E}_i^*. \end{aligned}$$

This is repeated for E_p and E_i so that the pulse interaction can be described as

$$\begin{aligned} \frac{\partial E_s}{\partial \tau} &= \frac{i\omega_s \chi_{\text{eff}}^{(2)}}{n_s c} v_s E_p \hat{E}_i^*, \\ \frac{\partial E_p}{\partial z} (v_p - v_s) + \frac{\partial E_p}{\partial \tau} &= \frac{i\omega_p \chi_{\text{eff}}^{(2)}}{n_p c} v_p E_s \hat{E}_i, \\ \frac{\partial \hat{E}_i}{\partial z} (v_i - v_s) + \frac{\partial \hat{E}_i}{\partial \tau} &= \frac{i\omega_i \chi_{\text{eff}}^{(2)}}{n_i c} v_i E_p E_s^* - i\Delta k v_i \hat{E}_i. \end{aligned} \quad (4.11)$$

The pulses are now moving in a frame relative to the signal pulse, so that the signal is stationary and the pump and idler pulse moves in relation to the signal pulse. Finally these equations are transferred to dimensionless units so that we have a universal treatment, independent of specific

pulse characteristics. Making the suitable transformations [27]

$$\begin{aligned}\frac{\Lambda}{E_0} \frac{\partial E_s}{\partial \tau} &= \frac{\Lambda}{E_0} \frac{i\omega_s \chi_{\text{eff}}^{(2)}}{n_s c} v_s E_p \hat{E}_i^*, \\ \frac{\Lambda}{E_0} \frac{\partial E_p}{\partial z} (v_p - v_s) + \frac{\Lambda}{E_0} \frac{\partial E_p}{\partial \tau} &= \frac{\Lambda}{E_0} \frac{i\omega_p \chi_{\text{eff}}^{(2)}}{n_p c} v_p E_s \hat{E}_i, \\ \frac{\Lambda}{E_0} \frac{\partial \hat{E}_i}{\partial z} (v_i - v_s) + \frac{\Lambda}{E_0} \frac{\partial \hat{E}_i}{\partial \tau} &= \frac{\Lambda}{E_0} \frac{i\omega_i \chi_{\text{eff}}^{(2)}}{n_i c} v_i E_p E_s^* - \frac{\Lambda}{E_0} i\Delta k v_i \hat{E}_i.\end{aligned}$$

Here $E'_j = \frac{E_j}{E_0}$ and $E'_i = \frac{\hat{E}_i}{E_0}$ is the dimensionless electric field strength weighted by the maximum amplitude (E_0), of a transform limited pump pulse. $z' = \frac{z}{\Lambda}$ is the dimensionless distance, in units of spatial pump pulse width Λ in the medium, time is expressed in units of the transform limited pulse duration $T = \frac{\Lambda}{c}$ as $t' = \frac{\tau}{T}$. By multiplying the equation with the characteristic constants $\frac{\Lambda}{E_0}$ we can now do a transformation to dimensionless units for the idler wave equation

$$\begin{aligned}\frac{\partial E'_i}{\partial z'} (v_i - v_s) + T c \frac{\partial E'_i}{\partial \tau} &= E_0 \Lambda \frac{i\omega_i \chi_{\text{eff}}^{(2)}}{n_i c} v_i E'_p E'_s{}^* - i\Delta k v_i \Lambda E'_i, \\ \frac{\partial E'_i}{\partial z'} (v_i - v_s) \frac{1}{c} + \frac{\partial E'_i}{\partial t'} &= E_0 \Lambda \frac{v_i}{c} \frac{i\omega_i \chi_{\text{eff}}^{(2)}}{n_i c} E'_p E'_s{}^* - \frac{1}{c} i\Delta k \frac{c}{n_i} \Lambda E'_i, \\ \frac{\partial E'_i}{\partial z'} \left(\frac{1}{n_i} - \frac{1}{n_s} \right) + \frac{\partial E'_i}{\partial t'} &= E_0 \Lambda \frac{i\omega_i \chi_{\text{eff}}^{(2)}}{n_i^2 c} E'_p E'_s{}^* - i\Delta k \frac{\Lambda}{n_i} E'_i.\end{aligned}$$

Repeating this for E_s and E_p the interaction of the dimensionless electric fields (E'_j) can be described as

$$\begin{aligned}\frac{\partial E'_s}{\partial t'} &= E_0 \Lambda \frac{i\omega_s \chi_{\text{eff}}^{(2)}}{n_s^2 c} E'_p E'_i{}^*, \\ \frac{\partial E'_p}{\partial z'} \left(\frac{1}{n_p} - \frac{1}{n_s} \right) + \frac{\partial E'_p}{\partial t'} &= E_0 \Lambda \frac{i\omega_p \chi_{\text{eff}}^{(2)}}{n_p^2 c} E'_s E'_i, \\ \frac{\partial E'_i}{\partial z'} \left(\frac{1}{n_i} - \frac{1}{n_s} \right) + \frac{\partial E'_i}{\partial t'} &= E_0 \Lambda \frac{i\omega_i \chi_{\text{eff}}^{(2)}}{n_i^2 c} E'_p E'_s{}^* - i\Delta k \frac{\Lambda}{n_i} E'_i.\end{aligned}\tag{4.12}$$

The relative velocities can now be defined as the inverse difference in refractive indices, $\nu_{ps} = \frac{1}{n_p} - \frac{1}{n_s}$ and $\nu_{is} = \frac{1}{n_i} - \frac{1}{n_s}$ and the dimensionless nonlinear coupling is $\gamma_j = \frac{\omega_j \chi_{\text{eff}}^{(2)} E_0 \Lambda}{n_j^2 c}$. So that we can write

$$\frac{\partial E'_s}{\partial t'} = i\gamma_s E'_p E'_i{}^*,\tag{4.13}$$

$$\frac{\partial E'_p}{\partial z'} + \frac{1}{\nu_{ps}} \frac{\partial E'_p}{\partial t'} = \frac{1}{\nu_{ps}} i\gamma_p E'_s E'_i,\tag{4.14}$$

$$\frac{\partial E'_i}{\partial z'} + \frac{1}{\nu_{is}} \frac{\partial E'_i}{\partial t'} = \frac{1}{\nu_{is}} i\gamma_i E'_p E'_s{}^* - \frac{1}{\nu_{is}} i\Delta k \frac{\Lambda}{n_i} E'_i. \quad (4.15)$$

Equations 4.13 to 4.15 corresponds to the nonlinear coupling equations used by Cavallari et al. [28] and Bakker et al. [27].

Expressing the equations in dimensionless units demonstrates that the only relevant parameters in the problem are the relative velocities ν_{ij} , and the effective nonlinear coupling constants γ_j . On its own, the left side of equation 4.13 to 4.15 leads to movement of the pulse in the nonlinear medium, while the right hand side results in the nonlinear interaction of the respective pulses when there is temporal and spatial overlap.

This derivation was done for the nonlinear interaction of the pulses in the time domain. For the corresponding frequency domain information a Fourier transform of each pulse (described by the electric field E) must be done.

4.2 Conservation of Energy During Difference Frequency Mixing

In this section we show that the equations describing the nonlinear interaction, derived from Maxwell's equations adheres to conservation of energy. To test that there is conservation of energy in the DFG process we show analytically that $\frac{\partial U}{\partial t} = 0$, where U is the energy density. Starting with equations 4.8, 4.9 and 4.10 and assuming perfect phase matching so that $\Delta k = 0$, we have

$$\begin{aligned} \frac{\partial E_s}{\partial z} + \frac{1}{v_s} \frac{\partial E_s}{\partial t} &= \frac{i\omega_s \chi_{\text{eff}}^{(2)}}{n_s c} E_p E_i^*, \\ \frac{\partial E_p}{\partial z} + \frac{1}{v_p} \frac{\partial E_p}{\partial t} &= \frac{i\omega_p \chi_{\text{eff}}^{(2)}}{n_p c} E_s E_i, \\ \frac{\partial E_i}{\partial z} + \frac{1}{v_i} \frac{\partial E_i}{\partial t} &= \frac{i\omega_i \chi_{\text{eff}}^{(2)}}{n_i c} E_p E_s^*. \end{aligned}$$

Setting $\gamma_k = \frac{\omega_k \chi_{\text{eff}}^{(2)}}{n_k c}$, with $n_k = \frac{c}{v_k}$ and multiplying each equation with E_k^* , with $k = s, p, i$ respectively, we can write

$$\begin{aligned}\frac{\partial E_s}{\partial z} E_s^* + \frac{1}{v_s} \frac{\partial E_s}{\partial t} E_s^* &= i\gamma_s E_p E_i^* E_s^*, \\ \frac{\partial E_p}{\partial z} E_p^* + \frac{1}{v_p} \frac{\partial E_p}{\partial t} E_p^* &= i\gamma_p E_s E_i E_p^*, \\ \frac{\partial E_i}{\partial z} E_i^* + \frac{1}{v_i} \frac{\partial E_i}{\partial t} E_i^* &= i\gamma_i E_p E_s^* E_i^*.\end{aligned}$$

Rewriting these equations we have

$$\begin{aligned}\frac{\partial E_s E_s^*}{\partial z} &= \frac{\partial E_s}{\partial z} E_s^* + \frac{\partial E_s^*}{\partial z} E_s, \\ \left(\frac{\partial E_s E_s^*}{\partial z}\right) + \frac{1}{v_s} \left(\frac{\partial E_s E_s^*}{\partial t}\right) &= i\gamma_s (E_p E_i^* E_s^* + \text{cc.}),\end{aligned}$$

$$\left[\frac{\partial}{\partial z} + \frac{1}{v_s} \frac{\partial}{\partial t}\right] |E_s|^2 = i\gamma_s (E_p E_i^* E_s^* - E_p^* E_i E_s), \quad (4.16)$$

$$\left[\frac{\partial}{\partial z} + \frac{1}{v_p} \frac{\partial}{\partial t}\right] |E_p|^2 = i\gamma_p (E_s E_i E_p^* - E_s^* E_i^* E_p), \quad (4.17)$$

$$\left[\frac{\partial}{\partial z} + \frac{1}{v_i} \frac{\partial}{\partial t}\right] |E_i|^2 = i\gamma_i (E_p E_s^* E_i^* - E_p^* E_s E_i). \quad (4.18)$$

Now in SI units, energy density (U) can be written as

$$U = \int dV \mathbf{E} \cdot \mathbf{D}$$

$$\mathbf{D} = \epsilon \mathbf{E}$$

$$\epsilon = \epsilon_0 (1 + \chi_e)$$

with χ_e the linear susceptibility. The refractive index can we expressed as

$$\begin{aligned}n &= \sqrt{\frac{\mu}{\mu_0} \frac{\epsilon}{\epsilon_0}}, \\ &= \sqrt{\frac{\mu}{\mu_0} (1 + \chi_e)},\end{aligned}$$

and assuming $\mu = \mu_0$,

$$\begin{aligned}\epsilon &= \epsilon_0(1 + \chi_e), \\ \epsilon &= \epsilon_0 n^2.\end{aligned}$$

The energy density can now be expressed as

$$U = \epsilon_0 n^2 \int dV |\mathbf{E}|^2.$$

The quantity $E_0 \int dV (n_s^2 |E_s|^2 + n_p^2 |E_p|^2 + n_i^2 |E_i|^2) = U$ should be conserved. Equation 4.16 to 4.18 can be re-written as

$$\begin{aligned}v_s \frac{\partial}{\partial z} |E_s|^2 + \frac{\partial}{\partial t} |E_s|^2 &= i v_s \gamma_s (E_p E_i^* E_s^* - E_p^* E_i E_s), \\ v_p \frac{\partial}{\partial z} |E_p|^2 + \frac{\partial}{\partial t} |E_p|^2 &= i v_p \gamma_p (E_s E_i E_p^* - E_s^* E_i^* E_p), \\ v_i \frac{\partial}{\partial z} |E_i|^2 + \frac{\partial}{\partial t} |E_i|^2 &= i v_i \gamma_i (E_p E_s^* E_i^* - E_p^* E_s E_i).\end{aligned}$$

Since $v_k \gamma_k = \frac{\omega_k \chi_{\text{eff}}^{(2)}}{n_k^2}$

$$\begin{aligned}\frac{\partial}{\partial z} (n_s^2 v_s |E_s|^2 + n_p^2 v_p |E_p|^2 + n_i^2 v_i |E_i|^2) + \frac{\partial}{\partial t} (n_s^2 |E_s|^2 + n_p^2 |E_p|^2 + n_i^2 |E_i|^2) = \\ i \omega_s \chi_{\text{eff}}^{(2)} (E_p E_i^* E_s^* - E_p^* E_i E_s) + i \omega_p \chi_{\text{eff}}^{(2)} (E_s E_i E_p^* - E_s^* E_i^* E_p) + i \omega_i \chi_{\text{eff}}^{(2)} (E_p E_s^* E_i^* - E_p^* E_s E_i).\end{aligned}\quad (4.19)$$

We note that the three brackets are the same and define $\alpha = E_p E_i^* E_s^* - E_p^* E_i E_s$. Equation 4.19 now becomes

$$\begin{aligned}\frac{\partial}{\partial z} (n_s c |E_s|^2 + n_p c |E_p|^2 + n_i c |E_i|^2) + \frac{\partial}{\partial t} (n_s^2 |E_s|^2 + n_p^2 |E_p|^2 + n_i^2 |E_i|^2) = \\ i \omega_s \chi_{\text{eff}}^{(2)} \alpha - i \omega_p \chi_{\text{eff}}^{(2)} \alpha + i \omega_i \chi_{\text{eff}}^{(2)} \alpha, \\ \frac{\partial}{\partial z} (n_s c |E_s|^2 + n_p c |E_p|^2 + n_i c |E_i|^2) + \frac{\partial}{\partial t} (n_s^2 |E_s|^2 + n_p^2 |E_p|^2 + n_i^2 |E_i|^2) =\end{aligned}$$

$$i(\omega_s - \omega_p + \omega_i) \chi_{\text{eff}}^{(2)} \alpha.$$

But $\omega_p = \omega_s + \omega_i$, so that

$$\begin{aligned} \frac{\partial}{\partial z} \left(n_s c |E_s|^2 + n_p c |E_p|^2 + n_i c |E_i|^2 \right) + \frac{\partial}{\partial t} \left(n_s^2 |E_s|^2 + n_p^2 |E_p|^2 + n_i^2 |E_i|^2 \right) &= 0, \\ \int_{-\infty}^{\infty} \left[\frac{\partial}{\partial z} \left(n_s c |E_s|^2 + n_p c |E_p|^2 + n_i c |E_i|^2 \right) + \frac{\partial}{\partial t} \left(n_s^2 |E_s|^2 + n_p^2 |E_p|^2 + n_i^2 |E_i|^2 \right) \right] dz &= 0, \\ \int_{-\infty}^{\infty} \frac{\partial}{\partial z} \left(n_s c |E_s|^2 + n_p c |E_p|^2 + n_i c |E_i|^2 \right) dz + \frac{\partial}{\partial t} \int_{-\infty}^{\infty} \left(n_s^2 |E_s|^2 + n_p^2 |E_p|^2 + n_i^2 |E_i|^2 \right) dz &= 0. \end{aligned}$$

E_j is 0 at $\omega_j = \pm\infty$ so that $\int_{-\infty}^{\infty} \frac{\partial}{\partial z} |E_j|^2 dz = 0$ since E_j is a Gaussian pulse and I_j is the total intensity for each pulse in the crystal, with $j = s, p, i$, so that we can write

$$\begin{aligned} \frac{\partial}{\partial t} \left(n_s^2 I_s + n_p^2 I_p + n_i^2 I_i \right) &= 0, \\ \frac{\partial U_T}{\partial t} &= 0. \end{aligned} \tag{4.20}$$

From equation 4.20 for the sum of the pulses the change in intensity, in time, is zero which proves that we have conservation of energy in our system.

4.2.1 Weak Coupling Limit

To build intuition and following closely the analysis of [37], we explore the limiting case in which the undepleted pump and signal approximation applies, which arises for weak coupling where γ_p and $\gamma_s \ll 1$. That is, we assume $\frac{\partial E_s}{\partial z} = 0$, $\frac{\partial E_s}{\partial t} = 0$ and $\frac{\partial E_p}{\partial z} = 0$, $\frac{\partial E_p}{\partial t} = 0$ in equation 4.13 to 4.15 and we assume perfect phase matching, $\Delta k = 0$, so that the only relevant dynamical equation is

$$\frac{\partial E_i(z, t)}{\partial z} + \frac{1}{\nu_{is}} \frac{\partial E_i(z, t)}{\partial t} = \frac{1}{\nu_{is}} i \gamma E_p(z + \nu_{ps} t) E_s^*(z, t).$$

In the above equation, the dynamics of E_p and E_s enter only through their relative velocities, with $\nu_{ps} = \frac{1}{n_p} - \frac{1}{n_s}$, $\nu_{is} = \frac{1}{n_i} - \frac{1}{n_s}$, $\gamma = \frac{\omega_i \chi_{\text{eff}}^{(2)}}{n_i^2}$ and $z + \nu_{ps} t$ the position of E_p at time t with respect to the position of pulse E_s in the crystal. If we apply the transformation $u = z + \nu_{is} t$ then we can write

$$\begin{aligned} \frac{\partial E_i}{\partial z}(1) + \frac{\partial E_i}{\partial t} \left(\frac{1}{\nu_{is}} \right) &= \frac{\partial E_i}{\partial z} \left(\frac{\partial z}{\partial u} \right) + \frac{\partial E_i}{\partial t} \left(\frac{\partial t}{\partial u} \right) \\ &= \frac{\partial E_i(z, t)}{\partial u} \end{aligned}$$

so that

$$\frac{\partial E_i(u - \nu_{is}t)}{\partial u} = \frac{i\gamma}{\nu_{is}} E_s^*(u - \nu_{is}t) E_p(u - \nu_{is}t + \nu_{ps}t).$$

Now integrating over the length L of the nonlinear medium we have

$$\begin{aligned} \int_{-\nu_{is}t}^{L - \nu_{is}t} \frac{\partial E_i(u - \nu_{is}t)}{\partial u} du &= \frac{i\gamma}{\nu_{is}} \int_{-\nu_{is}t}^{L - \nu_{is}t} E_s^*(u - \nu_{is}t) E_p(u - \nu_{is}t + \nu_{ps}t) du, \\ E_i(L - \nu_{is}t) &= \frac{i\gamma}{\nu_{is}} \int_{-\nu_{is}t}^{L - \nu_{is}t} E_s^*(u - \nu_{is}t) E_p(u - \nu_{is}t + \nu_{ps}t) du. \end{aligned}$$

Assuming the nonlinear medium is long enough so that the temporal overlap occurs entirely in the crystal, allows us to extend the integration boundaries to infinity. We transform back to z so that

$$E_i(L - \nu_{is}t) = \frac{i\gamma}{\nu_{is}} \int_{-\infty}^{\infty} E_s^*(z) E_p(z + \nu_{ps}t) dz. \quad (4.21)$$

The above equation is in the form of a correlation, and indicates that perfect shape transfer will occur when the electric field of one of the pulses is a dirac delta function [29]. Experimentally, this means that if the pump pulse is shaped in time, the signal pulse has to be significantly shorter than the shortest feature (in time) of the pump pulse, for the shape to be transferred with high fidelity to E_i .

We can investigate the nonlinear interaction further analytically, by looking at equation 4.21 in the frequency domain. This is done by taking the Fourier transform of the convolution in equation 4.21 [37]

$$\begin{aligned} \int_{-\infty}^{\infty} E_i(L - \nu_{is}t) e^{-i\omega t} dt &= \frac{i\gamma}{\nu_{is}} \int_{-\infty}^{\infty} e^{-i\omega t} \left[\int_{-\infty}^{\infty} E_s^*(z) E_p(z + \nu_{ps}t) dz \right] dt, \\ \frac{1}{\nu_{is}} \int_{-\infty}^{\infty} E_i(L - \nu_{is}t) e^{-i\frac{\omega}{\nu_{is}} \nu_{is}t} \nu_{is} dt &= \frac{i\gamma}{\nu_{ps}\nu_{is}} \int_{-\infty}^{\infty} e^{-i\frac{\omega}{\nu_{ps}} \nu_{ps}t} \left[\int_{-\infty}^{\infty} E_s^*(z) E_p(z + \nu_{ps}t) \nu_{ps} dz \right] dt. \end{aligned}$$

If we set $L - \nu_{is}t = x'$ and $z + \nu_{ps}t = x''$ we can write

$$\begin{aligned}
 \frac{1}{\nu_{is}} \int_{-\infty}^{\infty} E_i(x') e^{-i\frac{\omega}{\nu_{is}}(L-x')} dx' &= \frac{i\gamma}{\nu_{ps}\nu_{is}} \int_{-\infty}^{\infty} e^{-i\frac{\omega}{\nu_{ps}}(x''-z)} \left[\int_{-\infty}^{\infty} E_s^*(z) E_p(x'') dz \right] dx'', \\
 \frac{\nu_{is}\nu_{ps}}{i\gamma\nu_{is}} \int_{-\infty}^{\infty} E_i(x') e^{-i\frac{\omega}{\nu_{is}}L} e^{i\frac{\omega}{\nu_{is}}x'} dx' &= \int_{-\infty}^{\infty} e^{-i\frac{\omega}{\nu_{ps}}x''} e^{i\frac{\omega}{\nu_{ps}}z} \int_{-\infty}^{\infty} E_s^*(z) E_p(x'') dz dx'', \\
 \frac{\nu_{ps}}{i\gamma} e^{-i\frac{\omega}{\nu_{is}}L} \int_{-\infty}^{\infty} E_i(x') e^{i\frac{\omega}{\nu_{is}}x'} dx' &= \int_{-\infty}^{\infty} e^{-i\frac{\omega}{\nu_{ps}}x''} E_p(x'') dx'' \int_{-\infty}^{\infty} E_s^*(z) e^{i\frac{\omega}{\nu_{ps}}z} dz, \\
 \frac{\nu_{ps}}{i\gamma} e^{-i\frac{\omega}{\nu_{is}}L} E_i^* \left(\frac{\omega}{\nu_{is}} \right) &= E_p \left(\frac{\omega}{\nu_{ps}} \right) \cdot E_s^* \left(\frac{\omega}{\nu_{ps}} \right). \tag{4.22}
 \end{aligned}$$

$E_i^* \left(\frac{\omega}{\nu_{is}} \right)$ and $E_s^* \left(\frac{\omega}{\nu_{ps}} \right)$ is the inverse Fourier transform of $E_i(x')$ and $E_s(z)$ respectively and $E_p \left(\frac{\omega}{\nu_{ps}} \right)$ is the Fourier transform of $E_p(x'')$. Equation 4.22 indicates that while the dirac delta function solution in equation 4.21 is one possible solution, as discussed above, it is not unique. Instead many solutions for generating a specific pulse shape are possible, particularly if both the signal and pump pulses can be shaped independently.

To investigate the influence of the different widths and amplitudes of the interacting pulses, we solve equation 4.21 with A and B the amplitude of the pump and signal respectively and τ_p and τ_s the FWHM for the specific case of Gaussian pulses.

$$\begin{aligned}
 E_i(L - \nu_{is}t) &= \frac{i\gamma}{\nu_{is}} \int_{-\infty}^{\infty} E_p(z + \nu_{ps}t) E_s(z) dz, \\
 &= \frac{i\gamma}{\nu_{is}} \int_{-\infty}^{\infty} \left(A e^{-\frac{(z+\nu_{ps}t)^2}{\sqrt{2}\tau_p^2}} \right) \left(B e^{-\frac{z^2}{\sqrt{2}\tau_s^2}} \right) dz, \\
 &= \frac{i\gamma}{\nu_{is}} AB 2^{1/4} \sqrt{\pi} \frac{1}{\sqrt{\frac{1}{\tau_p^2} + \frac{1}{\tau_s^2}}} e^{-\frac{(\nu_{ps}t)^2}{\sqrt{2}(\tau_p^2 + \tau_s^2)}}.
 \end{aligned}$$

If $R = L - \nu_{is}t$, $t = \frac{L-R}{\nu_{is}}$, with R the position of the idler pulse in the crystal at time t

$$E_i(R) = \frac{i\gamma}{\nu_{is}} 2^{1/4} \sqrt{\pi} AB \frac{1}{\sqrt{\frac{1}{\tau_p^2} + \frac{1}{\tau_s^2}}} e^{-\frac{\left(\frac{\nu_{ps}}{\nu_{is}}\right)^2 (L-R)^2}{\sqrt{2}(\tau_p^2 + \tau_s^2)}}. \tag{4.23}$$

Equation 4.23 indicates that the amplitude of the generated pulse is directly dependent on the amplitudes of the input pulses (AB) as well as the FWHM of each input pulse, $\frac{1}{\sqrt{\frac{1}{\tau_p^2} + \frac{1}{\tau_s^2}}}$. The width of the generated pulse is dependent on the ratio of the relative velocities, $r_v = \frac{\nu_{is}}{\nu_{ps}}$, as well as the widths of the input pulses, $\tau_p^2 + \tau_s^2$. As a result, careful selection of the relative velocities can be used to tune the width of the output pulse, as we will explore later in this chapter.

4.3 Numerical Modeling

We now want to do a computational simulation of the theory using equations 4.13 to 4.15 from the previous section. In order to do this we employ numerical methods, such as the Lax-Friedrichs which is used to solve partial differential equations based on a finite difference method.

To implement the Lax-Friedrichs in our simulations we must first investigate how the method works. Consider the following first order partial differential equation for an arbitrary field u , which depends on both time (t) and position (x)

$$\frac{\partial u}{\partial x} a + \frac{\partial u}{\partial t} = 0. \quad (4.24)$$

The two terms in equation 4.24 can be discretised as follows

$$\begin{aligned} \frac{\partial u}{\partial x} a &= a \frac{u_{i+1}^j - u_{i-1}^j}{2\Delta x} \text{ and} \\ \frac{\partial u}{\partial t} &= \frac{u_i^{j+1} - u_i^j}{\Delta t}, \\ &= \frac{u_i^{j+1}}{\Delta t} - \frac{1}{2} \left(\frac{u_{i+1}^j + u_{i-1}^j}{\Delta t} \right), \end{aligned}$$

with i and j representing the steps in space and time respectively. Combining the above terms, we can now solve for the new value of the field at time $j+1$

$$\begin{aligned} a \frac{\partial u}{\partial x} + \frac{\partial u}{\partial t} &= 0, \\ a \frac{u_{i+1}^j - u_{i-1}^j}{2\Delta x} + \frac{u_i^{j+1}}{\Delta t} - \frac{1}{2} \left(\frac{u_{i+1}^j + u_{i-1}^j}{\Delta t} \right) &= 0, \end{aligned}$$

$$u_i^{j+1} = \frac{1}{2} (u_{i+1}^j + u_{i-1}^j) - \frac{a\Delta t}{2\Delta x} (u_{i+1}^j - u_{i-1}^j).$$

with Δx a step in position and Δt a step in time, see figure 4.1.

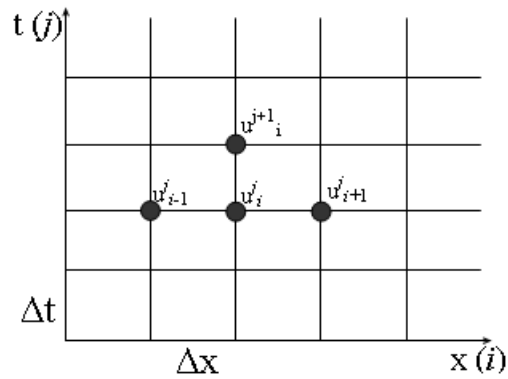


Figure 4.1: Visualisation of the Lax-Friedrichs method.

It is important to note that the Lax-Friedrichs method is numerically stable when the Courant-Friedrichs-Lewy condition is met

$$a \left| \frac{\Delta t}{\Delta x} \right| \leq 1. \quad (4.25)$$

To further study the dynamics we resort to a finite difference split-step method to numerically solve equations 4.13 to 4.15. In this approach one alternates between propagating the motional part (the left-handed-side of equations 4.13 to 4.15), and the nonlinear part (the right-handed-side) of the set of equations. Consider first only the motional part of equation 4.13 to 4.15, which we solve using finite-differencing according to the Lax Frederick method

$$\begin{aligned} \frac{\partial E'_s}{\partial t'} &= 0, \\ \frac{\partial E'_p}{\partial z'} + \frac{1}{v_{ps}} \frac{\partial E'_p}{\partial t'} &= 0, \\ \frac{\partial E'_i}{\partial z'} + \frac{1}{v_{is}} \frac{\partial E'_i}{\partial t'} &= 0. \end{aligned}$$

The relative movement of the pulses in the crystal are shown at 3 different times; at $t=0$, halfway through the interaction when the pump and signal fully overlap, and when the pump and signal have completely moved over each other, see figure 4.2.

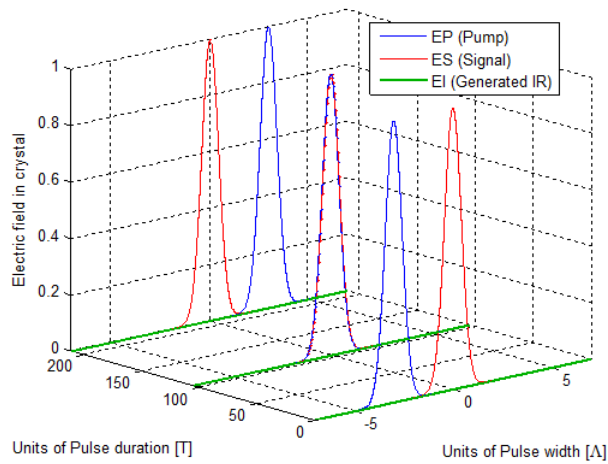


Figure 4.2: Relative movement of the pulses using the Lax-Friedrichs method.

It can clearly be seen in figure 4.2 how the pump field is moving (left to right), with time, over the stationary signal field. The relative velocities are dependent on the refractive indices which are calculated using the Sellmeier equations for the relevant crystal. From figure 4.2, it is clear that there are no change in the pump and signal pulse intensities or the shape of the envelopes when only the pulse movement are considered.

For the nonlinear interaction (right hand side of equation 4.12) in the second step of the split-step method we consider only the time evolution of the nonlinear interaction

$$\frac{\partial E'_s}{\partial t'} = i\gamma_s E'_p E_i'^*, \quad (4.26)$$

$$\frac{1}{v_{ps}} \frac{\partial E'_p}{\partial t'} = \frac{1}{v_{ps}} i\gamma_p E'_s E_i', \quad (4.27)$$

$$\frac{1}{v_{is}} \frac{\partial E'_i}{\partial t'} = \frac{1}{v_{is}} i\gamma_i E'_p E_s'^* - \frac{1}{v_{is}} i\Delta k \frac{\Lambda}{n_i} \tilde{E}'_i, \quad (4.28)$$

with $\gamma_j = \frac{\omega_j \chi_{\text{eff}}^{(2)} E_0 \Lambda}{n_j^2 c}$. The equations are discretised using a simple Euler method

$$\begin{aligned} \frac{E'_s(i, j+1) - E'_s(i, j)}{\Delta t'} &= i\gamma_s E'_p(i, j) E_i'^*(i, j), \\ E'_s(i, j+1) &= E'_s(i, j) + \Delta t' i\gamma_s E'_p(i, j) E_i'^*(i, j), \\ E'_p(i, j+1) &= E'_p(i, j) + \Delta t' i\gamma_p E'_s(i, j) E_i'(i, j), \end{aligned}$$

$$E'_i(i, j + 1) = E'_i(i, j) + \Delta t' i \gamma_i E'_p(i, j) E_s^{*'}(i, j) - \Delta t' i \Delta k \frac{\Lambda}{n_i} \tilde{E}'_i.$$

To illustrate the effect of the nonlinearity alone, we neglect the relative movement of the two pulses. E'_i is generated by mixing E'_s and E'_p in the non linear medium (figure 4.3).

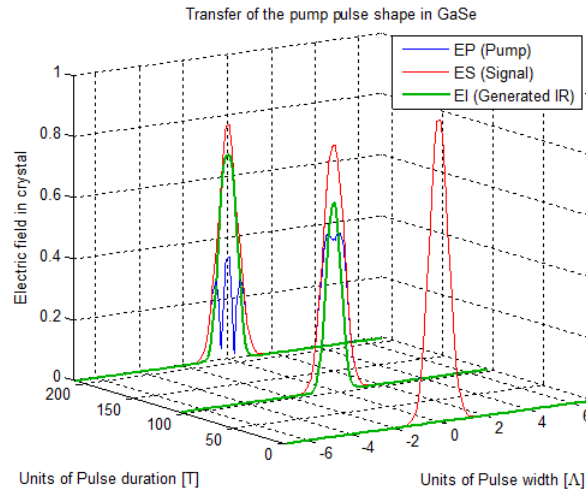


Figure 4.3: Difference frequency generation simulated using the Euler method.

The depletion of the signal (E_s) and pump pulse (E_p), due to the generation of the idler (E_i) is clear and can be seen in figure 4.3 after about 100 pulse durations. As the interaction time becomes longer, back conversion to the signal or pump beam will start to occur as is evident at 200 pulse durations. Finally the split step method is used to combine the two separately solved parts of the pump, signal and idler. First the the movement is addressed using the Lax-Friedrichs (linear part) and next the nonlinear interaction is addressed using the Euler, with the electric fields generated by the Lax-Friedrichs functioning as the input. In figure 4.4 the relative movement of the pulses combined with the generation of the idler, are shown clearly.

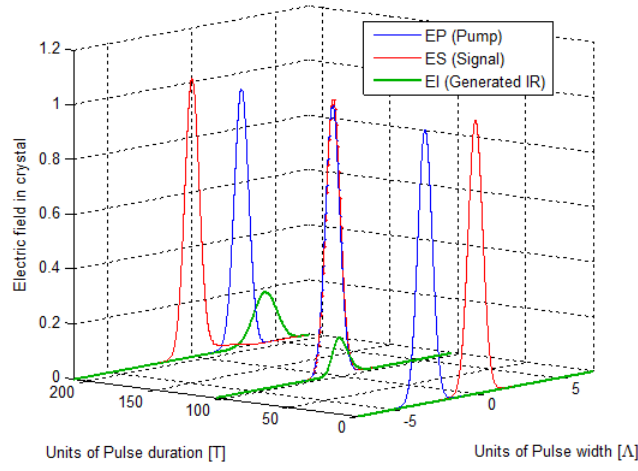


Figure 4.4: Difference frequency generation simulated using the combined Lax-Friedrichs and the Euler method in a single pulse.

For the input signal (E_s) and pump beam (E_p), the amplitude of the generated infrared pulse (E_i) in figure 4.4 is 0.185.

4.4 Parametric Study

To better understand the effect of each parameter on the nonlinear interaction between the pulses, we investigate the effect of the nonlinear coupling strengths (γ_j), as well as the relative velocities of the three interacting pulses on the efficiency of the pulse shape transfer to the idler pulse. The relative velocity of the pump and idler have previously been defined as $v_{js} = \frac{1}{n_j} - \frac{1}{n_s}$ and the velocity ratio as $r_v = \frac{v_{is}}{v_{ps}}$. For this study we calculate the nonlinear coupling strengths of the pump (γ_p) and idler (γ_i) pulse in relation to the coupling strength of the signal pulse (γ_s), by using equation 4.26, 4.27 and 4.28, while assuming perfect phase matching ($\Delta k = 0$). The nonlinear interaction factor for the pump and idler pulses can be written in terms of the signal so that

$$\begin{aligned}
 \gamma_s &= \frac{\omega_s}{n_s^2} \frac{\chi_{\text{eff}}^{(2)} E_0 \Lambda}{c}, \\
 \gamma_p &= \frac{\omega_p}{n_p^2} \frac{\chi_{\text{eff}}^{(2)} E_0 \Lambda}{c}, \\
 &= \frac{\chi_{\text{eff}}^{(2)} E_0 \Lambda}{c} \frac{\omega_s}{\omega_s} \frac{n_s^2}{n_s^2} \frac{\omega_p}{n_p^2},
 \end{aligned} \tag{4.29}$$

$$= \gamma_s \frac{\omega_p}{\omega_s} \frac{n_s^2}{n_p^2}. \quad (4.30)$$

Similarly for γ_i

$$\gamma_i = \gamma_s \frac{\omega_i}{\omega_s} \frac{n_s^2}{n_i^2}. \quad (4.31)$$

By using equation 4.29 to 4.31 it is now possible to tune the relevant parameters while preserving energy conservation. The factors considered in this study are the refractive index of each pulse n_s , n_p and n_i , as well as the frequencies ω_s , ω_p and ω_i , where $\omega_p = \omega_s + \omega_i$. We work in the undepleted pump regime and assume that we have perfect phase matching.

4.4.1 Influence of Nonlinear Coupling Strengths

First we investigate the influence of the nonlinear interaction factors on the pulses by tuning γ_s , γ_p and γ_i . This is done by changing the respective refractive indices and frequencies of the interacting pulses, while keeping $r_v = 1$, by setting $n_p = n_i$. In figure 4.5(a) we investigate the behavior of the pulses where all the nonlinear interaction factors are close to equal. The idler pulse has low intensity due to the low coupling constant (γ_i).

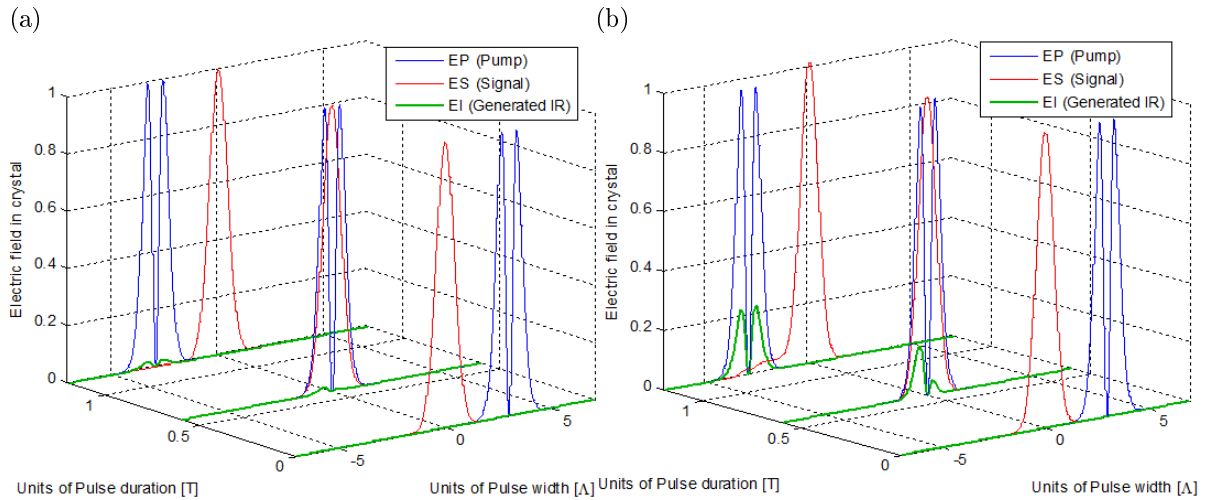


Figure 4.5: Shape transfer to the idler with (a) $\gamma_s \approx \gamma_p \approx \gamma_i \approx 0.1$ and (b) $\gamma_s \approx \gamma_p \approx \gamma_i \approx 1$.

In figure 4.5(b) the same refractive indices and frequencies are used but with $\gamma_s = 1$ so that $\gamma_p = 1.28$ and $\gamma_i = 1.03$. For this case where the nonlinear interaction factors are larger than the factors in figure 4.5(a), the idler pulse is larger compared to the idler pulse in figure 4.5(a), as expected, with back

conversion to the signal pulse. Back conversion occurs when the interaction between the pulses are very strong and the generated wavelength interacts with one of the input wavelengths to generate the second input wavelength as shown in figure 4.5(b).

In order to characterise the shape transfer fidelity (which is the accuracy of the transfer of the pulse shape from the shaped pulse to the generated pulse), we define a transfer error (equation 4.32) that is calculated by taking the root-mean-square difference of the normalised input shaped pump pulse and the normalised generated idler pulse, weighed against the area under the normalised input pump intensity

$$\text{Error in amplitude transfer} = \sqrt{\frac{\sum_i \left(\left| \frac{P_n}{P_{\max}} \right| - \left| \frac{I_n}{I_{\max}} \right| \right)^2}{\sum_i \left| \frac{P_n}{P_{\max}} \right|^2}}. \quad (4.32)$$

In figure 4.5(a) the error in the conversion fidelity is 0.03% and 1.6% in figure (b). In the case where the interaction factor is strong ($\gamma = 1$), the shape transfer has a larger error than in the case where $\gamma = 0.1$. This is due to back conversion to the signal, caused by the stronger interaction factors. We define an error less than 1% as excellent shape transfer and below 5% as good shape transfer.

The input values for the coupling strength study, as well as the error in the transfer efficiencies are summarised in table 4.1.

| Figure | Nonlinear coupling | γ_s | γ_p | γ_i | Error |
|--------|--|------------|------------|------------|-------|
| 4.5(a) | $\gamma_s \approx \gamma_p \approx \gamma_i$ | 0.1 | 0.128 | 0.103 | 0.03% |
| 4.6(a) | $\gamma_p \gg \gamma_s \approx \gamma_i$ | 0.1 | 2.6 | 0.1 | 0.03% |
| 4.6(b) | $\gamma_s \gg \gamma_p \approx \gamma_i$ | 5 | 1.375 | 0.125 | 1% |
| 4.7(a) | $\gamma_s \ll \gamma_p \approx \gamma_i$ | 0.1 | 2.4 | 2 | 0.5% |
| 4.7(b) | $\gamma_s \approx \gamma_p \gg \gamma_i$ | 0.1 | 0.103 | 0.0207 | 0.1% |

Table 4.1: Parameters for coupling strength study.

In figure 4.6(a) the pump pulse interaction strength is significantly larger than that of the signal and idler pulses, $\gamma_p \gg \gamma_s = \gamma_i$. The amplitude of the generated idler pulse is small due to the small value of $\gamma_i = 0.1$, with a shape transfer error of 0.03%. In the case of figure 4.6(b) where the signal pulse interaction strength, $\gamma_s = 5$, is much larger than that of the pump and idler pulse, there is back conversion to the signal which distorts the shape of the idler slightly, giving a error of 1%.

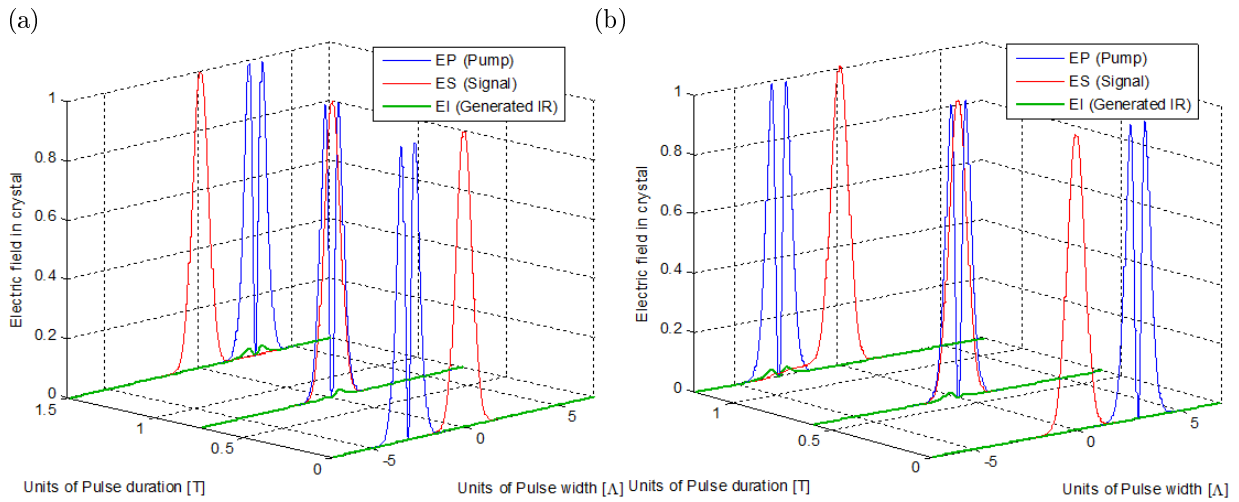


Figure 4.6: Shape and amplitude transfer to the idler with (a) $\gamma_p \gg \gamma_s = \gamma_i$ and (b) $\gamma_s \gg \gamma_p = \gamma_i$.

The input values for figure 4.6(a) and (b) are indicated in table 4.1 row 2 and 3, respectively.

In figure 4.7(a) the interaction strength of the idler (γ_i) and pump (γ_p) pulse are very large in comparison to that of the signal pulse. Due to the large γ_i the generated idler pulse has a very high intensity and shows strong depletion in the pump pulse at $T \approx 2.4$, with the error in the transfer fidelity 0.5%.

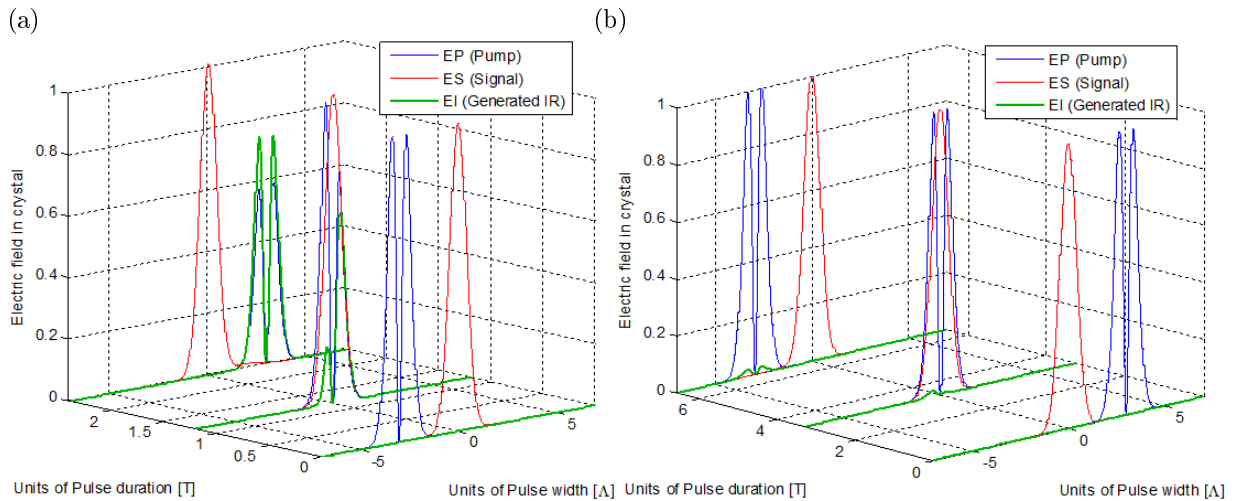


Figure 4.7: Shape and amplitude transfer to the idler with (a) $\gamma_s \ll \gamma_p = \gamma_i$ and (b) $\gamma_i \ll \gamma_s = \gamma_p$.

In figure 4.7(b) with $\gamma_i \ll \gamma_s = \gamma_p$, the generated idler amplitude is small, as expected since γ_i is small at 0.0207. The shape transfer error is calculated as 0.1%.

The largest errors in the transfer fidelity has been 1.6% in figure 4.5(b) and 1% in figure 4.6(b). In

both cases the larger error is due to back conversion to the signal pulse caused by a large γ_s factor. By keeping the signal pulse interaction strength or the amplitude of the input signal pulse sufficiently small, effectively eliminating the back conversion to the signal, the error in the transfer efficiencies can be vastly reduced. We conclude that, in the absence of back conversion, the coupling strengths does not have a strong effect on the shape transfer fidelity of the idler pulse, and efficient transfer can be achieved when using large γ_i .

4.4.2 Influence of Relative Velocities on Shape Transfer

It is clear from equation 4.23 that the fidelity of the pump pulse shape transfer to the idler pulse is connected to the relative velocities of the three pulses. To investigate the influence of these relative velocities on the shape transfer and the width of the idler pulse, we vary the relative velocities of the pump and idler pulse, $r_v = \frac{v_{is}}{v_{ps}} = \left(\frac{1}{n_i} - \frac{1}{n_s} \right) \left(\frac{1}{\frac{1}{n_p} - \frac{1}{n_s}} \right) = \left(\frac{n_s - n_i}{n_i} \right) \left(\frac{n_p}{n_s - n_p} \right)$. The frequencies ω_s , ω_p and ω_i were chosen to have a ratio: 4:5:1, and kept constant.

In figure 4.8(a), with $r_v = 2.5$, the shape of the idler pulse is broader than the input shape, with the error equal to 79%. In figure (b), where $r_v = 1.18$, the shape transfer is significantly better than in figure (a), with the error 24.6%.

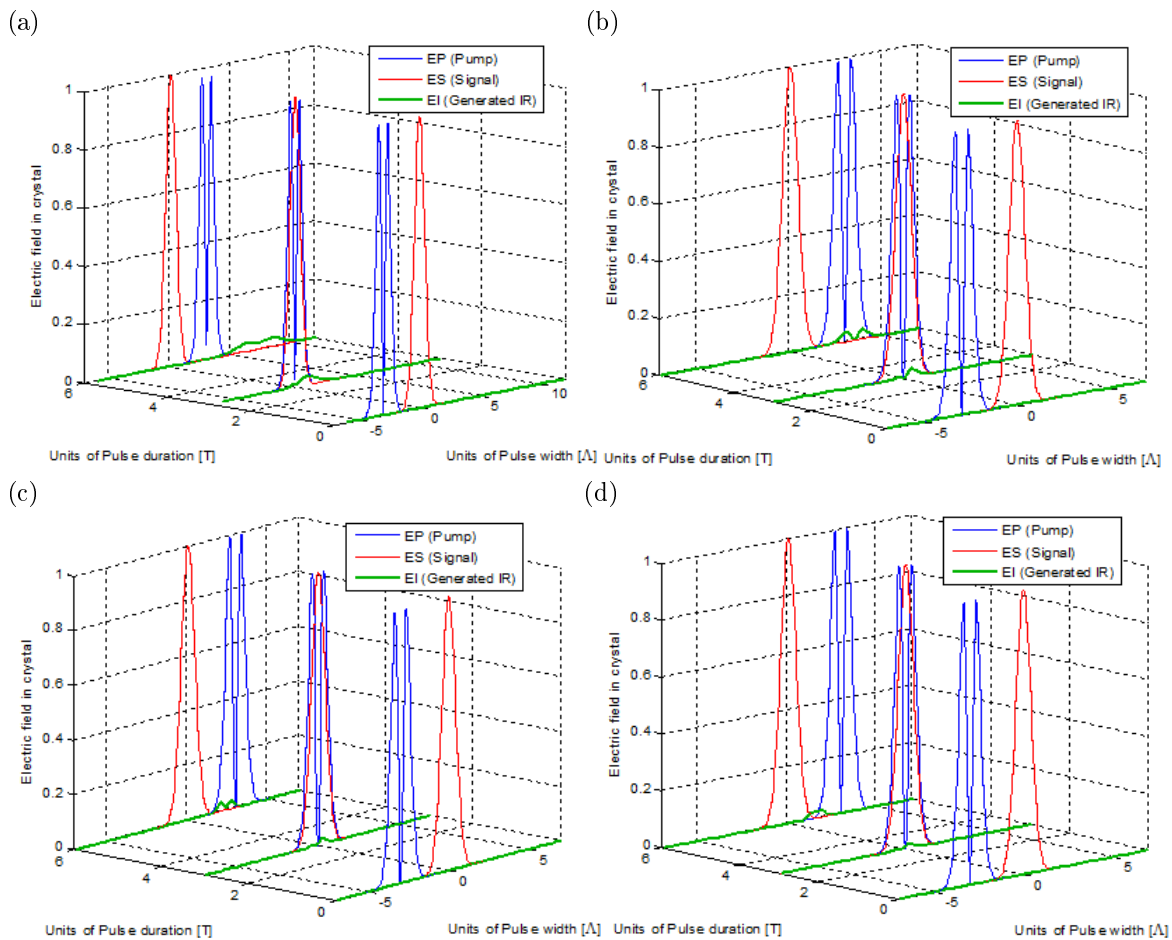


Figure 4.8: Transfer of the pump pulse shape to the idler pulse for (a) $r_v = 2.5$, (b) $r_v = 1.18$, (c) $r_v = 0.8$ and (d) $r_v = 0.56$.

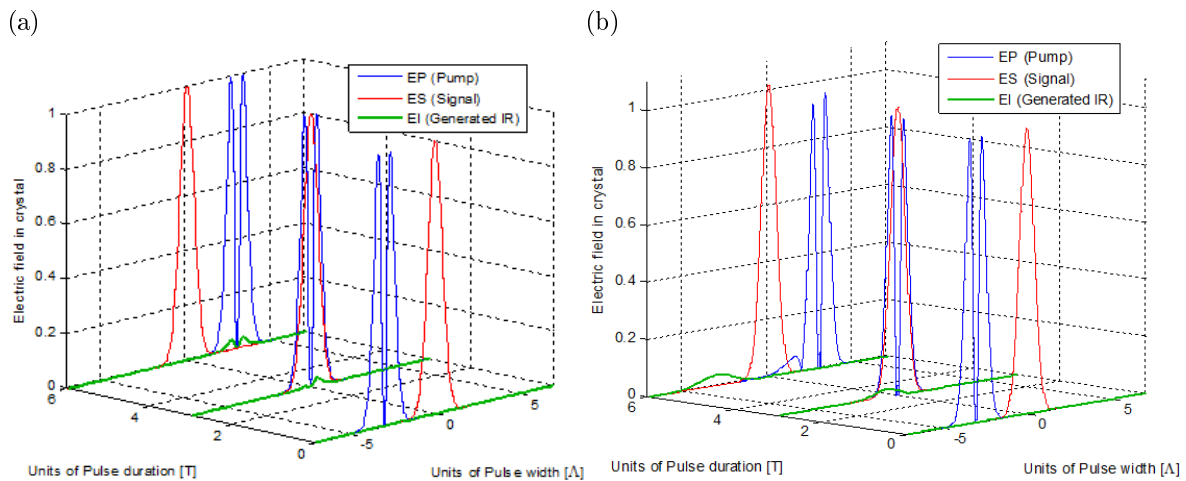
In figure 4.8(c), with $r_v = 0.8$ the transfer error is 27.5%, which is still better than figure (a), but with the idler pulse shape visibly narrower than the input shaped pulse. In figure 4.8(d) the error in the pulse shape transfer fidelity is 66.7%, with $r_v = 0.56$. The shape transfer error is smaller in figure (b) and (c) where r_v is closer to 1, see table 4.2 for a summary of all calculated relative velocities with corresponding simulated transfer errors.

| r_v | Error |
|-------|-------|
| 2.5 | 79% |
| 1.82 | 68.9% |
| 1.18 | 24.6% |
| 1 | 0.05% |
| 0.8 | 27.5% |
| 0.65 | 52.9% |
| 0.56 | 66.7% |

Table 4.2: Shape transfer to idler.

As demonstrated in table 4.2 the shape transfer occurs with negligible error when the velocity ratio r_v approximates 1. There is little to no shape transfer when r_v is larger than 2.5 or smaller than 0.56.

In figure 4.9(a) and (b) we consider the case where the pump and idler pulses move in opposite directions and compare 2 cases where r_v has opposite signs.


 Figure 4.9: Transfer of the pump pulse shape to the idler pulse for (a) $r_v = 1$ and (b) $r_v = -1$.

In figure 4.9(a) the error is 0.05% with $r_v = 1$, giving us optimal shape transfer. This corroborates the previous statement, that the shape transfer fidelity becomes better as r_v approaches 1. In figure 4.9(b) there is no shape transfer and the idler has a FWHM of 2.3 pulse widths. We conclude that there is no shape transfer to the idler pulse in the case where the pump and idler pulse move in opposite directions.

In conclusion the transfer fidelity is best when the generated pulse travels at the same velocity as the shaped pulse. As the difference in velocity between the two pulses becomes larger the fidelity of the shape transfer will become worse until there is no shape transfer.

4.4.3 Influence of Relative Velocities on a Pulse FWHM

In the previous subsection we observed in figures 4.8(a) and 4.8(d) that there was broadening and narrowing of the idler pulse shape, relative to the input pulses for specific value of r_v . This is expected from equation 4.23. In this subsection we investigate this behavior using single pulses, by comparing the FWHM of the idler to that of the input pump pulse while varying r_v . The frequencies ω_s , ω_p and ω_i were chosen to have a ratio: 4:5:1, and kept constant. Firstly, in figure 4.10, we investigate an extreme case where $r_v = -10$.

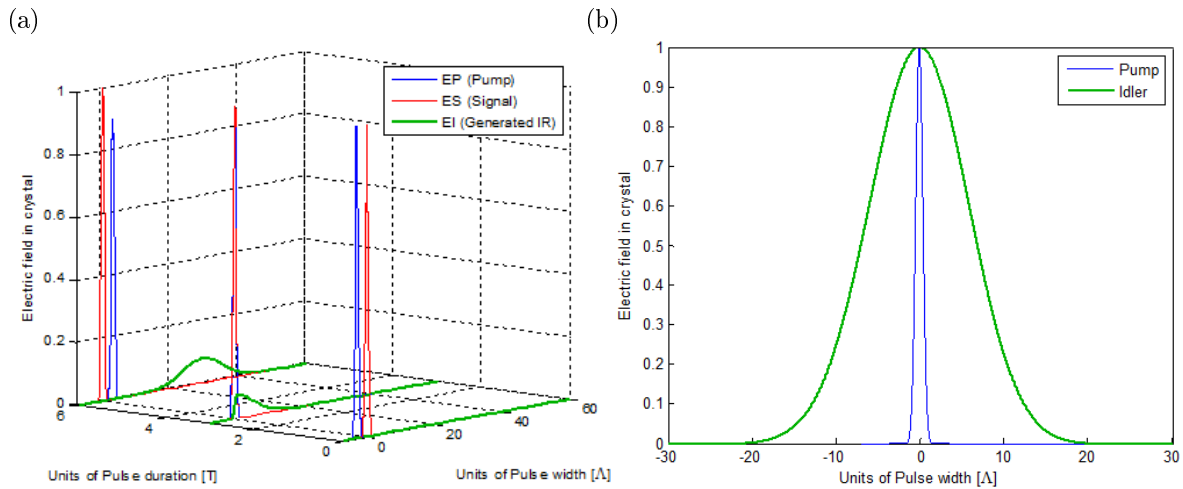


Figure 4.10: Generated single idler pulse for $r_v = 10$, (a) 3d view and (b) comparison between pump and idler pulse.

In figure 4.10(a) we see the evolution of the pulses, with the input pulses show at $T = 0$, half way through the interaction at $T = 3$ and the final result of the interaction at the final time at $T = 6$. There is extreme broadening of the idler pulse with the FWHM equal to 13.87 times the pulse width of the signal and pump input pulses. In figure 4.10(b) the idler pulse is normalised in intensity with respect to the input pump pulse and directly compared by plotting the two pulses on the same graph. Here the broadening of the idler pulse is illustrated very clearly. In the following figure (figure 4.11) the direct comparison is shown for different velocity ratios (r_v).

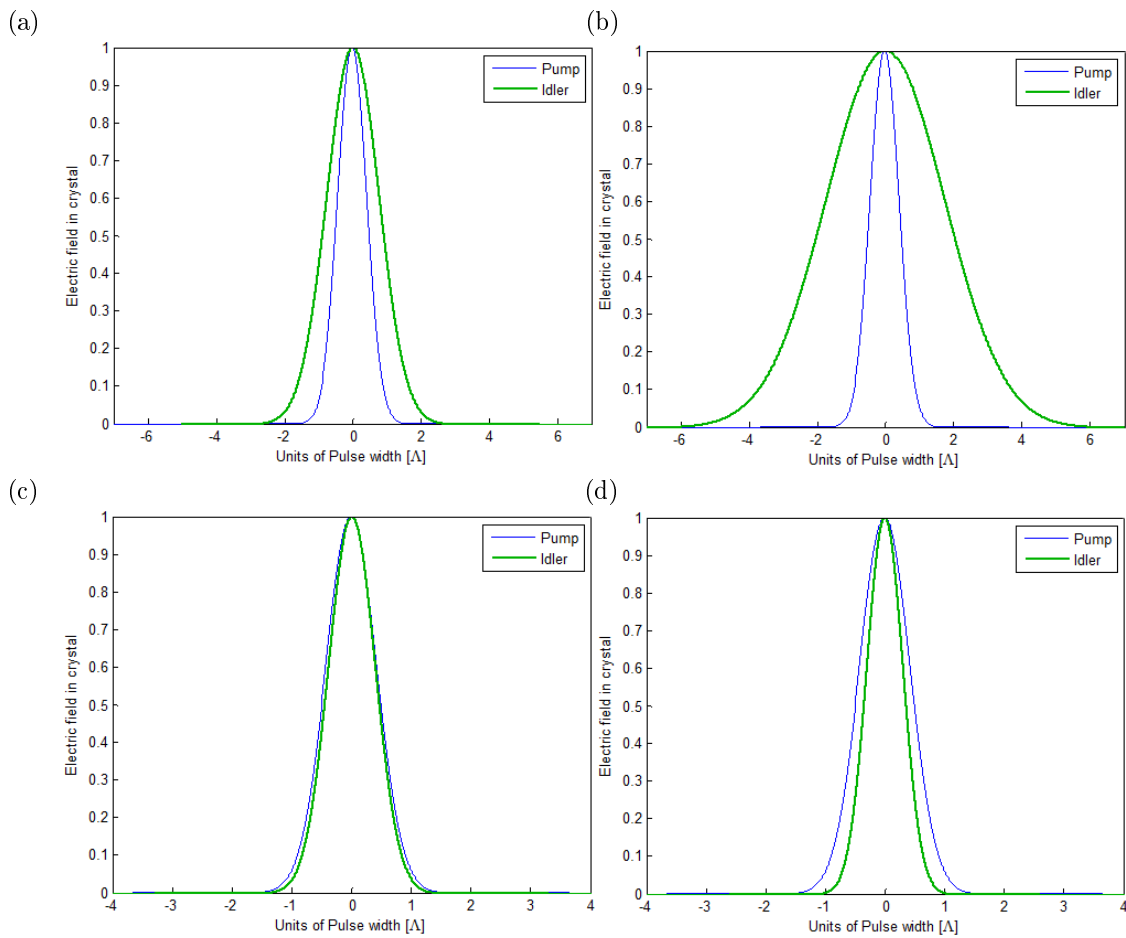


Figure 4.11: Generated single idler pulse for (a) $r_v = -0.67$, (b) $r_v = 3.33$, (c) $r_v = 0.91$ and (d) $r_v = 0.50$.

The relative velocity ratios of the pulses in figure 4.11 (a) to (d) is -0.67 , 3.33 , 0.91 and 0.50 respectively with each corresponding FWHM indicated in figure 4.12. On the graph in figure 4.12 we look at the general trend of the FWHM of the idler pulse for different relative velocity ratios (r_v), with the FWHM of the input pulses 1.

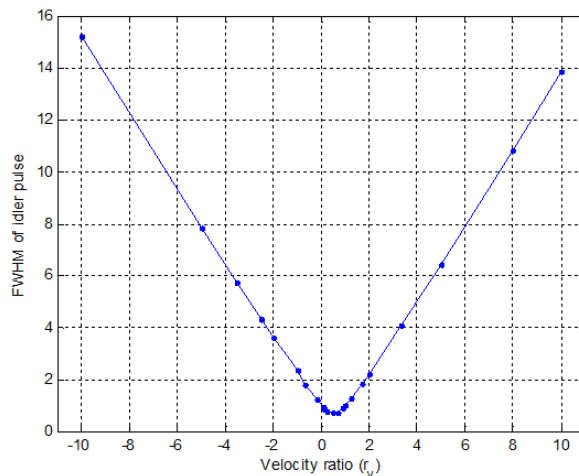


Figure 4.12: Idler FWHM for different velocity ratios (r_v).

At $r_v = 0$ and $r_v = 1$ the idler pulse is the same width as the input pulse, see figure 4.12. When $r_v = 1$, the idler moves at the same velocity as the shaped pulse, giving the good shape transfer that we simulated previously in figure 4.9(a). When r_v is between 0 and 1 the idler is narrower than the pump with maximum narrowing occurring when $r_v = 0.5$. When r_v is smaller than 0 or larger than 1 the idler becomes broadened. From figure 4.12 we can see that the idler will be wider as $|r_v|$ becomes larger. This numerical study agree with the analytical prediction from equation 4.23, and completes it in the area between $r_v = -1$ and $r_v = 1$ where the weak coupling limit breaks down.

In conclusion the FWHM of the generated pulse can be stretched or narrowed in comparison to the input pulses by tuning the relative velocities. When the idler travels at a slower velocity than the pump pulse the generated pulse will be narrowed, with maximum narrowing occurring when the idler pulse travels at half the velocity of the pump pulse. In the case where the idler pulse travels faster than the pump pulse there will be stretching in the idler.

4.5 Phase Matching

It has been noted in the previous section that the best shape transfer fidelity is achieved when the idler pulse velocity is equal to that of the input shaped pulse velocity. These velocities are determined by the refractive indices of the pulses, which in turn are dependent on the input angle of the pulses with regard to crystal optical axis, as shown in the equation below [38]

$$n_{\text{eff}}(\lambda, \theta) = \frac{1}{\sqrt{\left(\frac{\sin \theta}{n_e(\lambda)}\right)^2 + \left(\frac{\cos \theta}{n_o(\lambda)}\right)^2}}, \quad (4.33)$$

where θ is the angle between the propagation direction of the light and the optical axis of the nonlinear crystal, see figure 4.13. $n_e(\lambda)$ and $n_o(\lambda)$ are the wavelength dependent refractive indices of the extraordinary and ordinary polarised light. So far the pulses have been simulated to travel collinearly meaning that $\theta = 0^\circ$ for both input pulses and $n_{\text{eff}} = n_o$. By varying the angle of the input beams, the angle of the idler will change in order to conform to the phase matching condition so that

$$\begin{aligned} k_i &= k_p - k_s, \\ \frac{2\pi n_i(\lambda_i, \theta_i)}{\lambda_i} &= \frac{2\pi n_p(\lambda_p, \theta_p)}{\lambda_p} - \frac{2\pi n_s(\lambda_s)}{\lambda_s}. \end{aligned} \quad (4.34)$$

By choosing the correct combination of pump and signal angle we can tune the refractive indices so that $n_p \approx n_i$, ensuring optimal shape transfer. It has to be noted that not all pump and signal angle combinations will generate the idler wavelength λ_i , which might be required in a specific experiment. Clearly this parameter also has to be taken into consideration as well when choosing the input angles.

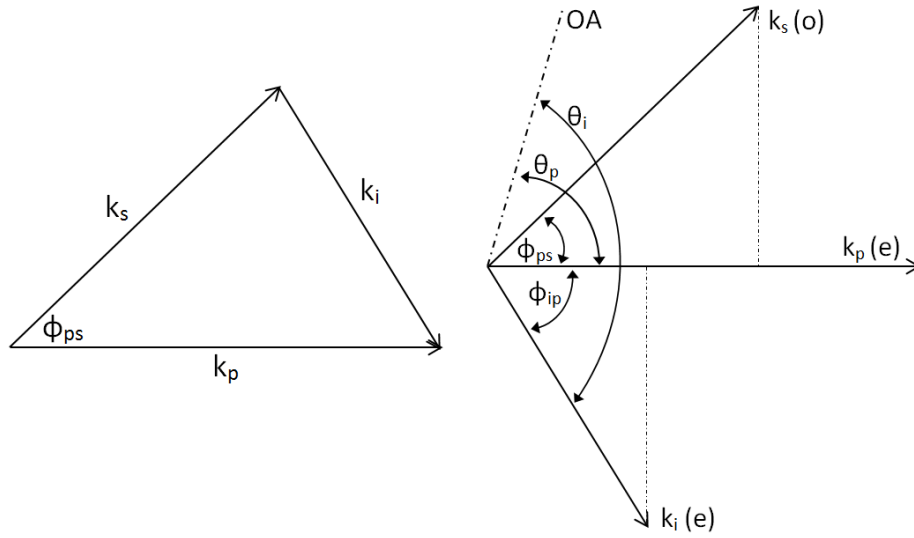


Figure 4.13: Phase matching diagram.

In figure 4.13 θ_p is the angle of the pump beam with the optical axis of the crystal, ϕ_{ps} is the angle between the pump and signal and ϕ_{ip} is the unknown angle between the pump and the idler, which is determined from the phase matching condition [38]. The change in idler angle and refractive index, with varying pump angle can be calculated from figure 4.13 starting by expressing k_i in terms of known variables and ϕ_{ip}

$$\begin{aligned}
 k_s \cos(\phi_{ps}) + k_i \cos(\phi_{ip}) &= k_p, \\
 k_s \sin(\phi_{ps}) - k_i \sin(\phi_{ip}) &= 0, \\
 k_i &= \frac{k_s \sin(\phi_{ps})}{\sin(\phi_{ip})}.
 \end{aligned} \tag{4.35}$$

Next we calculate ϕ_{ip}

$$\begin{aligned}
 k_s \cos(\phi_{ps}) + \left[\frac{k_s \sin(\phi_{ps})}{\sin(\phi_{ip})} \right] \cos(\phi_{ip}) &= k_p, \\
 k_s \cos(\phi_{ps}) - k_p &= - \left[\frac{k_s \sin(\phi_{ps})}{\sin(\phi_{ip})} \right] \cos(\phi_{ip}), \\
 \tan(\phi_{ip}) &= \frac{k_s \sin(\phi_{ps})}{k_p - k_s \cos(\phi_{ps})}, \\
 \phi_{ip} &= \arctan \left(\frac{k_s \sin(\phi_{ps})}{k_p - k_s \cos(\phi_{ps})} \right),
 \end{aligned}$$

with $\theta_i = \theta_p + \phi_{ip}$. Now we can write

$$k_i = \frac{2\pi n_{i, \text{eff}}}{\lambda_i} = \frac{2\pi}{\lambda_i \sqrt{\left(\frac{\sin \theta_i}{n_{i, e}}\right)^2 + \left(\frac{\cos \theta_i}{n_{i, o}}\right)^2}}. \quad (4.36)$$

From the Sellmeier equations we know that $n_i(e)$ and $n_i(o)$ are dependent on the wavelength. We now insert the Sellmeier equations [39]

$$\begin{aligned} n_e^2 &= A + \frac{B}{\lambda^2} + \frac{C}{\lambda^4} + \frac{D}{\lambda^6} + \frac{E}{(1 - F/\lambda^2)}, \\ \text{eg. } n_e^2 &= 5.76 + \frac{0.3879}{\lambda^2} - \frac{0.2288}{\lambda^4} + \frac{0.1223}{\lambda^6} + \frac{1.855}{(1 - 1780/\lambda^2)} \text{ for GaSe,} \end{aligned}$$

with the factors A,B,C,D,E and F, which are unique for each crystal and polarisation (o and e), into equation 4.36 for k_i . This allows us to calculate λ_i by substituting equation 4.35 into equation 4.36

$$\frac{k_s \sin(\phi_{ps})}{\sin(\phi_{ip})} = \frac{2\pi}{\lambda_i \sqrt{\left(\frac{\sin \theta}{n_{i, e}}\right)^2 + \left(\frac{\cos \theta}{n_{i, o}}\right)^2}}. \quad (4.37)$$

Now the wavelength of the idler can be calculated for specific input angles of the signal and pump pulses and from there the refractive index (n_i) of the idler pulse can be obtained. The solution of equation 4.37 can be multivalued but we select the physical solutions by choosing the upper and lower bounds of what λ_i can be.

4.6 Physical Examples

4.6.1 Type II Difference Frequency Mixing for Generating Mid-IR Pulses

To illustrate the method for calculating n_i in the previous section we investigate two concrete examples generating light in the short-wavelength infrared and far infrared regimes. For the short-wavelength infrared we consider GaSe to generate $1.6\mu\text{m}$, by mixing 795 nm and 1521.5 nm and for the far infrared we consider GaSe to generate $10\mu\text{m}$ by mixing 795 nm and 863.7 nm.

From equation 4.37 we can calculate the combinations of input angles that will produce the wanted λ_i , this is explored in the figures below for GaSe generating an idler of $1.6\mu\text{m}$.

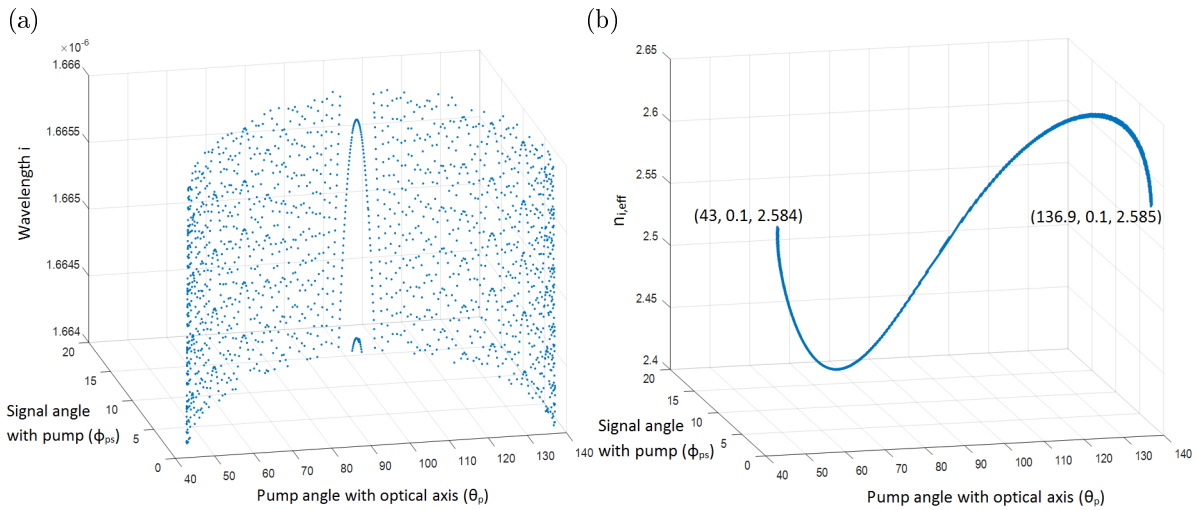


Figure 4.14: Input signal and pump angle vs (a) idler wavelength and (b) effective idler refractive index for generating $1.6\mu\text{m}$ in GaSe.

In figure 4.14(a) the input angle combinations that generate λ_i in the wavelength range $1.664 - 1.666\mu\text{m}$ are identified and plotted, with the corresponding refractive indices ($n_i(\lambda_i, \theta_i)$) for the values in figure 4.14(a), plotted in figure 4.14(b). The refractive index is dependent on wavelength as well as the angle of the idler with the crystal optical axis as indicated by equation 4.33. However, the refractive indices depend very weakly on this angle so that multiple points fall essentially on top of each other.

Next we investigate the relative velocities for the angle combinations by plotting, in figure 4.15(a), the relative velocities as a function of θ_p , with the relative velocities calculated using the refractive indices for all ϕ_{ps} angles considered in figure 4.14.

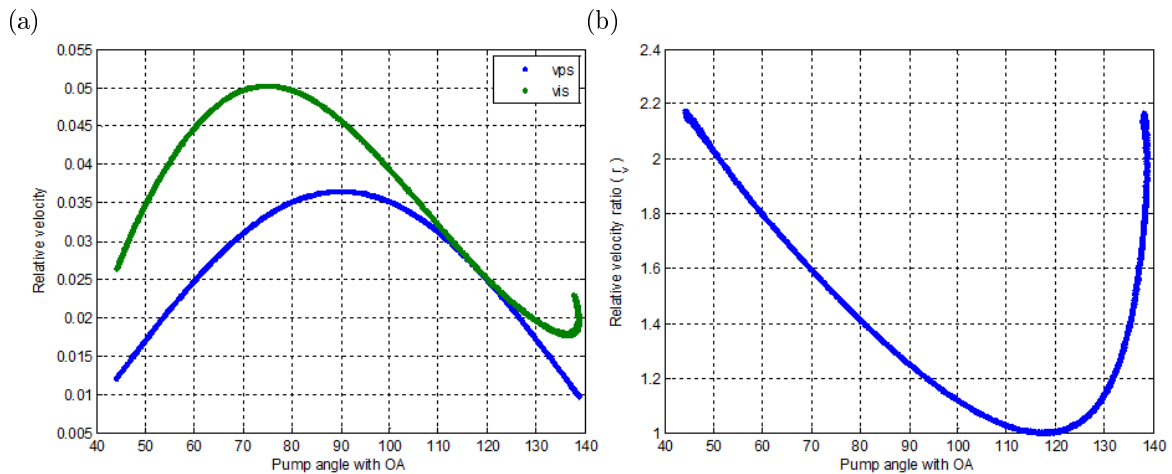


Figure 4.15: Input pump angle vs (a) relative velocities and (b) relative velocity ratio for generating $1.6\mu\text{m}$ in GaSe.

The signal angle corresponding to a specific v_{ps} and v_{is} can be looked up, if needed, using figure 4.14(b). In figure 4.15(b) the relative velocity ratios (r_v), corresponding to the relative velocities (v_{ps} and v_{is}) plotted in figure 4.15(a), are indicated. The ratio is close to 1 between $\theta_p = 115^\circ$ and 120° as expected from figure 4.15(a). In this case, where we want to generate $1.6 \mu\text{m}$, r_v is always larger or equal to 1, meaning we can either choose the angles for optimal pulse shape transfer ($r_v \approx 1$) or we can choose the idler pulse to be longer than the input pulses ($r_v > 1$), as predicted by our numerical simulations in section 4.4.

Next we investigate creating pulses in the far-IR by generating $10 \mu\text{m}$ through mixing 795 nm and 863.66 nm in a GaSe crystal. We follow a similar procedure to the previous case for generating $1.6 \mu\text{m}$, investigating which input pump and signal angle combinations will provide good shape transfer at the wanted wavelength. Since our model was purely collinear in previous sections, we first explore in figure 4.16 the outcome of a purely collinear setup, we change the pump angle with the optical axis of the crystal while keeping $\phi_{ps} = 0.001^\circ$ constant. In figure 4.16 we explore the generated idler wavelength and velocity ratios (r_v) for a varying θ_p and constant $\phi_{ps} = 0.001^\circ$.

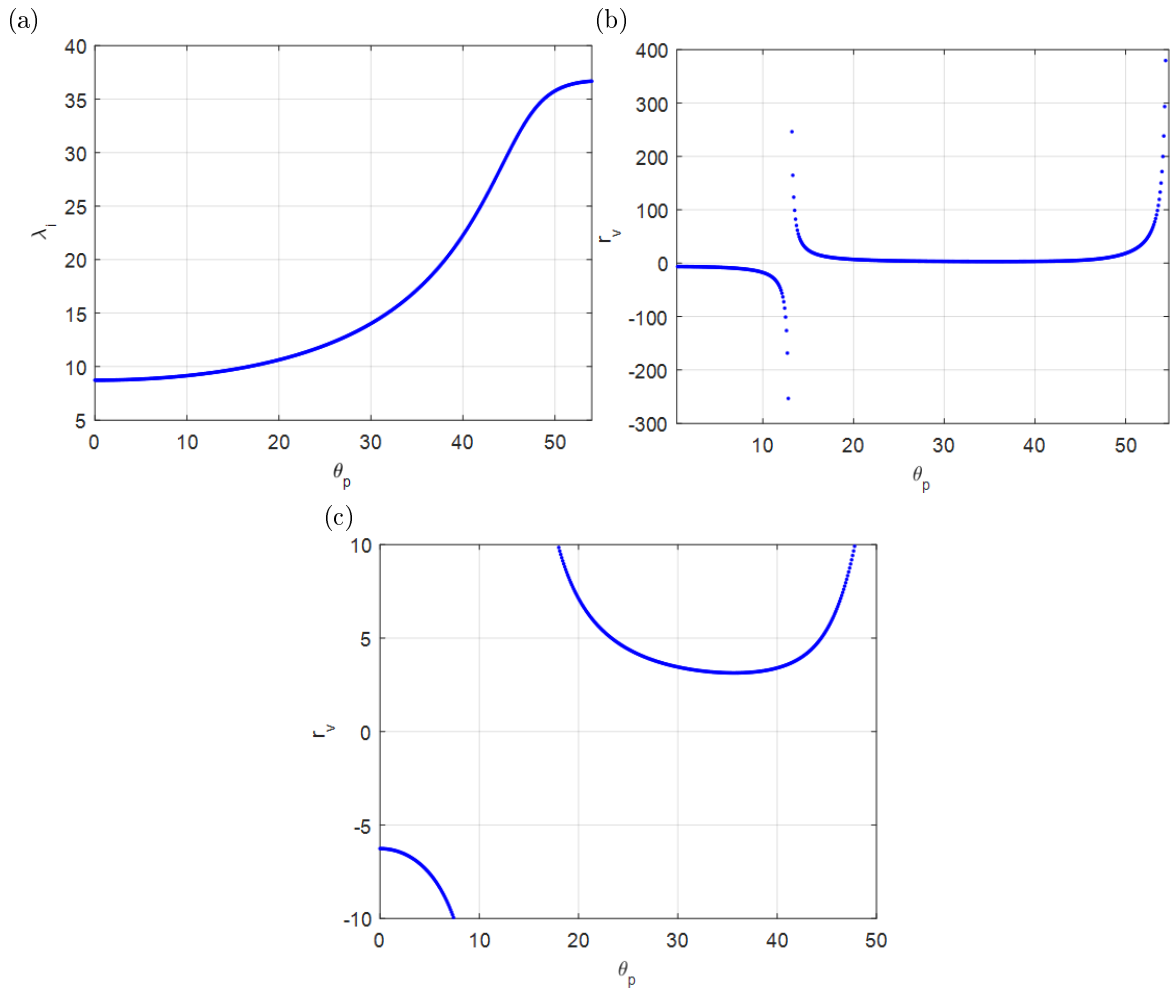


Figure 4.16: (a) Generated wavelengths for a collinear pump and signal configuration with changing pump angle θ_p . (b) Relative velocity ratio (r_v) with respect to changing θ_p and (c) zoomed in graph of 4.16(b) for constant $\phi_{ps} = 0.001^\circ$.

In figure 4.16(a) we see clearly that for a collinear setup, the wanted wavelength will be generated at a pump angle around 16° with the optical axis, but from figure 4.16(b) and (c) we can see that there will be no shape transfer and the generated pulse will be extremely broad due the velocity ratios r_v being equal to 16.37. With the collinear setup and only changing the pump angle with regard to the crystal optical axis, there is variation in r_v , but the extent of the variation is not sufficient for tuning of r_v between $r_v = 0$ and 3, see figure 4.16(b) and (c). For the best choice of pump angle θ_p ($35.4^\circ - 35.9^\circ$), where the relative velocity ratio $r_v \approx 3.1$, the pulse will still show minimal shape transfer and the desired wavelength will not be generated. Clearly the collinear setup is not sufficient for tuning r_v and so also not for efficient indirect pulse shaping in the far-IR.

Next we give up the constraint that the pump and signal are collinear; and the angles between the pump, signal and optical axis are varied, see figure 4.17 below. We can see that there are many angle variations between the input pulses, in figure 4.17(a), that will generate the needed relative velocities for good shape transfer as well as fall in the wanted wavelength regime.

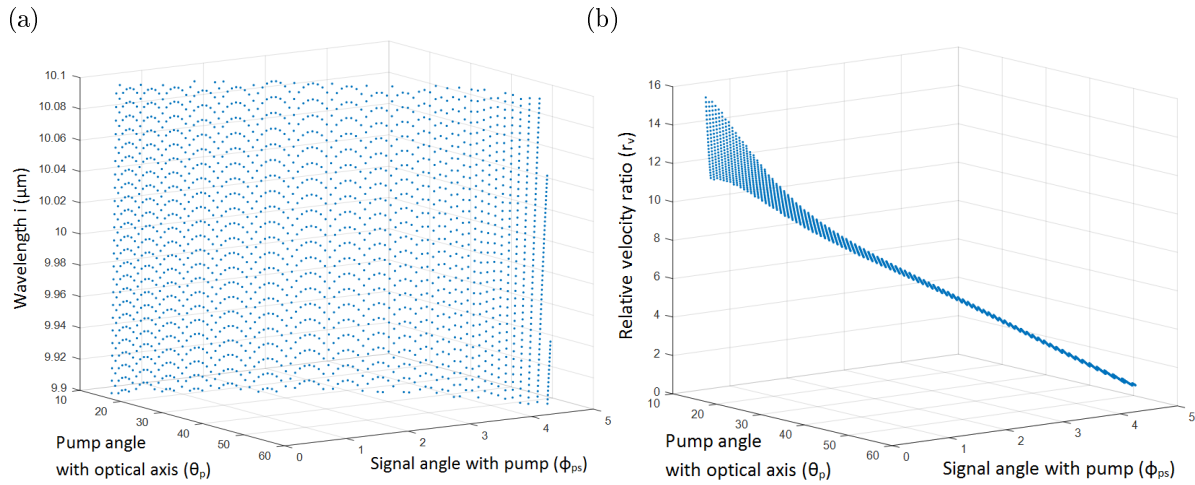


Figure 4.17: Varying pump and signal input angles vs (a) wavelength and (b) the relative velocity ratios (r_v) for generating $10\mu\text{m}$ in GaSe.

The angle combinations that will generate the wanted wavelength range are shown in figure 4.17(a) while the corresponding relative velocity ratios are shown in figure 4.17 (b). It is now possible to identify the angle combinations that will generate the correct wavelength, with the best possible shape transfer fidelity, as predicted by our model. In figure 4.18 we choose the appropriate input angles for generating a $10\mu\text{m}$ double pulse with optimal shape transfer by consulting figure 4.17(a) and (b).

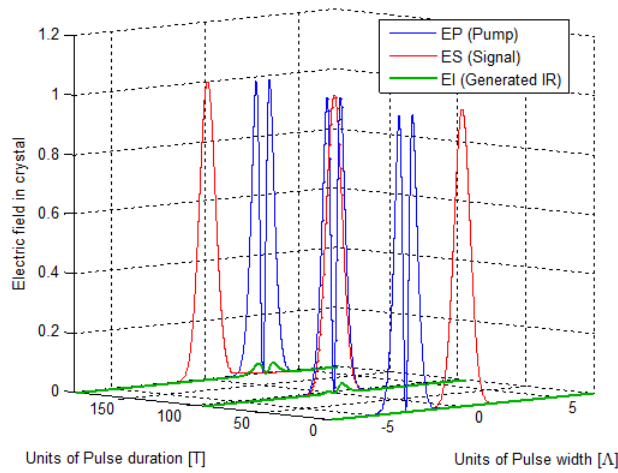


Figure 4.18: Simulating the generation of a $10\mu\text{m}$ double pulse in GaSe.

The input angles are selected to provide a velocity ratio as close to 1 as possible while still generating the wanted wavelength. By choosing $\theta_p = 56.2^\circ$ and $\phi_{ps} = 4.5^\circ$, moving away from a collinear setup, we have a velocity ratio (r_v) of 1.066. The shape transfer fidelity in figure 4.18 has an error of 8.5% with the wavelength of the generated idler very close to the desired wavelength, $10.05\mu\text{m}$. This shape transfer fidelity is not great, but it is much improved from what can be achieved in a collinear setup. The error can be decreased to 1.9%, with $r_v = 0.991$, by changing the input angles to $\theta_p = 56.9^\circ$ and $\phi_{ps} = 5.4^\circ$. But this will not generate the desired wavelength, but $8.41\mu\text{m}$.

In the collinear case it was not possible to achieve shape transfer with the fidelity in figure 4.18, since the angles could not be chosen to give a velocity ratio close enough to one. By taking into account tuning of the angle between the pump and signal pulse (ϕ_{ps}), thereby having more control over the refractive indices, it is possible to generate a larger range of r_v values. Our numerical model was set up for a collinear configuration since pulse movement in only the z axis of the crystal is considered. It is possible though, to incorporate the effect of small angles between the pump and signal, into our model since the error this will have on the velocity ratio will be small, making the collinear approximation in the model still accurate.

We now repeat a similar study with a BBO crystal, generating $1.6\mu\text{m}$. The phase matching graphs are unique for each type of nonlinear material, as well as the wavelengths of the input pulses. In figure 4.19 we calculated and plotted the relative velocities of the pump and idler pulse in a BBO crystal for the wavelength regime around $1.6\mu\text{m}$.

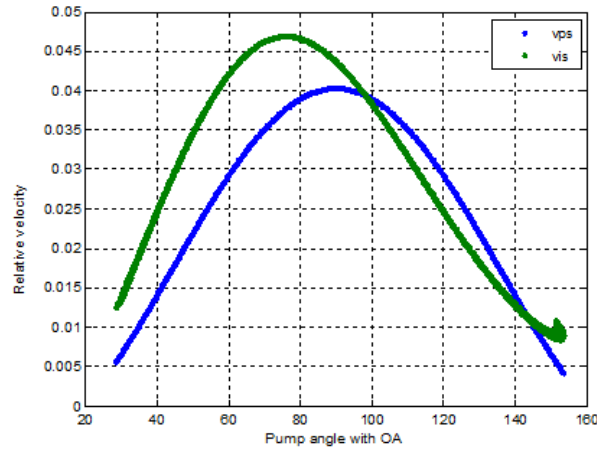


Figure 4.19: Relative velocities versus input angle for a BBO crystal.

It must be noted that in figure 4.19 varying angles between the input pulses (ϕ_{ps}) is employed in the calculation of the relative velocities, even if not indicated in the figure. Comparing figure 4.19 to figure 4.15(a) we can see that we have very different tuning curves for different crystals, even at similar input wavelengths and angles. There are two places where v_{ps} and v_{is} intersect ensuring very good transfer of the pulse shape at these angles.

4.6.2 Type I Frequency Mixing for Generating Near-IR

In the previous sections we used type II phase matching in all the calculations and simulations, due to the fact that longer (IR and far IR) wavelengths than the input wavelengths were generated. In the following section and chapters we want to generate a wavelength that is less complicated to measure with the equipment available in our laboratory. To that end we simulate type I frequency mixing in a BBO where $\omega_i = \omega_p - \omega_s$, with ω_i the generated wavelength (with o polarisation), $\omega_s = \frac{2\pi c}{797\text{nm}}$ the shaped signal (with o polarisation) and $\omega_p = \frac{2\pi c}{398.5\text{nm}}$ the frequency converted pump (with e polarisation). Since our input wavelengths are in the near IR and visible regime, a different mixing scheme is necessary to generate the idler wavelength in the near IR. In figure 4.20 the calculations in section 4.5 are repeated for type I frequency mixing.

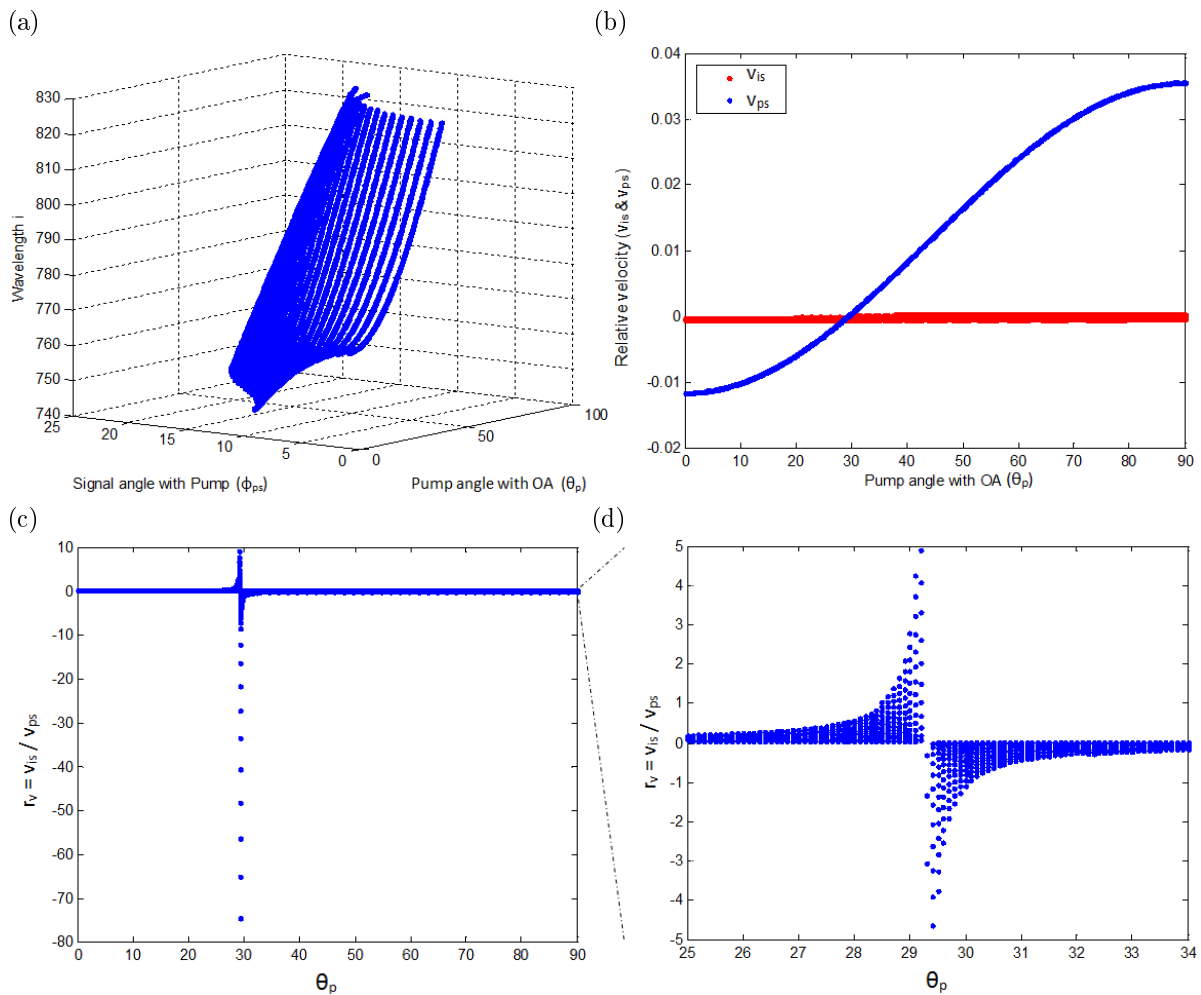


Figure 4.20: (a) Idler wavelength versus angle between signal and pump (ϕ_{ps}) and input angle of pump (θ_p), (b) relative velocities vs incident pump angle (θ_p), (c) relative velocity ratio r_v vs incident pump angle (θ_p) and (d) zoomed r_v vs θ_p for BBO.

It must be noted that plots (b) - (d) in figure 4.20 include velocities for all ϕ_{ps} angles indicated in figure 4.20(a). In figure 4.20(a) the wavelengths of the idler pulse are plotted with regard to the input angle between the pump and signal (ϕ_{ps}) and the angle of the pump with the crystal optical axis (θ_p). The relative velocities of the pump (v_{ps}) and idler (v_{is}) are plotted with regard to the angle of the pump with the optical axis, in figure 4.20(b). Overlap of v_{ps} and v_{is} occurs at a small set of angles between approximately 28.9° and 29.25° . In figure 4.20(c) we see the velocity ratio (r_v) versus the pump angle with the optical axis. Figure 4.20(d) shows a smaller range of angles and r_v , effectively zooming in on the graph. At a pump angle around 29° , there are more variation in r_v with different angles between the pump and signal with ϕ_{ps} not shown on the graph. This corresponds to tunability of the shape

transfer fidelity, generated pulse widths and idler pulse wavelength. Since the BBO crystal that we are using in the experiment is cut at a angle of 29.2° with the crystal optical axis and from figure 4.20(d), it is clear that it would be most convenient to keep the input angle for the pump pulse (θ_p) constant at 29.2° and varying the angle between the pump and signal pulse (ϕ_{ps}). By simulating the DFG process for a few select values of ϕ_{ps} we can see how r_v and the generated idler pulse is influenced by varying this angle. In figure 4.21 the 398.5 nm Gaussian pump pulse travels over the 797 nm shaped signal pulse from right to left, with the travel direction of the idler dependent on the sign of r_v .

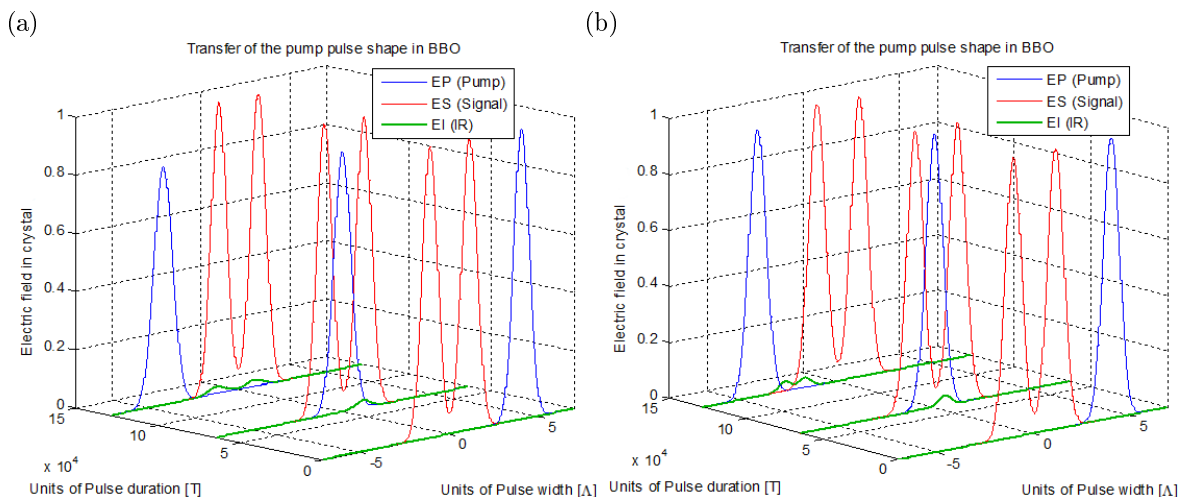


Figure 4.21: Generation of shaped idler for $\theta_p = 29.2^\circ$ and (a) $\phi_{ps} = 0.01^\circ$, and (b) $\phi_{ps} = 2.5^\circ$.

In figure 4.21(a) with $\phi_{ps} = 0.01^\circ$, the corresponding r_v will be equal to 0.0272, giving a reasonable shape transfer with an error of 5.5%. We refer to the delay between the two peaks of the generated pulse divided by the delay between the input shaped pulse peaks as the pulse separation ratio and this ratio is measured as 0.97 in figure 4.21(a). In figure 4.21(b) $\phi_{ps} = 2.5^\circ$ so that $r_v = 0.2823$, giving a transfer error of 63%. The distance between the peaks of the idler pulse is less than that of the input pump giving a pulse separation ratio of 0.72. The transfer efficiencies for various angles are indicated in table 4.3(a). The ratios between the peak separation of the input signal and generated idler, corresponding to r_v , is calculated and indicated in table 4.3(a).

The best shape transfer occurs when $r_v = 0$ (which correspond with $\phi_{ps} = 0$) and not when $r_v = 1$ as in the previous section, e.g. figure 4.18. This is due to the pulses moving in the reference frame of the shaped signal pulse, with the optimal shape transfer occurring when the idler pulse moves at the same velocity as the shaped pulse i.e. $n_i = n_s$.

Next we investigate the effect of r_v on the FWHM of the generated pulse due to two Gaussian input

pulses and observing for which input angles there will be narrowing and broadening in the idler pulse. In figure 4.22 a single idler pulse is generated with the input angle θ_p kept constant at 29.2° with varying ϕ_{ps} . In the following numerical simulations (figure 4.22 and 4.23) the pump and signal pulse have the same FWHM, which is used as the length unit Λ .

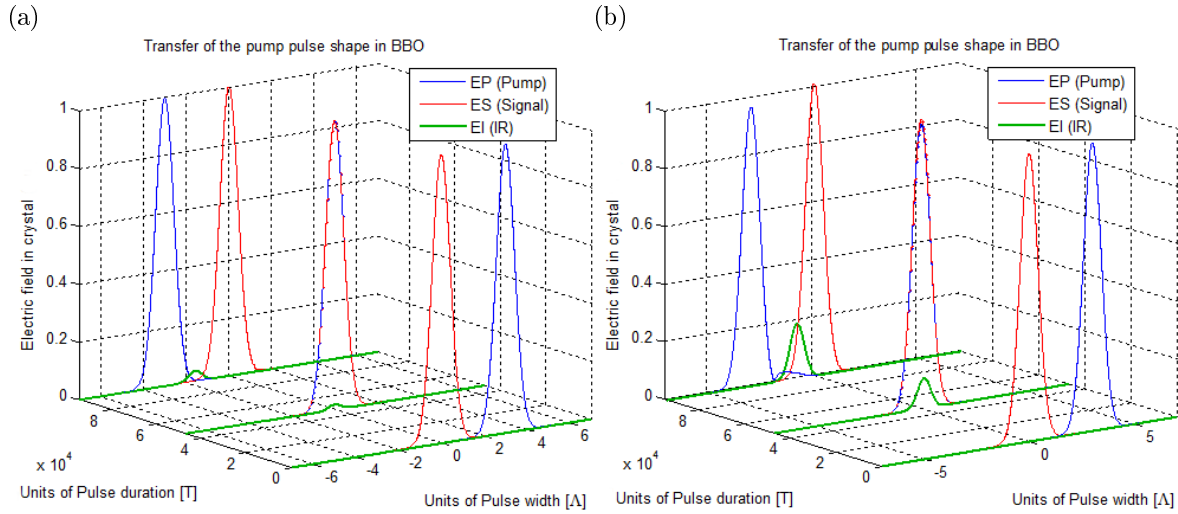


Figure 4.22: Generation of single idler pulse for (a) $\phi_{ps} = 3.4^\circ$, $r_v = 0.5042$ and (b) $\phi_{ps} = 2.4^\circ$, $r_v = 0.2663$.

In figure 4.22(a), $\phi_{ps} = 3.4^\circ$ so that $r_v = 0.5042$ with the idler pulse narrower than the input pulses with the FWHM equal to 0.7080. In figure 4.22(b) $\phi_{ps} = 2.4^\circ$ causing r_v to be equal to 0.2633. This causes less narrowing in the idler, with the FWHM equal to 0.7928. The different FWHM for the idler pulse, each time generated with different ϕ_{ps} , is indicated in table 4.3(b). In figure 4.23 we investigate two examples with broadening of the idler pulse FWHM.

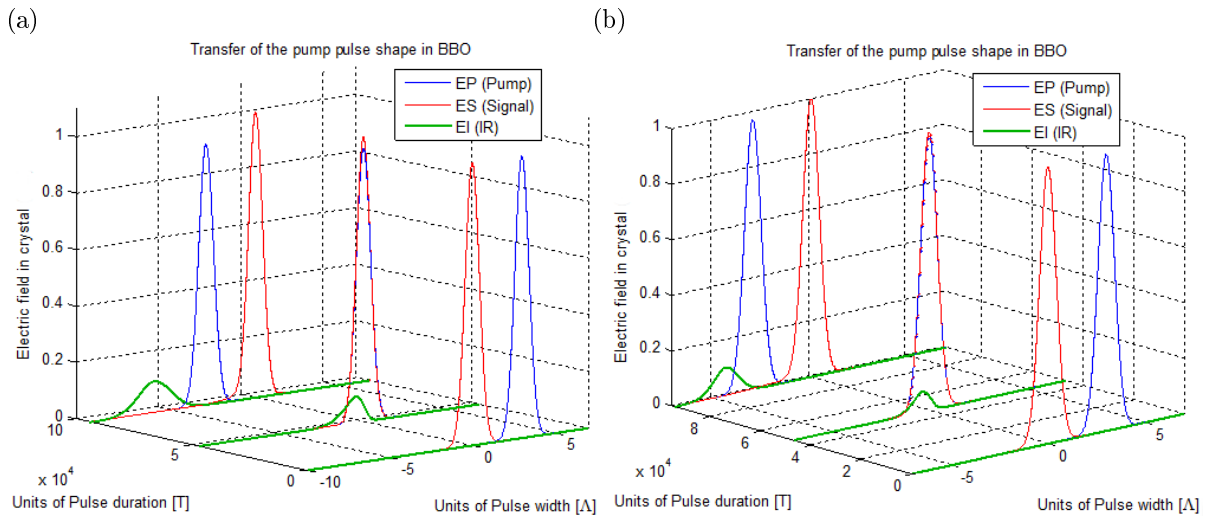


Figure 4.23: Generation of a single idler pulse for (a) $\phi_{ps} = 7^\circ$, $r_v = 2.019$ and (b) $\phi_{ps} = 5.9^\circ$, $r_v = 1.449$.

In figure 4.23(a) at $\phi_{ps} = 7^\circ$, the idler is broadened with the FWHM equal to 2.34 with $r_v = 2.019$. In figure 4.23(b) $\phi_{ps} = 5.9^\circ$ and $r_v = 1.449$ causing less broadening with the FWHM of the idler equal to 1.54. Since it is experimentally challenging to set an angle with the needed accuracy, we simulate the generation of the idler for different angles around the desired values to investigate the tolerance.

| ϕ_{ps} | r_v | Error | Separation Ratio |
|-------------|--------|-------|------------------|
| 0.010 | 0.0272 | 5.5% | 0.974 |
| 1.0 | 0.0687 | 14.3% | 0.931 |
| 1.5 | 0.1164 | 24.8% | 0.884 |
| 2.0 | 0.1911 | 41.8% | 0.809 |
| 2.5 | 0.2823 | 63.1% | 0.718 |

| ϕ_{ps} | r_v | FWHM |
|-------------|---------|-------|
| 0.01 | 0.02723 | 0.991 |
| 1 | 0.06875 | 0.954 |
| 2.0 | 0.1911 | 0.854 |
| 3.0 | 0.3970 | 0.750 |
| 3.4 | 0.5042 | 0.708 |
| 4.0 | 0.6849 | 0.788 |
| 5.0 | 1.049 | 1.09 |
| 6.0 | 1.494 | 1.61 |
| 7.0 | 2.019 | 2.34 |
| 8.0 | 2.629 | 3.20 |

Table 4.3: (a) Error and peak separation ratio for a simulated double pulses at different ϕ_{ps} and (b) FWHM for simulated single pulses at different ϕ_{ps} for constant $\theta_p = 29.2^\circ$.

As seen from table 4.3(a), for good shape transfer of a shaped pulse and in order to keep the shape transfer error below 10% the angle ϕ_{ps} has to be kept between 0° and 0.70° . To narrow the FWHM of the generated idler to less than 0.8, according to table 4.3(b), ϕ_{ps} must be between 2.55° and 4.05° .

Next we investigate the effect of small variations in the input pump angle with the crystal optical axis (θ_p), while keeping the angle between the pump and signal constant at $\phi_{ps} = 3.4^\circ$, with ϕ_{ps} chosen to cause the idler to be narrowed. The change in r_v with varying θ_p is indicated in table 4.4.

| θ_p | r_v |
|------------|-------|
| 29.05 | 0.206 |
| 29.10 | 0.253 |
| 29.15 | 0.333 |
| 29.20 | 0.504 |
| 29.25 | 1.097 |
| 29.28 | 4.540 |

Table 4.4: Pump angle with the crystal optical axis (θ_p) and corresponding velocity ratio (r_v) for constant $\phi_{ps} = 3.4^\circ$.

We see that small variation in θ_p on the order of 0.1 degrees have a large effect on the velocity ratios (r_v). For the case of narrowing in the idler pulse, the angle θ_p has to be between 29.10° and 29.23° to produce a FWHM no less than 0.8. We compare the change in r_v , due to tuning in θ_p and ϕ_{ps} , in figure 4.24. This is done by plotting the data in table 4.3 and 4.4 on the same graph.

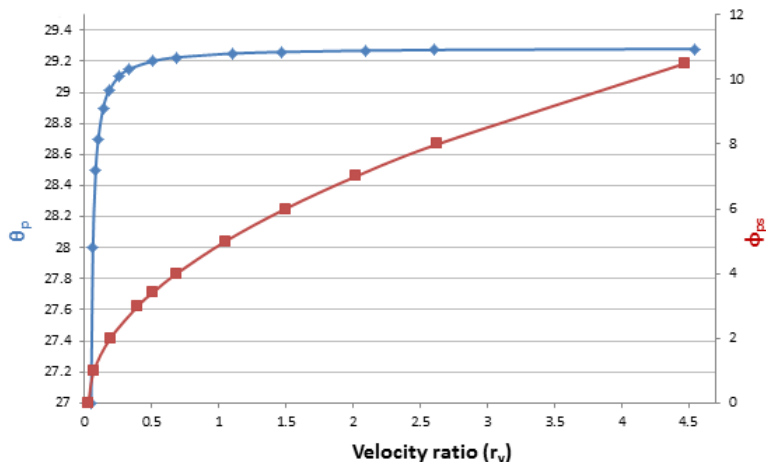


Figure 4.24: Blue curve: Angle between the pump and optical axis (θ_p) with constant $\phi_{ps} = 3.4^\circ$. Red curve: Angle between the pump and signal (ϕ_{ps}) with constant $\theta_p = 29.2^\circ$ versus relative velocity ratio (r_v).

From figure 4.24 it is clear that θ_p has a large effect on r_v between $\theta_p = 29.0^\circ$ and $\theta_p = 29.28^\circ$ and while varying ϕ_{ps} between 0 and 0.5 has a large effect on r_v , tuning ϕ_{ps} in that region it is still less sensitive than tuning θ_p between 29.0° and 29.28° . Because of the sensitivity of θ_p between 29.0° and 29.28° it is more convenient to work with θ_p smaller than 29.0° , if possible, so that a small change in θ_p will have a smaller effect on r_v .

In this section we found that the velocity ratio (r_v) determines the characteristics of the idler. By carefully selecting the input angles (θ_p and ϕ_{ps}), effectively setting r_v , we can broaden, narrow or

transfer a pulse shape with high fidelity to the idler pulse. Varying the angle between the pump pulse and the optical axis of the crystal (θ_p) between 29.0° and 29.2° has a very large effect on the velocity ratio (r_v), while variation in the angle between the pump and signal pulse (ϕ_{ps}) has a smaller effect.

4.7 Phase Transfer

Up to now only the transfer fidelity of the shaped pulse amplitude envelope has been investigated, but that is just one aspect of pulse shaping. The transfer of the phase from the pump pulse to the idler pulse is simulated in a BBO crystal for the 398.5 nm input pump pulse and the 797 nm signal pulse, generating a 797nm idler pulse, identical to the type I mixing process in subsection 4.6.2. The appropriate input angles for the most effective shape transfer were identified in subsection 4.6.2 as $\theta_p = 29.2^\circ$ and $\phi_{ps} = 0.01^\circ$, so that $r_v = 0.027$. In figure 4.25 we simulate the transfer of an arbitrarily chosen phase, added to the input signal pulse, to the idler pulse.

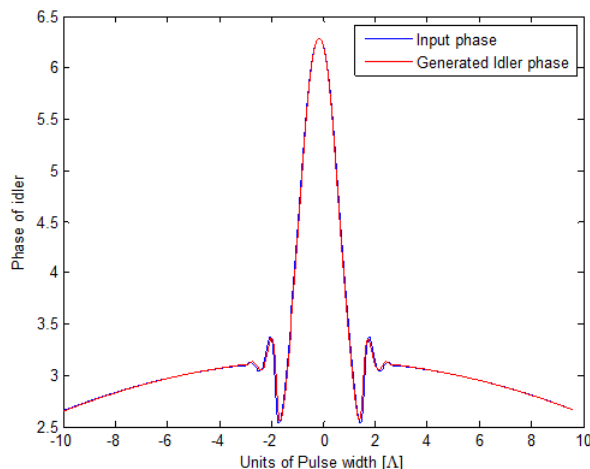


Figure 4.25: Phase of input pulse and generated Idler pulse.

The output phase corresponds well with the input phase with a error of 0.66%, see figure 4.25. From this we can conclude that the phase transfer is very good for $r_v = 0.0272$ and shows similar behavior to the studied shape transfer of the amplitude envelope.

Chapter 5

Experimental Equipment

We have simulated DFG for various crystals and wavelengths in the previous chapter. In the coming chapters we want to experimentally explore the behavior that was exhibited in the numerical simulations. We therefore need a complete characterisation of the experimental setup and the equipment. For DFG we need to be able to generate pulses through frequency conversion, do temporal pulse shaping and measure the generated pulses. To do this we make use of an Optical parametric amplifier (TOPAS), a spatial light modulator (SLM) and an intensity autocorrelator, respectively.

5.1 Laser Stability

The experimental results of the DFG will be measured using intensity autocorrelation and we will need to compare the DFG output pulses with the input pulses. To be able to do the comparison, we need to investigate the stability of the input pulses from the amplifier. This is done by measuring the temporal pulse envelope and duration of the femtosecond amplifier output. We test the stability of the output by measuring and averaging several intensity autocorrelation traces of the amplifier beam and calculating the standard deviation in the envelope, which is indicated by the error bars in figure 5.1. The FWHM of the averaged autocorrelation traces is 169 fs.

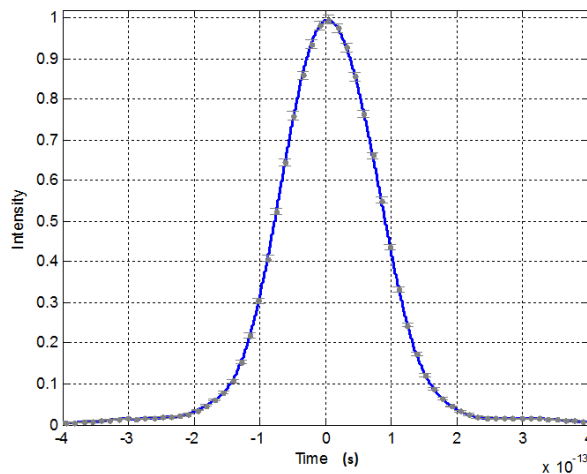


Figure 5.1: Average of the amplifier autocorrelation trace with error bars.

The error bars in figure 5.1 are an indication of the statistical uncertainty (or standard deviation) in the mean, after N autocorrelation measurements, calculated as the root mean square deviation of the amplifier intensity fluctuation divided by the square root of the number of measurements

$$\text{Statistical uncertainty} = \frac{\sqrt{\frac{1}{N} \sum_{i=1}^N (z_i - u)^2}}{\sqrt{N}}, \quad (5.1)$$

with z_i the measured intensity of the autocorrelation pulses, u the averaged intensity of the pulse measurements and $N = 21$ the number of autocorrelation measurements. From figure 5.1 we can see that the amplifier output is stable, with the fluctuation in the peak intensity 4.5% and the fluctuation in the FWHM 2.9%. The fluctuations in the laser pulse intensity and temporal FWHM of the autocorrelation traces are sufficiently small for our experiments.

The shape and temporal duration of a pulse can be determined by performing a deconvolution of the measured autocorrelation trace. The trace is deconvolved by taking the Fourier transform of equation 2.11 and solving for the intensity, $I(\omega)$, in the frequency domain. This comes down to taking the square root of the Fourier transform of the autocorrelation trace and transforming it back to the temporal domain. The deconvolution of the autocorrelation trace in figure 5.1 is shown in figure 5.2.

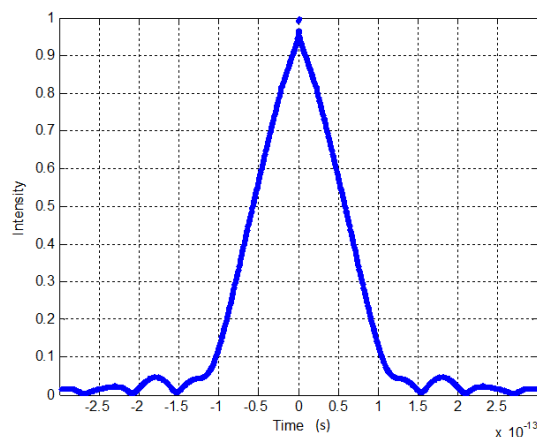


Figure 5.2: Deconvolution of autocorrelation trace.

The pulse in figure 5.2 has a FWHM of 120 fs, as expected, but not the expected Gaussian pulse shape. This deviation from a Gaussian shape is due to the slight asymmetry of the experimental autocorrelation trace in figure 5.1. Since the deconvolution of figure 5.1 does not give a perfect Gaussian pulse shape, a theoretical fit can be done to the pulse to approximate the pulse shape.

A different method would be to apply a Gaussian fit, indicated in figure 5.3(a), to the experimental autocorrelation trace in figure 5.1 and deconvolve the theoretical fit.

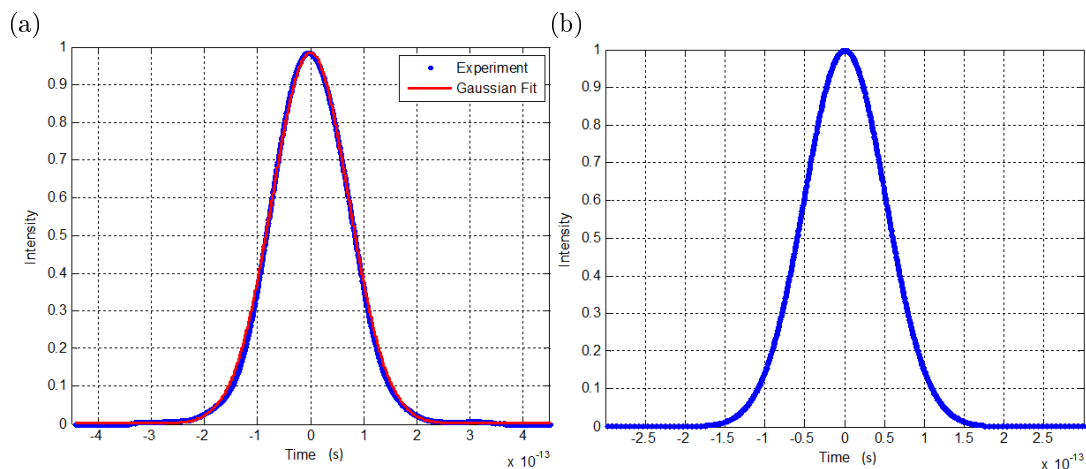


Figure 5.3: (a) Gaussian fit of experimental trace in figure 5.1 and (b) deconvolution of the Gaussian fit in figure 5.3(a).

The Gaussian pulse in figure 5.3(b) is the deconvolution of the Gaussian fit in figure 5.3(a) and has a FWHM of 120 fs, which corresponds to the FWHM of the pulse in figure 5.2.

5.2 SLM Assisted Autocorrelation

Intensity autocorrelation and FROG measurements have previously been discussed in section 2.4. The experimental setup for these measurements can be significantly simplified by using an SLM instead of a beamsplitter and a translation stage. A double pulse with a specific delay between the two pulses is created using the SLM, similarly to the double pulse created in section 3.4.1 [34]. This is similar to using a beam splitter to create two identical pulse moving on different beam paths. The time delay (τ) between the two pulses is decreased incrementally by loading a new transfer function on the SLM with different τ each time so that the delay between the double pulses becomes shorter with each new τ value, until the two pulses overlap and move apart again. This has the same effect as using a translation stage in the autocorrelation setup to change the path length between the two pulses, see figure 2.4. The two pulses are focused into a nonlinear crystal and the SFG output is measured with a photo diode or spectrometer (depending on the desired pulse information the user wants extracted) resulting in an autocorrelation or FROG trace. There will be significant background noise due to the collinear nature of this method and second harmonic generation, generating the same wavelength as the SFG signal. We execute an SLM assisted autocorrelation and FROG trace in figure 5.4 for a single pulse.

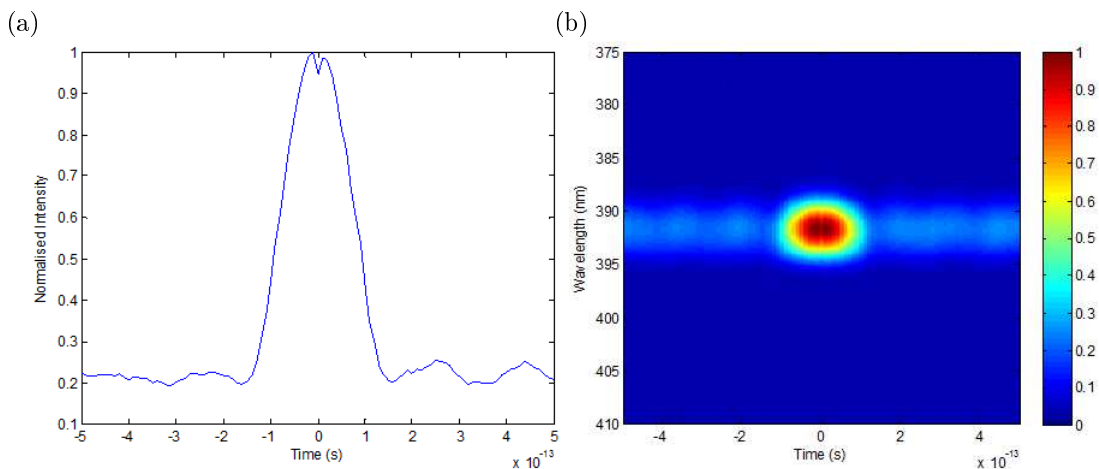


Figure 5.4: SLM assisted (a) autocorrelation and (b) FROG trace.

The FWHM of the measured autocorrelation trace in figure 5.4(a) is 113 fs, taking into account the deconvolution factor. Similarly a FROG trace can be measured by substituting the photo diode with a spectrometer 5.4(b). This setup, using an SLM, has the advantage of less optics and no beam splitter, which means that there will be less chirp added to the pulse, in comparison to the

experimental setup in figure 2.4. This technique is also less complicated since no additional alignment of an autocorrelation setup is necessary, with only a SLM, the appropriate nonlinear crystal and a photodiode or spectrometer needed. The nature of our experiment, implementing indirect pulse shaping, makes SLM assisted autocorrelation not feasible and so we will be using the experimental setup in figure 2.4 for autocorrelation.

5.3 SLM

The calibration and theory of the SLM has already been discussed in chapter 3. In this section we will look at the characterisation of the SLM.

5.3.1 Calibration of the Pixels and Spectrum

Next we investigate which pixels in the SLM display correspond to each wavelength. Both displays are set at maximum transmission and the spectrum of the output beam is measured to have a bandwidth of 15 nm, see figure 5.5(a). Selected pixels are blocked and the resulting spectrum is recorded, see figure 5.5(b). The series of pixels that were blocked are pixel 310 to 317, pixel 400 to 404 and pixel 450 to 455.

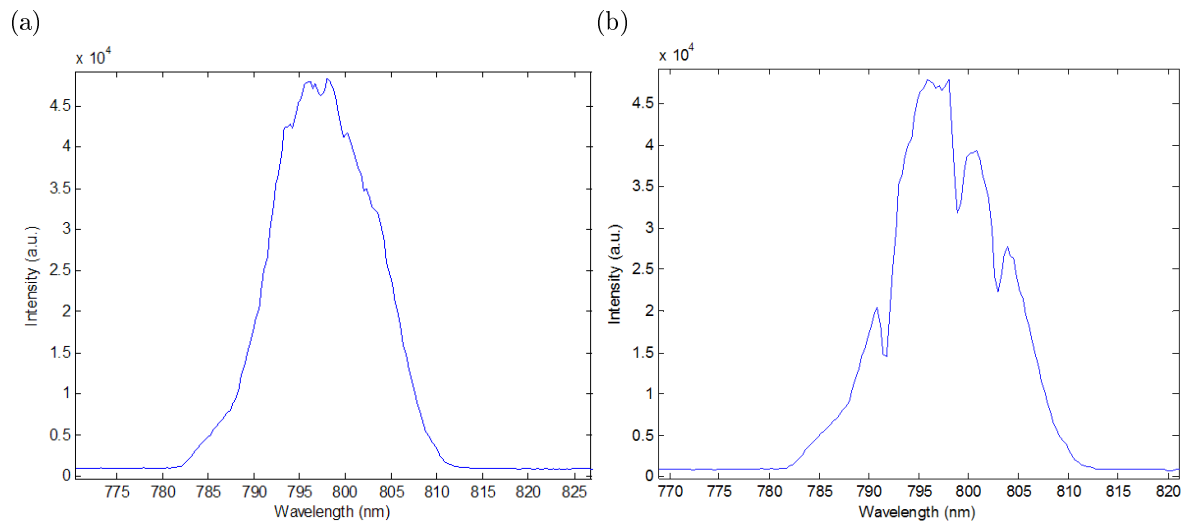


Figure 5.5: (a) The spectra after the 4f setup and (b) the same spectra with blocked pixels.

We can conclude from figure 5.5(b) that pixel 313, 402 and 452 correspond 791.8 nm, 798 nm and 803 nm respectively. From this we can calculate that the resolution of the SLM in our setup

$$\begin{aligned} \frac{\Delta\text{nm}}{\Delta\text{pixel}} &= \frac{803\text{ nm} - 791.8\text{ nm}}{452 - 313}, \\ &= 0.08 \frac{\text{nm}}{\text{pixel}}. \end{aligned}$$

In figure 5.5(b) the intensity of the the blocked wavelengths are not zero, this is due to the large laser spot size of the input beam in the 4f setup, with the input spot diameter at 1 cm. Referring to the folded 4f experimental setup in figure 3.3(a), the flat mirror used to fold the 4f setup is positioned at the focal plane of the plano-concave lens meaning that the SLM is not at the exact focal position of the plano-concave lens but instead in front of it. Because the spot falling on the grating is so large and due to the position of the SLM, the wavelength components that are falling on the SLM display overlap, each wavelength component is diffracted onto multiple pixels. Using the calculated resolution, the spectrum can now be calibrated to show the pixels, see figure 5.6.

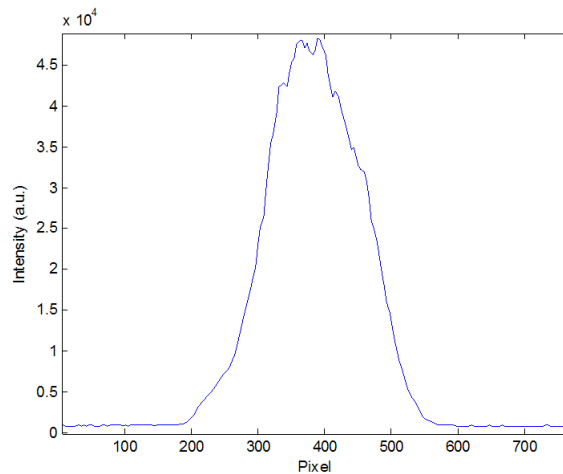


Figure 5.6: Spectrum calibrated for corresponding SLM pixels.

The center wavelength in figure 5.6 is at pixel 378 with the FWHM from pixel 300 to 478. Accurate knowledge of the SLM wavelength resolution is necessary for identifying the frequency at the first and last pixel, which is needed in order to create the patterns for pulse shaping.

5.3.2 Measuring the Pulse After the 4f Setup

It is necessary to know what effect the SLM and 4f setup has on the pulse when programmed to pass through unshaped. If the 4f setup is not correctly aligned the output pulse will not resemble the input pulse, with changes in the intensity envelope and phase. Autocorrelation was used to measure and compare the pulse shape and FWHM before and after the 4f setup for an input Gaussian pulse with a

FWHM of 123 fs. The pulse measured after the 4f setup, with both SLM displays made transmissive, is shown in figure 5.7 with a Gaussian envelope and FWHM of 123 fs.

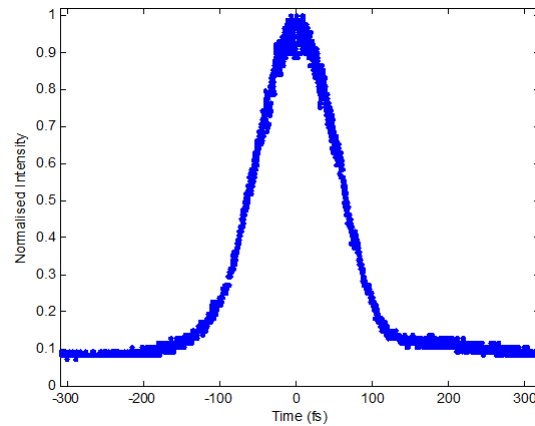


Figure 5.7: Trace of pulse after the 4f setup.

The pulse duration as well as temporal envelope before and after the 4f setup are the same and we conclude that the 4f setup is correctly aligned with correct spatial and spectral compression after the SLM.

5.3.3 SLM stability

Similarly to section 5.1, where the stability of the laser pulses were investigated, the pulses shaped by the SLM have to be characterised for complete understanding of the eventual experimental results. The shaped pulse is measured using autocorrelation, similarly to section 5.1, but for a double pulse shaped by the SLM. The double pulse is created in a similar fashion to the double pulse in section 3.4.1. In figure 5.8 the shaped pulse autocorrelation measurements of a double pulse with a peak separation of 174 fs are averaged and plotted.

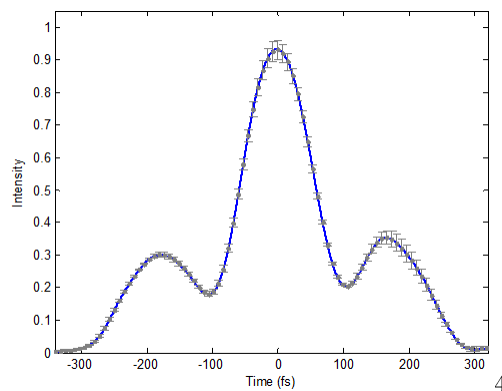


Figure 5.8: Average of the measured pulses.

The error bars give the statistical uncertainty in the mean of the autocorrelation measurements, see equation 5.1 with $N = 3$. We calculate the amplitude error of the main peak in figure 5.8 to be in the order of 4% and the fluctuation in the FWHM 3.4%. The stability of the laser output in section 5.1 has peak intensity fluctuations on the order of 4.5% and 2.9% for the pulse FWHM, with the laser pulse functioning as the input of the SLM. This means that, since the error in the peak of the shaped pulse is less than that of the input pulse (with a difference of 0.5%) and the fluctuation in the FWHM is larger (with a difference of 0.5%), we conclude that the SLM adds minimal to no fluctuations to the pulse and is stable. The autocorrelation trace in figure 5.8 is not perfectly symmetric due to a slight misalignment in the autocorrelator and a slow drift in laser power.

It is not possible to accurately deconvolve the autocorrelation trace in figure 5.8 since vital phase information was lost in the autocorrelation measurement.

From subsection 5.3.1 and figure 5.5(b) we conclude that the frequency mask used for pulse shaping ($H(\omega)$), which is applied to the frequency components of the incoming pulse, will have an offset. Simulated in figure 5.9(a) is a mask with an offset, applied to the frequency spectrum of a single Gaussian pulse.

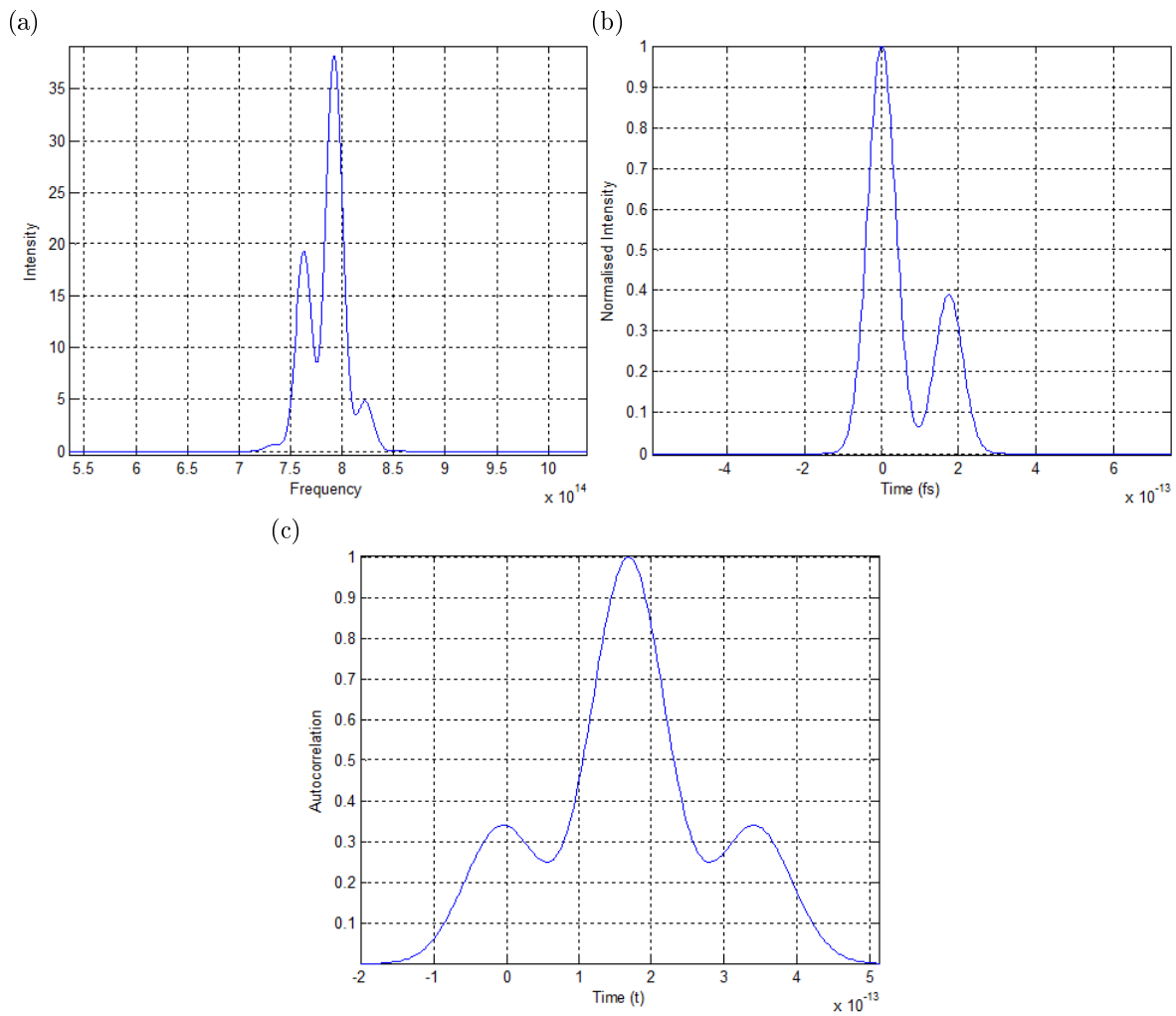


Figure 5.9: Simulation of (a) the mask, $H(\omega)$, with an offset added, (b) the resulting shaped pulse and (c) the autocorrelation trace for the pulse in figure (b).

Due to the offset in the mask, the temporal shaped pulse is not a perfect double pulse, but an unequal double pulse, indicated in figure 5.9(b). The autocorrelation trace of this unequal double pulse, indicated in figure 5.9(c), has side peaks below half the height of the main peak; compared to a double pulse autocorrelation trace in figure 2.8(b) where the side peaks' height are at precisely half of the main peak. When comparing the simulated autocorrelation trace for an unequal double pulse to the experimentally measured autocorrelation trace in figure 5.8 and taking into consideration the observations made in subsection 5.3.1, we conclude that the pulse shaped in our experimental setup is an unequal double pulse.

5.4 TOPAS

In the numerical simulations different wavelengths are mixed in a nonlinear crystal to create the shaped DFG pulse. Experimentally, an unshaped pulse at a different wavelength from the laser fundamental (795 nm) is necessary for DFG. This pulse is generated using an optical parametric amplifier (OPA) or nonlinear crystal. We use an OPA for the generation of wavelengths in the visible to IR regime while a nonlinear crystal can be used to generate half of the fundamental (397.5 nm) through second harmonic generation (SHG), where the generated pulse is at half the wavelength of the input pulse. In this section we characterise the TOPAS-C, which is a commercial OPA that can generate 1140 nm to 2600 nm [2]. By adding additional frequency mixers the range can be extended to the UV and far-IR wavelength ranges. For the purpose of this study we only investigate the TOPAS with one mixer, extending the wavelength range to 550 nm - 2600 nm. The TOPAS requires a short Gaussian pulse to operate effectively so that it is not possible to use a shaped pulse as input.

5.4.1 Setup

The TOPAS works in two stages: converting the laser fundamental (795nm) into the programmed wavelength and amplification using two BBO crystals. The input beam is split in two parts, see figure 5.10. In the first stage the transmitted beam size is reduced with a two lens telescope (L1 + L2), since the beam size is too large for some of the optics. The now smaller beam is split again into two beams at a second beam splitter (BS2). The transmitted beam is focused into a sapphire plate which generates a white-light continuum (very broad range of wavelengths) while the reflected beam travels to a BBO crystal (BBO1). The reflected beam interacts nonlinearly with the white light continuum in BBO1, with $\omega_3 = \omega_1 - \omega_2$, where ω_3 is a programmed wavelength between 1140 nm and 2600 nm. The angle of the BBO crystal with the input beams and the delay between the white light and 795 nm beam determines the wavelength of the generated signal (ω_3). The signal beam is reflected and expanded with L6 + L7 lens pair to fall on the second BBO crystal (BBO2).

In the second stage, the beam reflected from the first beam splitter (the pump beam) is focused down by a lens (L8) onto a smaller spot and collimated by M1, which is a curved mirror, and reflected to BBO2. At BBO2, the pump beam interacts with the signal (ω_3) which amplifies the signal strength. The path length of the two interacting beams (pump and signal) in the crystal must be the same with DP 1-2, which are Brewster angled plates, used to change the path lengths. In the mixer the wavelength of the amplified IR signal from the TOPAS is halved in BBO3 with the appropriate input

angle, through second harmonic generation, to generate a visible signal. In the case where the wanted wavelength is between 1140 and 2600 nm the mixer is not necessary and the BBO is rotated out of the beam path.

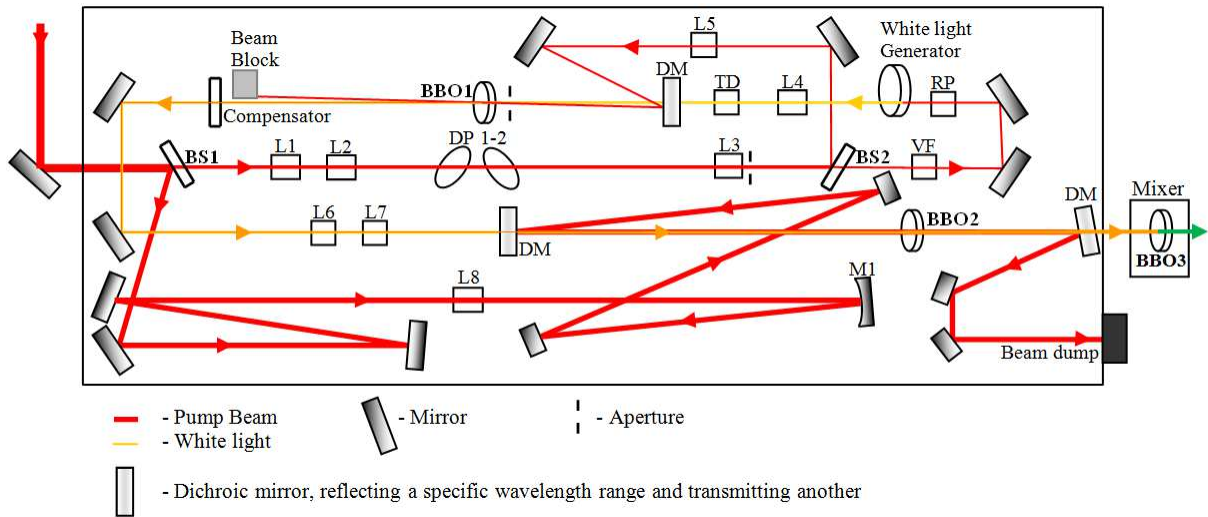


Figure 5.10: TOPAS configuration.[2]

In figure 5.10, L are Lenses, BS beam splitters and VF a variable density filter.

5.4.2 Characterisation of the TOPAS Output

It is important to have knowledge of the beam generated by the TOPAS to effectively use the TOPAS for generating the wanted wavelengths. We investigate the measured spatial profile and the wavelength conversion efficiency curve of the TOPAS output. The spatial profile of the TOPAS output has been measured with a Spiricon camera, see figure 5.11(a).

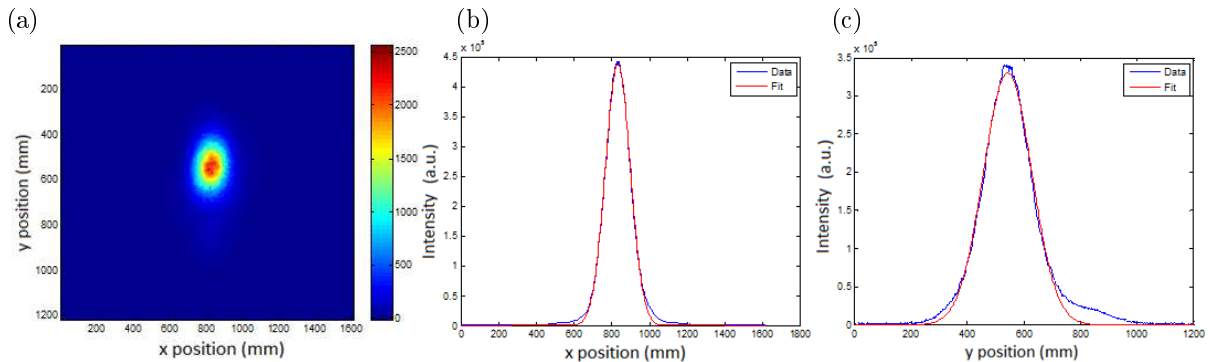


Figure 5.11: Spatial profile of 863.66 nm generated pulse from the TOPAS (a) camera image, (b) sum of the x profile and (c) y profile with a Gaussian fit.

The TOPAS output is elongated in the y-axis, see figure 5.11(a). Even though the output is not a round spot the profiles are Gaussian in each axis 5.11(b) and (c), with the FWHM of the x-axis 160 mm and 180 mm in the y-axis. In figure 5.11(c) the pulse is not completely Gaussian with a side lobe. The elongated spot and side lobe in the y axis is due to the telescope L8 and M1 not compressing the x- and y-axis of the pump beam perfectly. The TOPAS has different schemes for generating different wavelength ranges, as well as different efficiencies for generated wavelengths, see figure 5.12.

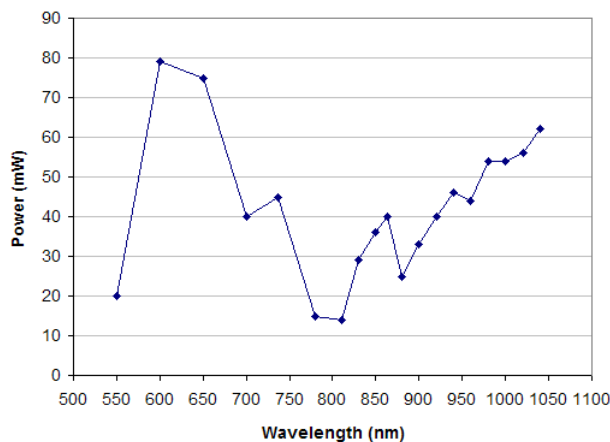


Figure 5.12: TOPAS output power vs wavelength.

The wavelength conversion is best around 600 nm at 79 mW, while it is worst around 800 nm, with 815 nm at 14 mW, see figure 5.12. 800 nm is so close to the input wavelength (795 nm) that it is not possible to distinguish between the input wavelength and generated 800 nm, which is why it is not indicated in figure 5.12. Using this graph it is possible to select, in the case where the nature of the experiment allows for it, wavelengths with good conversion efficiencies to work with.

Chapter 6

Difference Frequency Generation of Shaped Pulses

In chapter 4 we simulated DFG of shaped femtosecond pulses in different crystals and at different wavelength regimes. We found that for specific refractive indices, the generated pulse can be stretched, compressed or have a identical shape as that of the input pulse. The refractive indices can be tuned by changing the angles between the input pulses and the crystal optical axis. Next we want to compare the numerical model with experimental results. In order to produce shaped pulses in the far IR regime, indirect pulse shaping has to be used, as previously simulated. Unfortunately it is not possible to characterise a idler pulse generated in the far IR with the instruments at our disposal. Therefore, to verify the predictions of our model we implement DFG in a wavelength regime accessible to us, leaving upgrading of our system to the far IR regime for future work. The experiment is done for the three different identified cases: shape transfer, compression and stretching; and compared to the simulations. We generate a 797 nm idler pulse in a BBO crystal, as simulated in section 4.6.2. The phase matching scheme is shown in figure 6.1 below, with $k = \frac{2\pi}{\lambda}$ the wavenumber.

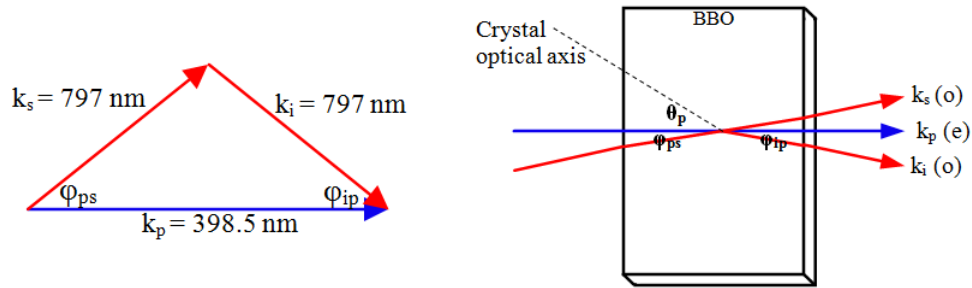


Figure 6.1: Phase matching scheme for Type I frequency mixing.

For the difference frequency generation process to take place and be efficient, phase matching has to occur where $k_i \cos(\phi_{ip}) = k_p - k_s \cos(\phi_{ps})$, see figure 6.1.

6.1 Experimental Setup

The experimental setup has been briefly discussed in section 2.5. The shaped signal pulse at the laser fundamental wavelength (797 nm) must interact with an unshaped pump pulse converted to the appropriate wavelength (398.5 nm) in a nonlinear crystal (BBO), see figure 6.2.

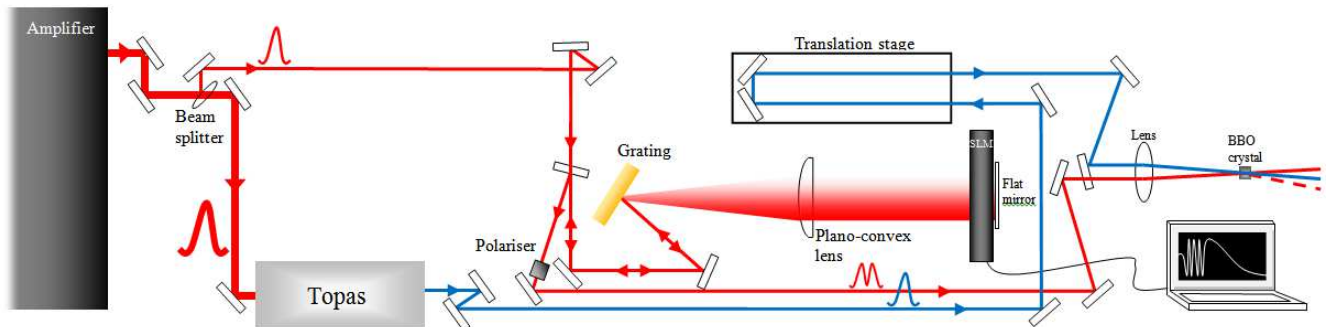


Figure 6.2: Difference frequency generation experimental setup.

The incoming fundamental beam, at 797 nm, is split with a 80/20 beam splitter so that 80% of the light is reflected to the frequency conversion setup which can be by the TOPAS or a nonlinear crystal, illustrated in figure 6.2. We choose to work with a nonlinear crystal since the wavelength required to generate the wanted DFG wavelength is the second harmonic of the fundamental wavelength. In the generation of a far-infrared idler pulse the TOPAS would have been necessary for frequency conversion. 20% fundamental is transmitted to the 4f setup with the SLM. The transmitted beam is shaped with the SLM and functions as the signal, while the reflected beam is frequency converted to function

as the pump. The optical path length of the pump is adjusted, after the nonlinear crystal using a translation stage, so that the optical path lengths of the 2 pulses correspond to each other. The two pulses are focused into a BBO crystal at a small angle below 6° to ensure that all three output pulses can be isolated yet still have long spatial overlap inside the BBO crystal. Keeping the angles small further ensures that our experiment is very close to the collinear model that we investigated in preceding sections. When the signal and pump pulses overlap temporally and spatially in the crystal, the shaped idler pulse is generated through DFG. The optimal angles for each individual case identified in subsection 4.6.2 (shape transfer, temporal narrowing and temporal stretching) will be investigated experimentally in the next section.

6.2 Experimental Results

Experimentally we generate 797 nm in a BBO crystal using difference frequency generation, as simulated in subsection 4.6.2 and experimentally described in section 6.1. The DFG is done for different angles between the pump and signal (ϕ_{ps}) with the angle of the pump with the crystal optical axis (θ_p) kept constant at 29.2° . Since the BBO crystal is cut at 29.2° , this would correspond to the pump beam falling on the surface of the crystal normally, see figure 6.1. Three different cases are investigated, with the angle ϕ_{ps} chosen in each instance to induce narrowing or stretching of the generated pulse, in comparison to the input FWHM; or optimal transfer of the input pulse shape to the generated pulse, as simulated in subsection 4.4 and 4.6.2. The input as well as generated pulses are measured using intensity autocorrelation, as described in subsection 2.4.1.

The pulse from the amplifier has a FWHM of 125.5 fs, see figure 6.3 for the autocorrelation trace of the pump pulse from the amplifier. Several DFG pulses are measured using the intensity autocorrelator and averaged. The DFG pulse was generated for the case where the angle between the pump and signal pulse is measured to be $\phi_{ps} \approx 1.46^\circ \pm 0.90^\circ$. This input angle between the pump and signal beam (ϕ_{ps}) is determined by measuring the distance between the two beams falling on a flat surface at a specific distance from the BBO crystal. By using the distance between the input beams and the distance to the BBO, simple trigonometry can be used to calculate the input angle, assuming that the pump beam falls on the BBO at 90° to the crystal surface. In each case the uncertainty in the measurement can be calculated using the spot sizes of the two beams and the thickness of the BBO crystal. We have taken into account Snell's law, after measuring the angle ϕ_{ps} outside the crystal. A

rather large uncertainty in the measurement arises due to the pump-signal beam separation being in the same order as the beam spot size at the location of the measurement. Since the pump beam (398.5 nm) is at 90° with the surface of the crystal, the pump angle with the optical axis is $\theta_p \approx 29.2^\circ \pm 0.1^\circ$. Several autocorrelation measurements of the DFG pulses are taken and the averaged signal is shown in figure 6.3. After the pulses are averaged, a fit is done to the averaged pulse with the error bars indicating the statistical uncertainty in the mean after the amount of autocorrelation measurements, using equation 5.1.

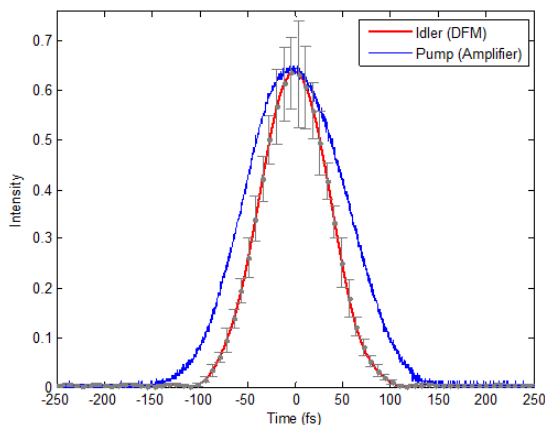


Figure 6.3: Comparison between the averaged pulses and amplifier input.

The averaged pulse has a FWHM of 86.3 fs, see figure 6.3. The averaged pulse is compared to the input pulse from the amplifier and the pulse width ratio $\left(\frac{\text{FWHM}_{\text{AV}}}{\text{FWHM}_{\text{AMPL}}}\right)$ 0.69 can now be used to calculate the difference between the simulation and experiment. If we assume that $\phi_{\text{ps}} = 1.46$ exactly, we calculate that we require $\theta_p = 29.27^\circ$, in order to cause exactly the amount of temporal narrowing in the idler that was measured in the experiment. This suggests that the pump is incident 0.07° away from the normal to the crystal surface ($\Delta\theta_p$), with the difference in angle of incidence falling well within in the uncertainty of the pump angle measurement.

The uncertainty in the FWHM of the idler pulse, that results from intensity fluctuations, indicates that we have set the angle θ_p within ± 0.01 of a degree.

The spectrum of an averaged input pulse and temporally narrowed output idler pulse are measured using a spectrometer and shown in figure 6.4. These measurements were done for a different case than above where there was less narrowing in the idler pulse, with the idler FWHM equal to 97 fs and signal input FWHM 111.5 fs.

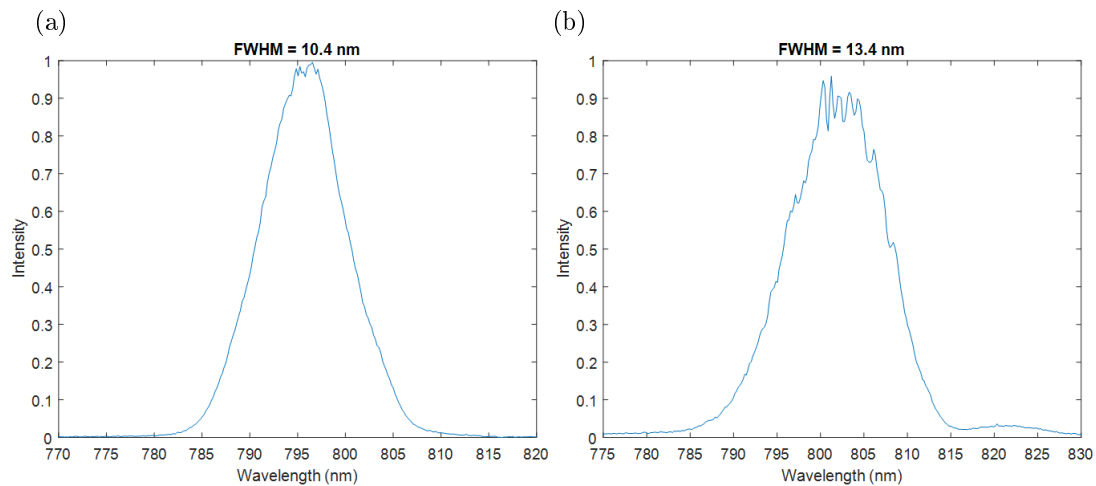


Figure 6.4: Averaged spectrum indicating the (a) input signal pulse and (b) generated idler pulse for a temporally narrowed idler pulse.

The generated idler pulse spectral bandwidth is broader than the input pulse 10.4 nm bandwidth (figure 6.4(a)) with the idler bandwidth 13.4 nm (figure 6.4(b)). The broadened frequency spectrum is consistent with the measured temporal narrowing, which was measured using autocorrelation traces. The noise on the idler spectrum in figure 6.4(b) is due to the low intensity of the generated pulse.

In figure 6.5 we see an example of broadening in the generated idler pulse. The angle between the pump and signal is measured as $3.55^\circ \pm 1.20^\circ$ and the pump beam with the crystal optical axis is $29.2^\circ \pm 0.2^\circ$. The input signal pulse from the Amplifier has a FWHM of 118 fs and the averaged DFG idler pulse has a FWHM of 166.8 fs.

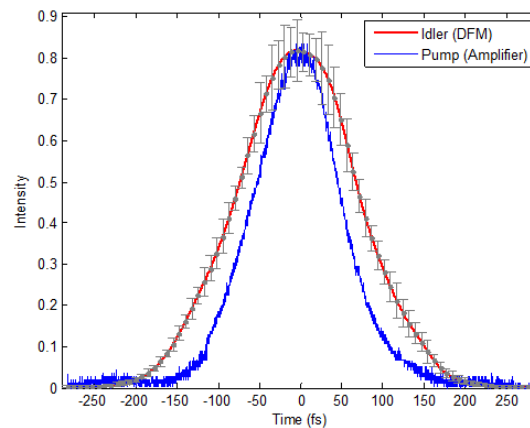


Figure 6.5: Comparison between the average pulses and amplifier input.

When comparing the input and DFG pulse, the generated pulse is 1.4 times longer, see figure 6.5. If we assume that ϕ_{ps} equals exactly 3.55° , we find through simulation that the required pump angle to account for the exact amount of temporal broadening in the idler (DFG) pulse compared to the input pulse is $\theta_p = 29.25^\circ$. Comparing the simulated angle with the known input angle, the difference is $\Delta\theta_p = 0.05^\circ$ with the difference falling well within the uncertainty of the pump angle.

Finally we investigate the transfer of an unequal double pulse to the idler pulse through DFG, with the pulse shaped by the SLM using the previously discussed 4f setup. Through the theory and simulations in section 4.6.2 we found that the angle between the pump and signal (ϕ_{ps}) pulses must be 0° for optimal shape transfer to occur, when $\theta_p = 29.2^\circ$ which corresponds to a collinear setup. For our choice of input wavelengths it is not possible to work in such a configuration since we would not be able to distinguish between the input signal pulse and the generated idler pulse, since they have exactly the same wavelength. The solution is to work at a small angle in order to have spatial separation between the input and generated beams. The LC SLM, which is situated in a 4f setup (discussed in chapter 3), is used to shape the unequal double pulse signal in figure 6.6 using the method and patterns explained in section 3.4.1.

The angle between the pump and signal pulse is measured as $\phi_{ps} \approx 0.88^\circ \pm 0.47^\circ$ with the uncertainty in the angle of the pump beam measured as $\theta_p \approx 29.2^\circ \pm 0.1^\circ$. The separation between the main and side peak of the input and averaged idler pulses in figure 6.6 are 173.7 fs and 131.6 fs respectively.

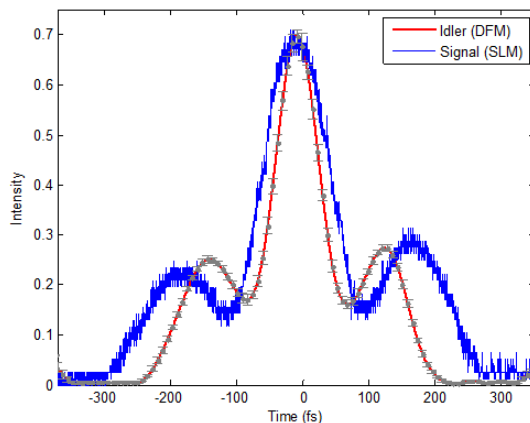


Figure 6.6: Comparison between the average pulses and SLM input.

The separations in the idler peak, in figure 6.6 are clearly narrower than that of the input signal pulse

and is due to the non-collinear experimental setup, as previously discussed. Instead the angle between the input pump and signal pulses is $0.88^\circ \pm 0.47^\circ$. When we assume that $\phi_{ps} = 0.88$ exactly, we can calculate the pump angle required to cause the precise amount of narrowing in the idler pulse peak separation, shown in figure 6.6, as $\theta_p = 29.28^\circ$. The difference between the theoretical and crystal cut angles, $\Delta\theta_p = 0.08^\circ$, falls in the angle uncertainty measurement.

The intensity of the generated idler wavelength is in each case low due to second harmonic generation in the idler pulse converting the newly generated 797 nm into 398.5 nm as it travels through the BBO crystal, which is not measured by the intensity autocorrelator.

In each of the 3 cases above, the difference between the known crystal optical angle and theoretical input angles can be attributed to the uncertainty in the angle alignment. However, the experimentally measured results are, in each case consistent with our model falling within the uncertainty of these angle measurements. We conclude that the experimental measurements correspond well with the numerical simulations.

Chapter 7

Summary

The main aim of this study has been to provide a recipe for achieving high fidelity pulse shape transfer through difference frequency generation. This was done through a detailed study using numerical simulations to identify critical factors that influence the fidelity of the pulse shape transfer to the desired wavelength. Finally we implemented DFG into an experiment, demonstrating three cases for pulse generation that were identified in the numerical simulations and compare this to the simulations.

While investigating a limiting case, where we worked in the weak coupling limit, we identified the factors that influence the generation of the idler pulse as the relative velocities and the nonlinear coupling strengths of each pulse. A parametric study was used to determine the extent of the influence of these parameters on the shape transfer as well as the FWHM of the idler pulse. We found that the relative velocities play a critical role in the characteristics of the idler pulse, while the coupling strengths of each pulse has a minimal influence when the fields intensity are kept low. On further investigation of the effect of the velocity ratio on the generated idler pulse, it was found that in the case where the velocities of the shaped input and idler pulses are equal, the transfer of a pulse shape to the idler will be near perfect. Narrowing of the idler pulse will occur when the input pulse is moving faster than the generated pulse and broadening of the idler pulse will occur when the idler pulse velocity is faster than the input pulse.

The difference in velocity of each pulse determines the duration, in time, that the pulses overlap and interact in the crystal. Temporal broadening of the idler occurs when the idler pulse travels faster than the pump pulse. While the pump and signal pulse overlap and generate the idler pulse, the idler

radiation that has already been generated is traveling away from the still overlapping pump and signal pulses, stretching the pulse. The faster the idler travels compared to the pump pulse, the more the pulse will be stretched. Maximum temporal narrowing of the idler pulse occur when the idler pulse moves at half the velocity of the pump pulse. When the pump pulse travel over the signal pulse the idler is generated, but the pump pulse is traveling at twice the velocity of the idler and reduce the pump and signal pulse interaction time to a short period. The pump travels away from the signal and idler, effectively creating a narrower idler pulse. In the case where the idler has the same velocity as the shaped pulse, they overlap perfectly the entire time, which ensures perfect shape transfer.

We implemented DFG in an experiment and identified the relationship between the angles of the input pulses with the optical axis of the nonlinear crystal and the velocity ratio, using phase matching relations. This makes it possible to select the angles of the two input pulses to produce the necessary velocities to control the idler pulse shape characteristics. When comparing the measured idler pulse to the simulations, the difference fell within the angle measurement uncertainty and corroborated our theoretical findings.

We leave upgrading of our system to generate wavelengths in the far IR regime, using a GaSe crystal, for future work. The far-IR pulses would be implemented for direct manipulation of the electronic ground state vibrational or ro-vibrational dynamics of a chosen molecule, using a genetic algorithm [11].

At the completion of this study it was found that very similar observations regarding the influence of velocity mismatch were made in the context of second harmonic generation by Wang et al. [40]. A theoretical and experimental investigation of the type II second harmonic generation in lithium triborate crystal was done and it was found that by tuning the group velocity mismatch, it is possible to transfer the intensity envelope as well as the phase profile of a shaped pulse to a wavelength in the UV.

Bibliography

- [1] Jenoptik, *SLM-S640d Technical Documentation*, 2009.
- [2] Topas-C, *Light Conversion, User's Manual*.
- [3] F.F. Crim. Vibrational state control of bimolecular reactions: Discovering and directing the chemistry. *Acc. Chem. Res.*, 32:877–884, 1999.
- [4] A Lindinger, C Lupulescu, M Plewicky, F Vetter, A Merli, S.M. Weber, and L Woste. Isotope selective ionization by optimal control using shaped femtosecond laser pulses. *Physical Review Letters*, 93:1–4, 2004.
- [5] H.G. Breunig, A Lauer, and K.M. Weitzel. Control of branching ratios in the dissociative ionization of deuterium chloride. *The Journal of Physical Chemistry Letters A*, 110:6395 – 6398, 2006.
- [6] J.J. Field, R Carriles, K.E. Sheetz, E.V. Chandler, E.E. Hoover, S.E. Tillo, A.W. Hughes, T.E. Sylvester, D Kleinfeld, and J.A. Squier. Optimizing the fluorescent yield in two-photon laser scanning microscopy with dispersion compensation. *Optics Express*, 18:13661 – 13672, 2010.
- [7] M Tsubouchi, A Khramov, and T Momose. Rovibrational wave-packet manipulation using shaped midinfrared femtosecond pulses. *Physical Review A*, 77:1 – 12, 2008.
- [8] J. Konradi, A.K. Singh, and A. Materny. Selective excitation of molecular modes in a mixture by optimal control of electronically nonresonant femtosecond four-wave mixing spectroscopy. *Journal of Photochemistry and Photobiology A: Chemistry*, 180:289 – 299, 2006.
- [9] D.J. Tannor and S.A. Rice. Control of selectivity of chemical reaction via control of wave packet evolution. *J. Chem. Phys.*, 83:5013, 1985.

- [10] H. Schworer, R Rausch, M. Heid, and W. Keiefer. Femtosecond vibrational wavepacket spectroscopy in the electronic ground state of K_2 . *Chemical Physics Letters*, 285:240–245, 1998.
- [11] L.E de Clercq, L.R. Botha, E.G Rohwer, H Uys, and A Du Plessis. Optimal control of the population dynamics of the ground vibrational state of a polyatomic molecule. *Proc. of SPIE*, 7925, 2011.
- [12] D. Oron, N Dudovich, and Y. Silverberg. Femtosecond phase-and-polarization control for background-free coherent anti-stokes raman spectroscopy. *Phys. Rev. Letters*, 90:1813–1859, 2004.
- [13] S. Roy, P. Wrzesinski, D. Pestov, T. Gunaratne, M. Dantus, and J. R. Gord. Single-beam coherent anti-stokes raman scattering spectroscopy of N_2 using a shaped 7 fs laser pulse. *Appl. Phys. Letters*, 95:074102, 2009.
- [14] M. P. A. Branderhorst, P. Londero, P. Wasylczyk, C. Brif, R. I. Kosut, H. Rabitz, and I. A. Walmsley. Coherent control of decoherence. *Science*, 320:638–643, 2008.
- [15] A.M. Weiner, J.P. Heritage, and E.M. Kirschner. High-resolution femtosecond pulse shaping. *Optical Society of America*, 5:1563 – 1572, 1988.
- [16] D. Meshulach, D. Yelin, and Y. Silberberg. Adaptive real-time femtosecond pulse shaping. *Journal of Optical Society of America B*, 15:1615 – 1619, 1998.
- [17] T. Brixner, A. Oehrlein, M. Strehle, and G Gerber. Feedback-controlled femtosecond pulse shaping. *Applied Physics B*, 70:119 – 124, 2000.
- [18] G. Stobrawa, M. Hacker, T. Feurer, D. Zeidler, M. Motzkus, and F. Reichel. A new high-resolution femtosecond pulse shaper. *Applied Physics B*, 72:627 – 630, 2001.
- [19] J.C. Delagnes, A. Monmayrant, P. Zahariev, A. Arbouet, B. Chatel, B. Girard, and M.A. Bouchene. Compensation of resonant atomic dispersion using a pulse shaper. *Applied Physics B*, 86:573 – 578, 2007.
- [20] Antoine Monmayrant and Beatrice Chatel. New phase and amplitude high resolution pulse shaper. *Review of Scientific Instruments*, 75:2668 – 2671, 2004.
- [21] A.M. Weiner. Femtosecond pulse shaping using spatial light modulators. *Review of Scientific Instruments*, 71:1929 – 1960, 2000.

- [22] Hua Zou, Changhe Zhou, and Enwen Dai. Femtosecond pulse shaping with phase-only filters. *Proceedings of SPIE*, 5636:350 – 360, 2005.
- [23] M. Hacker, G. Stobrawa, and T. Feurer. Iterative fourier transform algorithm for phase-only pulse shaping. *Optics Express*, 9:191 – 199, 2001.
- [24] Sang-Hee Shim, David B. Strasfeld, Eric C. Fulmer, and Martin T. Zanni. Femtosecond pulse shaping directly in the mid-ir using acousto-optic modulation. *Optics Letters*, 31:838 – 840, 2006.
- [25] Sang-Hee Shim, David B. Strasfeld, and Martin T. Zanni. Generation and characterization of phase and amplitude shaped femtosecond mid-ir pulses. *Optics Express*, 14:13120 – 13130, 2006.
- [26] P. Nuernberger, R. Vogt, G. Selle, T. Fenchner, S. Brixner, and G Gerber. Generation of shaped ultraviolet pulses at the third harmonic of titanium-sapphire femtosecond laser radiation. *Applied Physics B*, 88:519–526, 2007.
- [27] H.J. Bakker, P.C. Planken, and H.G. Muller. Numerical calculation of optical frequency-conversion processes: a new approach. *Optical Society of America*, 6:1665 – 1672, 1989.
- [28] M. Cavallari, G.M. Gale, F. Hache, L.I. Pavlov, and E Rousseau. Mid infra-red femtosecond pulse generation by wave-mixing: numerical simulation and experiment. *Optics Communication*, 114:329 – 332, 1995.
- [29] J. Prawiharjo, H.S.S. Hung, D.C. Hanna, and D.P. Shepherd. Theoretical and numerical investigations of parametric transfer via difference frequency generation for indirect mid-infrared pulse shpaing. *Optical Society of America*, 2006.
- [30] M Tsubouchi and M Takamasa. Femtosecond pulse shaping in the mid-infrared generation by difference-frequency mixing: a simulation and experiment. *J. Opt. Soc. Am. B*, 24:1886 – 1900, 2007.
- [31] Howe-Siang Tan and Warren S. Warren. Mid infrared pulse shaping by optical parametric amplification and its application to optical free induction decay measurement. *Optics Express*, 11:1021 – 1028, 2003.
- [32] T. Witte, K. L. Kompa, and M. Motzkus. Femtosecond pulse shaping in the mid infrared by difference-frequency mixing. *Applied Physics B*, 76:467 – 471, 2003.

- [33] A. Prakelt, M. Wollenhaupt, A. Assion, Ch. Horn, C. Sarpe-Tudoran, M. Winter, and T. Baumert. Compact, robust, and flexible setup for femtosecond pulse shaping. *Review of Scientific Instruments*, 74:4950 – 4953, 2003.
- [34] A. Galler and T. Feurer. Pulse shaping assisted short laser pulse characterization. *Applied Physics B*, 90:427–430, 2008.
- [35] Pierre Meystre and Murray Sargent III. *Elements of quantum optics*. Springer, 4th Edition, 2007.
- [36] Robert W. Boyd. *Nonlinear Optics, Third Edition 3rd*. Academic Press, 2008.
- [37] Athanasios Papoulis. *Signal Analysis*. McGraw-Hill Book Company, 1977.
- [38] Yanhua Shih. Entangled biphoton source - property and preparation. *Rep. Prog. Phys.*, 66:1009–1044, 2003.
- [39] Infrared nonlinear crystals. Electronic.
- [40] H Wang and M. Weiner. A femtosecond waveform transfer technique using type ii second harmonic generation. *IEEE Journal of quantum electronics*, 40:937–945, 2004.